Towards Benchmarking Chirality-Induced Spin Selectivity:

The Case of Chiral Tetrapyrroles

Adrian Joe Urban

June 2023

Inaugural dissertation
In application for the title "Philosophiæ Doctor" (Ph. D.)

Work Group Prof. H. M. Yamamoto

Institute for Molecular Science
National Institutes of Natural Sciences
The Graduate University for Advanced Studies, SOKENDAI

"What, if some day or night a demon were to steal after you into your loneliest loneliness and say to you: 'This life as you now live it and have lived it, you will have to live once more and innumerable times more' ... Would you not throw yourself down and gnash your teeth and curse the demon who spoke thus? Or have you once experienced a tremendous moment when you would have answered him: 'You are a god and never have I heard anything more divine'."

— Friedrich Nietzsche, *Die fröhliche Wissenschaft* (1882)

"I think that modern physics has definitely decided in favor of Plato. In fact the smallest units of matter are not physical objects in the ordinary sense; they are forms, ideas which can be expressed unambiguously only in mathematical language."

— Werner Heisenberg, *Das Naturgesetz und die Struktur der Materie (1967)*

Dedicated to my family, and in loving memory of my grandfather.

Contents

1 Introduction **1**

2 Selected Models of the CISS Effect **7**

2.1 Conventional Spin-Orbit Coupling 7

2.2 The Spinterface Effect 9

2.3 Contribution from Electron Correlation 9

3 Methods **15**

3.1 Syntheses 15

3.1.1 $Mg(OEP)(py)_2$ 16

3.1.2 Ni(OEFB) 17

3.1.3 Ni(TPBT) 18

3.1.4 Cu(TPBT) 20

3.1.5 $Mg(TPP)(py)_2$ 20

3.1.6 H_3TPBV 21

3.2 Magnetoconductive Atomic Force Microscopy 23

3.3 Electronic Circular Dichroism 26

3.4 Computational Details 28

3.4.1 Gas-phase calculations 29

3.4.2 Condensed Phase Calculations 31

3.4.3 Equipment and Data Processing 32

3.5 Complementary Methods and Materials 32

4 Results **35**

4.1 Isomerism in H_3TPBV 35

4.2 Geometrical Structure 36
4.2.1 Ni(TPBT) and H_2TPBT 36
4.2.2 *ap*/*sp* Interconversion in Ni(TPBT) and H_2TPBT . . . 37
4.2.3 Ni(OEFB) Hydrate 40
4.3 Electronic Structure and Noninnocence 42
4.4 Separability and Enantiostability 46
4.4.1 Ni(TPBT) 46
4.4.2 Cu(TPBT) 48
4.4.3 Ni(OEFB) 49
4.4.4 H_3TPBV 52
4.5 Cyclic Voltammetry 53
4.6 Behavior on Surfaces 55
4.6.1 Theoretical Predictions 55
4.6.2 Deposition on Surfaces 63
4.7 Conclusion: Expectations for observing CISS 67

5 Observing the CISS Effect 71
5.1 Sample Preparation 71
5.2 CISS via mc-AFM Measurements 74
5.3 Collaborative Projects 76
5.3.1 Monolayer Formation under Ultrahigh Vacuum 78
5.3.2 CISS in Ni(TPBT) via Mott Polarimetry 80
5.4 Conclusion 82

6 Outlook 85
6.1 Modifiable Variables 85
6.1.1 Helical Pitch and Radius 86
6.1.2 Helix Length 89
6.1.3 Electron Density 91
6.1.4 Central Metal 91
6.2 Chiral Closed-Chain Tetrapyrroles 93
6.3 Closing Remarks 93

7 Acknowledgements 95

Bibliography **98**

A Curriculum Vitae **115**

B List of Publications **117**

C Supplementary Figures and Data **119**

C.1 List of Chemicals, Vendors and Purities . . . 120

C.2 EI-MS Spectra . . . 121

C.2.1 Ni(TPBT) . . . 121

C.2.2 Cu(TPBT) . . . 122

C.2.3 H_3TPBV . . . 123

C.2.4 Ni(OEFB) . . . 124

C.2.5 Ni(OEFB) hydrate . . . 125

C.2.6 Mg(TPP) · 2 py . . . 126

C.2.7 Mg(OEP) · 2 py . . . 127

C.3 IR Spectrum of Ni(TPBT) . . . 128

C.4 ESR Peak Fitting of Cu(TPBT) . . . 129

C.5 NMR Spectra of Ni(TPBT) . . . 130

C.5.1 ^{1}H NMR . . . 130

C.5.2 ^{13}C . . . 132

C.5.3 ^{1}H,^{1}H-NOESY . . . 135

C.5.4 HMQC . . . 136

C.5.5 Proton Assignments . . . 137

C.6 NMR Spectra of *EZZZ*-H_3TPBV . . . 138

C.6.1 ^{1}H NMR . . . 138

C.6.2 ^{13}C NMR . . . 142

C.6.3 ^{1}H,^{1}H-COSY . . . 145

C.6.4 HMQC . . . 147

C.7 UV/vis Spectrum of H_3TPBV . . . 148

C.8 Potential Energy Surface Scans . . . 149

C.8.1 Ni(TPBT) . . . 149

C.8.2 21,23*H*-TPBT . . . 152

C.8.3 22,24*H*-TPBT . . . 155

C.9 Frontier Orbitals 158
C.9.1 Ni(TPBT) 158
C.9.2 Truncated Ni(TPBT) 163
C.10 Excited States of Truncated Ni(OEFB) 170
C.11 Predicted ECD of Truncated Ni(TPBT) 174
C.12 Excited States of Truncated Ni(OEFB) 178
C.13 Predicted ECD of Truncated Ni(OEFB) 182
C.14 Shell Scripts for mc-AFM Evaluation 186
C.14.1 Statistics on $I(V)$ Curves 186
C.14.2 Determining the Spin Polarization 190

Chapter 1

Introduction

When electrons leave a chiral molecule, their spin obtains a preferential orientation (spin-velocity locking) and the current is said to obtain a spin polarization (see Figure 1.1). This effect, discovered in 1999[1] and subsequently termed the "chirality-induced spin selectivity effect" or "CISS effect" in short, has been observed in a variety of molecules as diverse as helicenes[2], phthalocyanines[3], molecular motors[4] oligopeptides[5] or even large biomolecules such as DNA strands[6–8]. While experimental setups for observing this spin polarization have been similarly diverse – Ultraviolet photoelectron spectroscopy coupled with Mott polarimetry[6], magneto-conductive AFM[7,9,10], electrochemical methods[11] or Hall bar measurements[4,12,13] to name a few – and thus the amount of publications observing CISS has been steadily growing, it is all the more surprising that no consensus of the theoretical origin of the CISS effect has emerged yet[14]. Much rather, theories emerging from various disciplines of chemistry and physics have tried to explain this effect from angles such as scattering theory[15], phonon coupling[16], polaron transport[17] or many-body perturbation[18,19] and field theory[20]. To the author's knowledge, the points of mutual agreement in terms of the phenomenology are thus far as follows:

- The CISS effect is a nonequilibrium effect or, in simple terms: If one were to look at an isolated DNA strand in vacuum in the dark and were able to visualize the spin polarization across the double helix, one

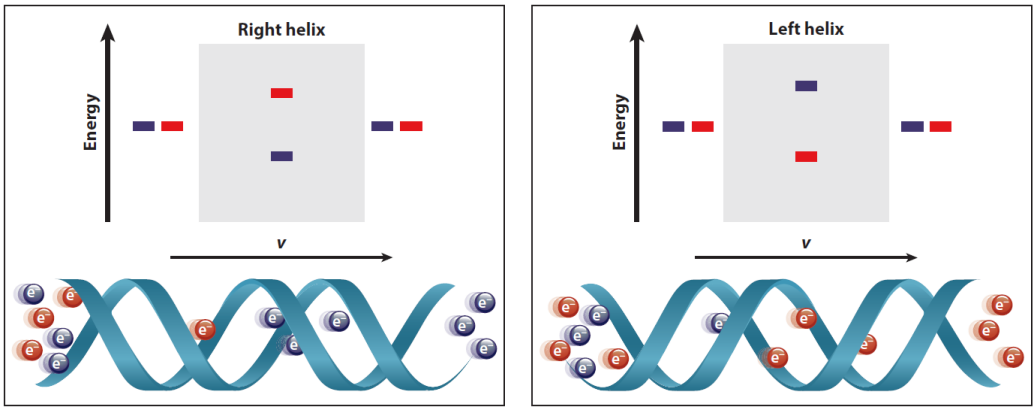

Figure 1.1: Schematic representation of the chirality-induced spin selectivity effect[25]. As electrons with spin α and β travel through a chiral potential – here indicated as a double helix – the degeneracy of the respective spin states is lifted and electrons leaving the potential are either in the α or the β state: The respective current becomes "spin-polarized".

would not see a spin accumulation anywhere, neither at the termini nor somewhere in between.

- The CISS effect is observable at room temperature, and both in electron transmission[1,6,8] as well as electron transport[7]. That is, it is both observable in bonded and unbonded electrons.

- Spin-orbit coupling (SOC) alone cannot explain the strength of the spin polarization observed in many systems. This is motivated by the fact that CISS is observable throughout a plethora of organic molecules (with spin polarization exceeding 60 % in the case of DNA[6] or 85 % in supramolecular porphyrin assemblies[21]) containing only carbon, hydrogen, oxygen and nitrogen; all elements with very weak SOC.

- The CISS effect is closely related to optical activity[21–24], more specifically to the absorption asymmetry factor g_{Abs} (sometimes also referred to as "Kuhn's factor").

From a molecular point of view, the following consensus seems to emerge:

- Opposite chiralities will always lead to opposite spin polarizations: electrons with spin α will only be preferentially transmitted by a left-handed *or* a right-handed molecule, not by both.
- At surfaces, the CISS effect is influenced by the interactions between substrate and adsorbate at least to some extent [5,26–28]. In some cases such as polyalanine peptides, the spin polarization even flips its sign for the same chirality when the molecules are attached to a substrate with the amino- or the carboxyl-terminus.
- The strength of the CISS effect generally increases with the length of the chiral medium [8,23,29,30].

While the potential applications of the CISS effect have been demonstrated on various occasions, such as for photovoltaics [31], catalysis [32–40], spintronics [41–47], OLEDs for circularly polarized light [48,49] and enantioseparation [10,50–54], the above consensus, despite the wide array of model systems and experimental setups, is still too thin to allow for targeted fabrication of devices ready for commercialization. One reason for the lack of a concise theoretical model may be a lack of capabilities for "benchmarking". Here, a property of interest $\chi(a, b, c, ...)$ depends on various parameters $a, b, c...$ and the relationship between both is explored by keeping all but one parameter fixed and then measuring, for example, $\chi(a)$. This approach is especially prominent in computational chemistry or, in everyday life, in the hardware and software design of the videogame industry. In order to apply the benchmarking approach to chiral molecules under study for the CISS effect, several properties can be seen as potential parameters: In molecules with helical chirality, these include the helix' radius, pitch and length, in addition to electron density or resistivity.
Helical tetrapyrroles, found in nature as bile pigments during heme catabolism [55] (see Figure 1.2), offer a promising opportunity for such benchmarking. Not only are their structures inherently chiral with well-defined features. They also hold several opportunities for variation, as they are derived from the

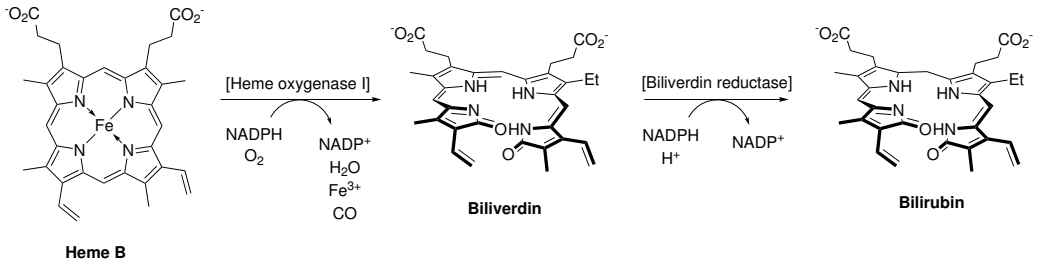

Figure 1.2: Degradation of heme B to bilirubin.

cleavage of metal porphyrins – a class of molecules with established chemistry and a history of at least a century[56]. In addition, elucidating the spin transport in these chiral molecules obviously provides valuable insight into how chiral information is transported and amplified in biological systems, as biliverdin (produced by catabolism of heme B) is redox-active. In fact, albumin-bound biliverdin is one of the most important antioxidants in human blood plasma[55]. This *in vivo* redox chemistry, together with the chance for showing a noticeable CISS effect, is closely related to the presently unknown origin of homochirality in the natural world[57]. There, the question at hand is: Why is all life on earth, consisting of several chiral building blocks, almost exclusively made out of one enantiomer (D-ribose, L-amino acids, ...) and not of the other, although both have identical reactivity in an otherwise achiral medium?

Similarly to the porphyrins, the helical tetrapyrroles can act as a tetradentate ligand to coordinate various metal atoms. This feature holds the potential for studying the CISS effect of a chiral molecule in the presence of an external perturbation, i.e. the *d* electrons of a metal atom. In contrast to the porphyrins that see an estimated 2,500 publications per year as of 2021[58], the chemistry of their cleavage products is considerably underreported as both the early pioneer work in the groups of Kevin M. Smith[59–61], Jürgen-Hinrich Fuhrhop[62–65] and Alan D. Balch[66–73], as well as later work of the Mizutani group[74–85] have focused predominantly on their synthesis rather than further modifications or their physical and chemical properties. As a result, many aspects that are important for the fabrication of modern nanoscale devices

are unknown and making these molecules accessible to modern CISS setups is certainly not trivial.
Hence, the thesis presented here aims to evaluate these CISS-relevant properties as well as the CISS effect itself for several molecules:

1. Octaethylformylbiliverdinato complexes from the photooxidation of octaethylporphyrinato magnesium(II): Ni(OEFB) in Figure 1.3b.

2. Tetraphenylbilatrienones from oxidation of tetraphenylporphyrinato iron(III) chloride: Ni(TPBT) and Cu(TPBT) in Figure 1.3c.

3. Tetraphenylbiliviolins from photooxidation of tetraphenylporphyrinato magnesium(II): H_3TPBV in Figure 1.3d.

The main part of this work is then separated into four sections: In the first section (Chapter 3.1), the molecules are synthesized and, where merited, existing literature is optimized for yield and scaling.
The second section (Chapters 4.2–4.6) is dedicated to a more in-depth analysis in terms of structure, spectral and electronic properties, as well as the separability of both helicities and their stabilities. The findings are augmented by modern computational predictions for the molecules in the gas phase, on gold, and on highly oriented pyrolytic graphene (HOPG); all being important aspects for the fabrication of surfaces where the CISS effect is measured.
In the third section (Chapter 5), the respective surfaces are manufactured and the CISS effect of the molecules is investigated via magneto-conductive AFM. These results include collaborative work under ultrahigh vacuum in Chapter 5.3, with the group of Prof. Helmut Zacharias at the university of Münster in Germany (Westfälische Wilhelms-Universität Münster).
Lastly, the fourth section (Chapter 6) is concerned with a general outlook and aims answer the question which systematic modifications and future measurements of the tetrapyrroles are possible, both for future benchmarking but also for possible experimental setups with these molecules in general.

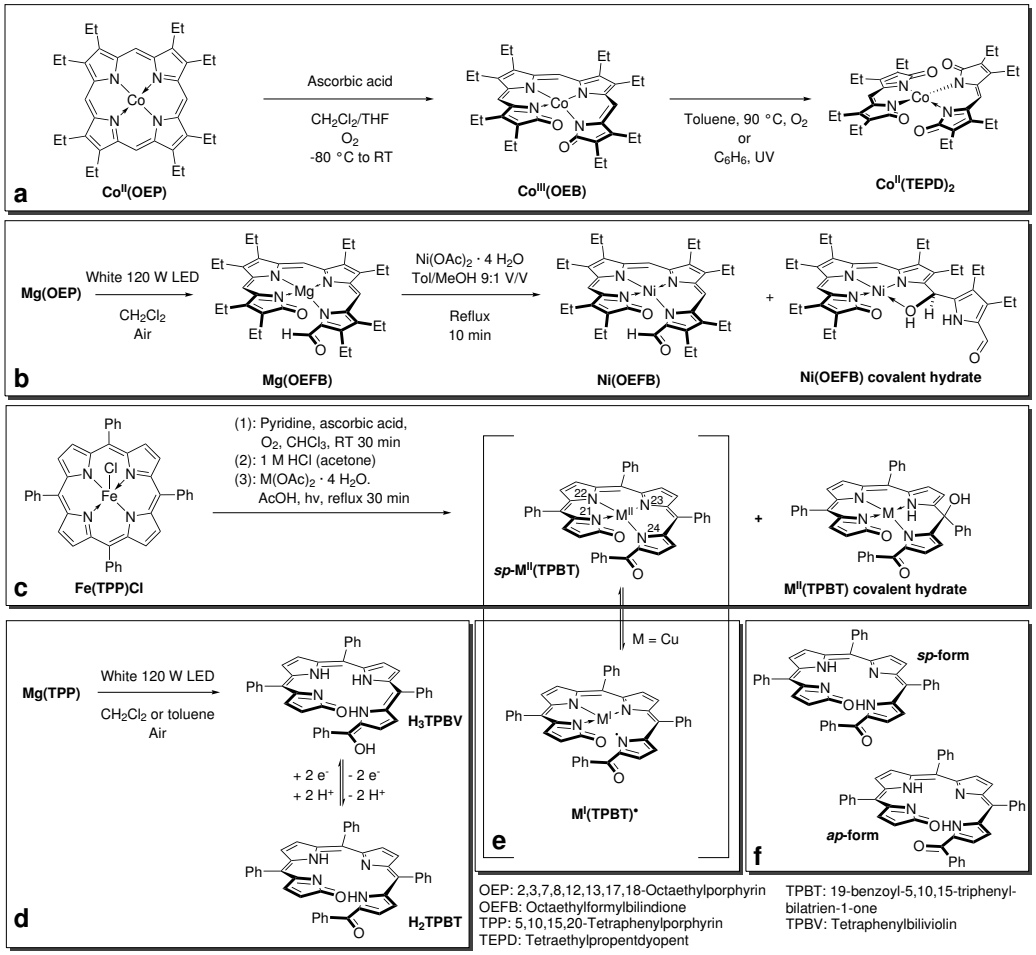

Figure 1.3: Selected syntheses of helical tetrapyrroles. (a) Oxidation of octaethylporphyrinato cobalt(II) in the presence of ascorbic acid to give octaethylbiliverdinato cobalt(III) and further degradation to ditetraethylpropentdyopento cobalt(II)[67–69] (b) Photooxidation of octaethylporphyrinato magnesium(II) and subsequent transmetalation to give octaethylformylbiliverdinato nickel(II)[63,64,70] as well as a "covalent hydrate" isolated in this work (c) Oxidation of tetraphenylporphyrinato iron(III) chloride with subsequent transmetalation to give tetraphenylbilatrienato complexes and a covalent hydrate[61,77,80,84,86] (d) Photooxidation of tetraphenylporphyrinato magnesium(II) to give tetraphenylbiliviolin[87] (e) Noninnocent behavior in Cu(TPBT) complexes (f) *ap*/*sp* isomerism in TPBV molecules.

Chapter 2

Selected Models of the CISS Effect

As mentioned in the introduction, no model of the CISS effect explaining all experimental findings currently exists. This fact notwithstanding, this chapter aims to give an overview of some models seeking to explain and/or quantify the CISS effect from various angles. Each model is briefly summarized and the consequences, if applied to helical tetrapyrroles, are laid out. As this work is mainly concerned with CISS measurements at the interfaces of a molecule and two electrodes, models with periodic boundary conditions are forgone for the sake of brevity. Instead, the focus is on models that can be applied either to interfaces or isolated molecules.

2.1 Conventional Spin-Orbit Coupling

The "conventional" spin-orbit coupling arises from the electrostatic field $\mathbf{E}$ of an atom's nucleus around which an electron moves with a velocity $\vec{v}$, a momentum $\vec{p}$ and a mass m_e. The electric field, in turn, gives rise to a magnetic field $\mathbf{B}$ that is described by the equation

$$\mathbf{B} = -\frac{\vec{v}}{c} \times \mathbf{E} \quad \rightarrow \quad \mathbf{B}_{\mathrm{NR}} = -\frac{1}{m_e c}\mathbf{E} \times \vec{p} \tag{2.1}$$

where the right equation applies if the electron's velocity is small compared to the speed of light c. As a result of the magnetic field, the electron's magnetic

momentum $\vec{\mu}_e$ changes direction; it experiences a "torque" and the potential $V_{\mathrm{SOC}} = -\vec{\mu}_e \cdot \mathbf{B}_{\mathrm{NR}}$ acting on the electron is expressed as

$$V_{\mathrm{SOC}} = -\frac{\varepsilon\hbar}{2m_e^2c^2} \cdot \vec{\sigma} \cdot (\mathbf{E} \times \vec{p}) \tag{2.2}$$

with the reduced Planck's quantum $\hbar$ and the permittivity ε. For an atomic nucleus, the electric field $\mathbf{E}(\vec{r})$ at any point $\vec{r}$ is given as

$$\mathbf{E}(\vec{r}) = -\frac{Zq_e}{4\pi\varepsilon_0}\frac{\vec{r}}{r^3} \tag{2.3}$$

where q_e is the elementary charge, ε_0 is the vacuum permittivity and Z is the atomic number. As a result, a bonded electron will experience a spin-orbit coupling potential of the form

$$V_{\mathrm{SOC}} = \frac{Zq_e^2}{8\pi\varepsilon_0}\frac{1}{m_e^2c^2r^3}\vec{s}\cdot\vec{l} \tag{2.4}$$

where $\vec{s}$ is the electron's spin and $\vec{l}$ is its angular momentum. One may now make the approximation that the distance between an electron and the nucleus is inversely proportional to its atomic number (i.e. $r = 1/Z$) to find that

$$V_{\mathrm{SOC}} = \frac{Z^4q_e^2}{8\pi\varepsilon_0}\frac{1}{m_e^2c^2}\vec{s}\cdot\vec{l} \quad \Rightarrow \quad V_{\mathrm{SOC}} \propto Z^4. \tag{2.5}$$

However, given the high amounts of spin polarization observed in the experiments introduced in Chapter 1, spin-orbit coupling alone clearly cannot explain chirality-induced spin selectivity, as the spin-orbit coupling is fairly small in metal-free organic molecules like DNA, helicene, polypeptides and others. In fact, this discrepancy is typically in the realm of three orders of magnitude[7,88]. Hence, other approaches like the ones introduced below have to play a significant role.

2.2 The Spinterface Effect

The theoretical model introduced in 2022 by Yonatan Dubi[89] was devised specifically with magneto-conductive AFM of double-stranded DNA on Au/Ni in mind. Here, the model is concerned with the interaction of spin-orbit coupling between the chiral molecule and the substrate, and proposes a strong dependence of the CISS effect on the coupling of electrons with phonons (collective vibration of ordered atoms). His model finds, for model DNA strands of a fixed length, that the spin polarization is voltage-dependent and increases linearly with the bias until a maximum is reached; the location of which and the associated magnitude of the spin polarization are dependent on the strength of the electron-phonon coupling. After reaching this maximum, the polarization then drastically declines until, typically at 1.5–2 V, it returns to zero. Because in this model, the CISS effect is strongly dependent on the molecule's transport properties, the dependence on the length of the chiral molecule is also variable (see Figure 2.1).
The model starts with the assumption that the CISS effect is the cause of spin-dependence of the energetic levels, in a fashion similar to Zeeman splitting. This effect is assumed to arise from the current passing through a helical molecule, generating a solenoid magnetic field that interacts with the magnetic moment of the metallic substrate. Additionally a small difference in the distributions of α and β spin generates an effective "spin torque" field which, together with the solenoid field are sufficient in stabilizing the surface angular momentum.

2.3 Contribution from Electron Correlation

In 2019, Jonas Fransson[18] brought forward a model to describe chirality-induced spin selectivity within the theoretical framework of electron correlation. Here, a molecule of helical chirality between two leads is described as consisting of several sites along a helical pathway, with each site experiencing on-site Coulomb interaction and next-nearest neighbor spin-orbit interaction, in addition to nearest-neighbor hopping. The energetic level of an electron at

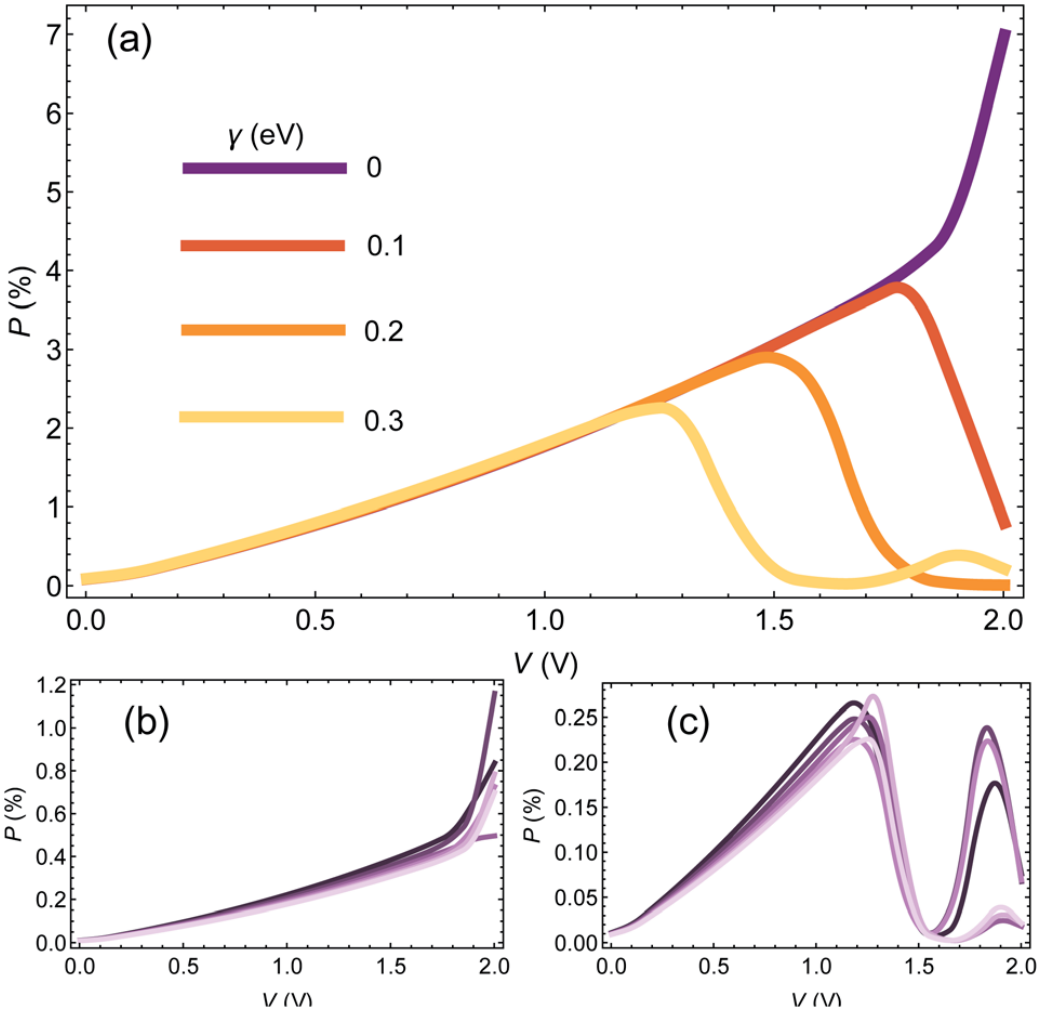

Figure 2.1: (a) Modelled polarization P of the mc-AFM current as a function of voltage for a DNA chain – consisting only of 25 base pairs of cytosin C guanin G – for electron-phonon coupling strengths, characterized by the coupling parameter γ. (b) Polarization over different biases for varying amounts of CG base pairs at zero electron-phonon coupling, i.e. $\gamma = 0\,\text{eV}$. (c) Same as (b), for $\gamma = 0.3\,\text{eV}$. Reproduced from Y. Dubi[89] with permission from the Royal Society of Chemistry.

site m with a total of M sites is constructed in second quantization as follows. The first part consists of

$$\hat{H}_{\text{Coul}} = \sum_{m=1}^{M} \left(\varepsilon_m \hat{a}_m^\dagger \hat{a}_m + U_m \hat{n}_{m,\uparrow} \hat{n}_{m,\downarrow} \right) \tag{2.6}$$

where ε_m is the interaction-free energy, $\hat{a}_m^\dagger$ and $\hat{a}_m$ are the creation and annihilation operators, U_m is the energy from electron-electron interaction and $\hat{n}_{m,\uparrow/\downarrow}$ are the electron number operators for spin-up and spin-down. Nearest neighbor hopping is characterized by the following expression

$$\hat{H}_{\text{Hop}} = t \sum_{m}^{M-1} \hat{a}_m^\dagger \hat{a}_{m+1} + \text{c.c.} \tag{2.7}$$

with the hopping integral t which, if approaching zero, describes electrons being "frozen" at their current position and being unable to move the nearest site. Similarly, spin-orbit coupling between next-nearest neighbors is described by the Hamiltonian

$$\hat{H}_{\text{SOC}} = \lambda \sum_{m}^{M-2} \left(i \, \Psi_m^\dagger \vec{v}_m \cdot \vec{\sigma} \Psi_{m+1} + \text{c.c.} \right) \tag{2.8}$$

where λ is the spin-orbit integral and $\vec{\sigma}$ is a vector containing the Pauli matrices. The vector $\vec{v}_m$ contains information about the molecule's helicity, as it is defined as the normalized vector product of the position vectors of nearest and next-nearest site:

$$\vec{v}_m = \vec{d}_{m+1} \times \vec{d}_{m+2} \quad \text{with} \quad \vec{d}_{m+n} = \frac{\vec{r}_m - \vec{r}_{m+n}}{|\vec{r}_m - \vec{r}_{m+n}|}. \tag{2.9}$$

Lastly, as described above, the helical molecule is sandwiched between two metallic leads, the interaction with which be solely through tunneling described via

$$\hat{H}_{\text{tun}} = \sum_{p} t_p \Psi_p^\dagger \Psi_1 + \sum_{q} t_q \Psi_q^\dagger \Psi_1 + \text{c.c.} \tag{2.10}$$

with the Hamiltonian of either left (L) and right (R) lead modelled as $\hat{H}^{\mathrm{L/R}}_{\mathrm{Lead}}$ and its description omitted here for brevity, the Hamiltonian of the entire lead-molecule-lead junction is described as the sum of equations 2.6 through 2.10:

$$\hat{H}_{\mathrm{tot}} = \hat{H}_{\mathrm{Coul}} + \hat{H}_{\mathrm{Hop}} + \hat{H}_{\mathrm{SOC}} + \hat{H}_{\mathrm{tun}} + \hat{H}^{\mathrm{L}}_{\mathrm{Lead}} + \hat{H}^{\mathrm{R}}_{\mathrm{Lead}}. \tag{2.11}$$

It is important to point out that in the framework of this model, the spin predicted spin polarization of a chain with $M = 3$ sites (for example, a suitably substituted halocarbon) vanishes even in the correlated case because, via equation 2.9, the possible scattering channels either cancel each other out (up to third order) or become spin-symmetric (fourth order and higher). It is only for $M > 3$ that the spin symmetry of the higher-order scattering channels is lifted.

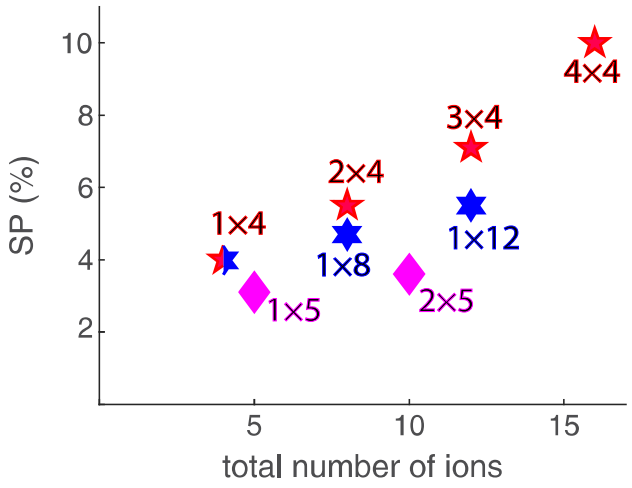

Figure 2.2: Maximum spin polarization SP of the current in the metal-molecule-metal junction as a function of the number of ions in the molecular chain. Nomenclature follows $M \times N$ with M being the numbers of laps and N the numbers of ions per lap[18]. Reprinted with permission from J. Fransson. Copyright 2019 American Chemical Society.

The results for the maximum spin-polarization of the current passing through the junction can be obtained by evaluating equation 2.11, and are given in Figure 2.2. These results are consistent with the observation that the CISS effect generally increases with the helix length (as SP linearly increases with M). A less expected result, however, is the behavior of $SP(N)$ at constant M: starting at $N = 4$, the spin polarization first decreases when moving to $N = 5$ before recovering to higher values and increasing linearly. This initial decrease is proportional to the number of turns M and the behavior has unfortunately not been explained in this work; neither will it be very likely to verify experimentally, as N – with the helix radius being equal – is mostly limited to the carbon-carbon bond distance of 1.54–1.20 Å in organic molecules[90,91].

Nonetheless, treating the resulting point as an outlier and extrapolating Fransson's data, the spin-polarization of the molecules in Figure 1.3 may be well over 6 %, assuming a number of $M = 1$ turns and $N = 24$ sites (i.e. atoms) per turn. This hypothesis will be put to the test in Chapter 5.

Chapter 3

Methods

The following section is concerned with the theoretical and apparative details of the experiments used in this work. First, a brief theoretical overview and, if merited, a connection to the CISS effect are briefly given. This is followed by the experimental details of the setup used by the author. The detailed setup for collaborative projects are given in the respective chapters (5.3.1 and 5.3.2).

3.1 Syntheses

The syntheses represent typical examples conducted by the author and were necessarily varied in scale, depending on the demand at the given time. Unless otherwise stated, all reagents were used as received by the supplier. Pyrrole was distilled on a rotary evaporator (35 torr, 60 °C water bath) immediately before use and otherwise stored over CaH_2 at -22 °C in a brown glass flask. With the exception of H_3TPBV, all synthetic protocols have for the most part been taken verbatim from an earlier work of the author[92] who is responsible for the syntheses presented therein.

3.1.1 $Mg(OEP)(py)_2$

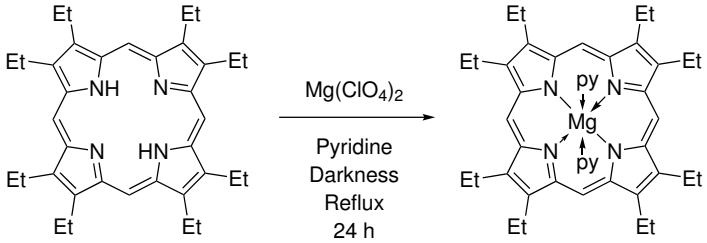

This molecule was synthesized using literature procedure[62] to give 142 mg from 200 mg H_2OEP (53 %). Crystals (CCDC 2240944) precipitated upon the cold storage in Et_2O. The brine was evaporated to dryness and extracted with few milliliters of CH_2Cl_2 to leave an insoluble colorless solid behind. The extract was evaporated to dryness and combined with the aforementioned crystals to give a total yield of 53 % (142 mg from 200 mg H_2OEP).
EI-MS (direct injection) m/z = 557.25 $[Mg(TPP)+H]^+$ 100 %, 541.20 $[M-CH_3]^\bullet$ 30 %, 278.20 $[Mg(TPP)]^{2+}$ 37 %.

3.1.2 Ni(OEFB)

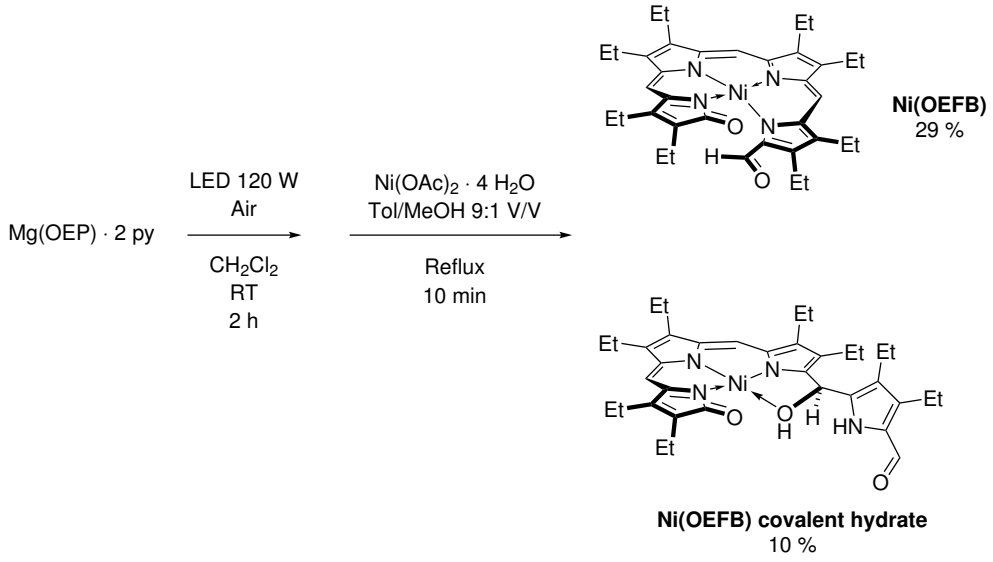

This procedure was adapted from Koerner *et al.*[70]. The 142 mg Mg(OEFB) · 2 py from the synthesis above were added to 3 l CH_2Cl_2 and irradiated with a 120 W corn-type LED lamp (white with ca. 3300 K, placed 15 cm away) while being stirred under access to air at room temperature for 2 h. Filtration and evaporation of the filtrate gave a brown-violet solid. This solid was dissolved in a mixture of 400 ml toluene and 40 ml MeOH, then treated with 200 mg $Ni(OAc)_2 \cdot 4\ H_2O$ and heated at 85 °C for 10 min. After evaporation to dryness, the olive solid was redissolved in 5 ml toluene and separated on SiO_2 (d = 4 cm, l = 15 cm). Starting with toluene first eluted H_2OEP (2 mg or 2 %), changing to 2 % acetone in toluene then eluted the covalent hydrate as a blue band (CCDC 2241426, $R_F = 0.37$, 13 mg or 10 %). This blue band could be crystallized via slow evaporation of a 50:50 mixture of EtOAc/hexane. The product eluted last ($R_F = 0.24$, 34 mg or 27 %, lit. 29 %) and readily crystallized upon evaporation of the solvent on a rotary evaporator at 60 °C. Another band with $R_F = 0.11$ was visible on TLC but could not be isolated on the column.

For the water-free Ni(OEFB) EI-MS (direct injection) m/z = 591.10 $[M\text{-}CHO]^{\bullet}$ 100 %, 563.10 $[M\text{-}CHO\text{-}C_2H_5]^{+\bullet}$ 35 %, 275.10 50 %.
For the covalent hydrate of Ni(OEFB) EI-MS (direct injection) m/z = 640.15 $[M+H]^{+}$ 44 %, 609.10 $[M\text{-}C_2H_5]^{+}$ 69 %, 581.15 $[M\text{-}CHO\text{-}C_2H_5]^{+\bullet}$ 100 %.

3.1.3 Ni(TPBT)

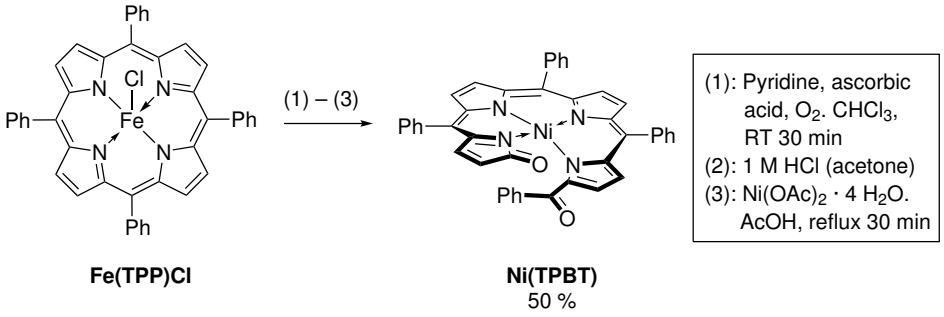

Fe(TPP)Cl **Ni(TPBT)** 50 %

H_2TPP was synthesized[93] and metalated[94] with $FeCl_2$ using literature procedure ($FeCl_3$ or $Fe(OAc)_2 \cdot H_2O$ may be used instead). 1 g of the resulting Fe(TPP)Cl was dissolved in 60 ml pyridine and stirred for 15 min to allow for complete solution. In the meantime, 500 ml $CHCl_3$ were saturated with O_2 at room temperature for 15 min. The red pyridine solution was added, followed immediately by 5 g ascorbic acid and stirring at room temperature for 30 min. Now brown in color, the mixture was filtered and evaporated to dryness, then treated with 100 ml of 1 M HCl in acetone (8 ml of 37 % aqueous HCl to 92 ml acetone). The resulting blue solution was stirred for 5 min, then 9 g $NaHCO_3$ (NaOH may be used instead) in 100 ml water were added dropwise under stirring to give a violet solution. After the addition of 200 ml water, the mixture was extracted three times with each 300 ml CH_2Cl_2. After evaporation of the combined organic phases, the residue was dissolved in 100 ml glacial acetic acid and, under irradiation with a 170 W tungsten halide lamp (white 120 W corn-type LED with 3300 K maybe used instead) placed 15 cm away from the vessel, refluxed together with 800 mg of $Ni(OAc)_2 \cdot 4\ H_2O$ for 20 min. Having cooled to room temperature and assumed a brown to olive color, ice cold 6 M NaOH (67 g to 300 ml H_2O) was added under stirring. The precipitate was filtered off to remove most of

the sodium acetate, then dried and separated on a SiO_2 column (l = 35 cm, d = 4 cm) using 5 % acetone in CH_2Cl_2. Doing so first eluted H_2TPP and Ni(TPP) in one band ($R_F \approx 0.90$). Thereafter eluted a short blue band that, interestingly, was not the covalent hydrate of Ni(TPBT) but rather appeared to be either $[Ni^{II}(HTPP)]_2O$ or $[Ni^{III}(TPP)]_2O$ (crystallizable from EtOAc/hexane 50:50, CCDC 2242338, $R_F = 0.75$, 25 mg or 3 %, not analyzed further). Afterwards, water-free Ni(TPBT) was eluted as a brown solid (crystallizable from CH_2Cl_2 or $CHCl_3$, CCDC 2240943, $R_F = 0.51$, 500 mg or 50 %).

EI-MS m/z = 703.90 $[M+H]^+$ (15 %), 599.00 (100 %).

^{1}H NMR (600 MHz, $CDCl_3$) δ 8.13 (dt, 2H), 7.45–7.65 (m, 17H), 7.40 (tt, 1H), 7.33 (d, 1H), 7.30 (t, 2H), 7.20 (d, 1H), 7.17 (d, 1H), 7.00 (d, 1H), 6.98 (d, 1H), 6.66 (d, 1H), 5.75 (d, 1H).

^{13}C NMR (600 MHz, $CDCl_3$) δ 186.67, 180.90, 166.03, 158.98, 152.97, 150.91, 145.45, 143.79, 142.92, 140.95, 139.84, 138.88, 137.62, 137.22, 136.35, 135.09, 132.90, 132.76, 132.16, 131.90, 131.30, 131.06, 130.76, 130.41, 129.15, 128.84, 128.27, 127.92, 127.79, 127.51, 127.15, 124.85, 117.00. This compound was well soluble in most dry solvents, but almost insoluble in aliphatics and completely insoluble in water. Solutions of Ni(TPBT) are sensitive to water and MeOH to change the color towards the green, giving bands of the water-free compound and the covalent hydrate or methanolate. This behavior is consistent with literature descriptions of the zinc complex[78,86]. The synthesis was later repeated with half the amount of AcOH and using a half-equimolar amount of Na_2CO_3, without changes in the yield.

3.1.4 Cu(TPBT)

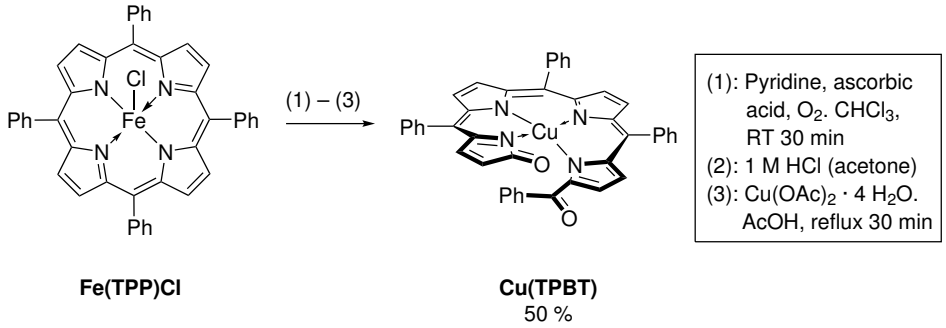

Fe(TPP)Cl **Cu(TPBT)** 50 %

This compound was synthesized using the method above, substituting $Ni(OAc)_2 \cdot 4\,H_2O$ for
$Cu(OAc)_2 \cdot 4\,H_2O$. Gave an orange-brown solid at identical yields.
^{1}H-NMR (600 MHz in $CDCl_3$): No signal obtainable in the region of ± 400 ppm.
EI-MS m/z = 708.95 $[M+H]^+$ (15 %), 604.00 $[M\text{-}PhCO]^{+\bullet}$ (100 %).
Solutions behave like the ones of the nickel complex towards H_2O and MeOH.

3.1.5 Mg(TPP)(py)$_2$

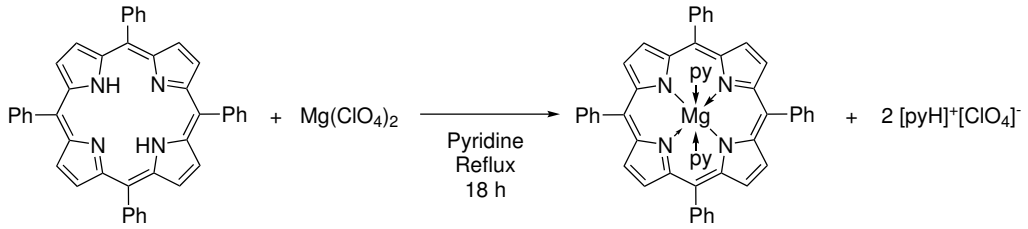

H_2TPP 1 eq 1.5 eq **Mg(TPP)(py)$_2$** 79 %

1 g H_2TPP and 545 mg $Mg(ClO_4)_2$ (1.5 eq) were refluxed in 100 ml pyridine for 18 h in the dark. Letting the solution come to room temperature on the oil bath, 200 ml MTBE (Et_2O may be used instead) were added without stirring and the mixture was left to stand over night to precipitate a large portion of the product (703 mg) as blueviolet rhomboeders or platelets, typically suitable for x-ray crystallography upon filtration, rinsing with hexane and drying. The filtrate was washed twice; first with 4.5 g household-grade citric acid in

150 ml water, then with 150 ml water only. The organic phase was dried over Na_2SO_4 and evaporated to dryness, to give another 334 mg of the product in equal purity. Both portions were combined and dried over night at 120 °C to yield 1.037 g or 79 %.

EI-MS (direct injection) m/z = 636.05 Mg(TPP)$^\bullet$ 100 %, 614 TPP$^\bullet$ 15 %, 558.05 $[M\text{-}Ph]^+$ 15 %.

3.1.6 H_3TPBV

Early Variant

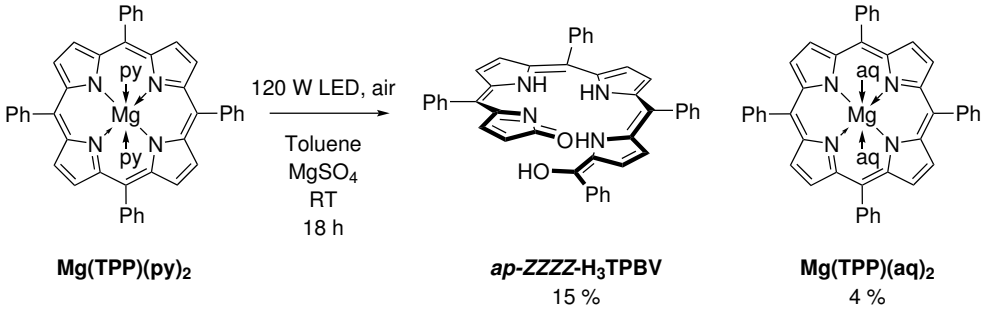

This synthesis was adapted from Matsuura *et al.*[87]. 3 g of Mg(TPP) · 2 py were added to 3 l toluene together with 30 g $MgSO_4$ to give a red solution. Using a conventional aquarium pump (delivering ca. 1.2 l/min), the mixture was aerated and the vessel was illuminated with a 120 W corn-type LED lamp (white with ca. 3300 K, placed 15 cm away) for a total of 18 h at room temperature. Toluene that evaporated during this period was not replenished. After filtration and evaporation to dryness, the crude was chromatographed on SiO_2 (l = 40 cm, d = 6 cm) with 5 % MeOH in CH_2Cl_2. Doing so first eluted H_2TPP and Mg(TPP) together ($R_F \approx 1$, 1 g or 43 %), followed by a small green portion of Mg(TPP) · 2 H_2O (occasionally crystallized in the test tubes, CCDC 2240945, $R_F = 0.71$, 92 mg or 4 %) and the H_3TPBV ($R_F = 0.50$, 600 mg or 25 %). No other portions eluted thereafter.

EI-MS (direct injection) m/z = 648.20 M$^\bullet$ 60 %, 543.20 40 %, 326.15 45 %, 261.10 100 %.

Late Variant

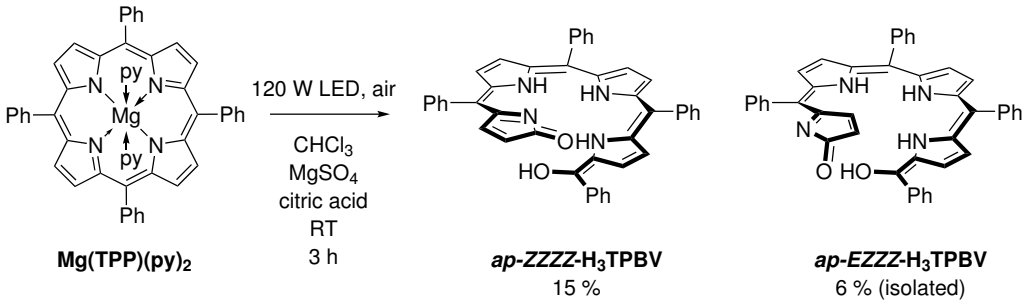

3 g of Mg(TPP) · 2 py were added to 3 l $CHCl_3$ together with 30 g $MgSO_4$ to give a red solution. Using the setup shown in Figure 3.1, the mixture was irradiated internally with a 120 W corn-type LED lamp (white with ca. 3300 K) while being aerated with a commercially available aquarium pump (delivering ca. 1.2 l/min). After 30 min, the lamp was turned off to allow the now warmed mixture to cool down for 30 min. This procedure was repeated two more times and the $CHCl_3$ was evaporated down to ca. 100 ml and filtered. The filtrate was evaporated and the residue was extracted with 5×50 ml to leave most of the insoluble H_2TPP and Mg(TPP) behind. The filtrate was evaporated and separated on SiO_2 (l = 35 cm, d = 3 cm) with 5 % MeOH in CH_2Cl_2. This eluted a short band of H_2TPP and Mg(TPP) together ($R_F \approx 1$, not collected), followed by the product ($R_F = 0.50$, 363 mg or 15 %) and another band of similar color ($R_F = 0.26$) with identical EI-MS spectrum and seemingly similar yield, of which 152 mg (6 %) could be isolated. This compound was later assigned to the *EZZZ* isomer, based on a strong signal from one of the pyrrole hydrogens in H,H-COSY that coupled with

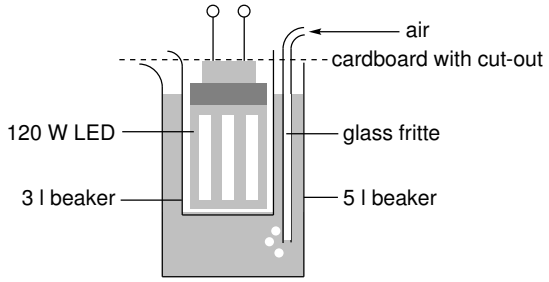

Figure 3.1: Experimental setup used in a later variety of H_3TPBV synthesis.

a β-pyrrole proton and was not visible in the H,H-NOESY spectrum of the *ZZZZ* compound. The compound transformed into the ZZZZ isomer on the TLC plate within 3–4 h and within 1–2 d in solution.

3.2 Magnetoconductive Atomic Force Microscopy

Magnetoconductive atomic force microscopy (or mc-AFM in short) belongs to the group of AFM methods and as such, is a type of scanning probe microscopy. In classical light microscopy, Ernst Abbe described the resolution (that is, the minimum distance between two separate objects needed to distinguish them) to be limited to half of the wavelength of the incident light [95]. Assuming the human eye to be most sensitive to light in the 500 nm range [96], conventional light microscopy is not suitable for resolving structures less than 250 nm in size. Scanning probe techniques, on the other hand, rely on the interaction of a probe with the sample (for example, attractive or repulsive interactions, or the generation of a tunneling current), scanning it at different points using piezoelements to move the sample. The resulting map provides information about the sample at a scale of small molecular aggregates, single molecules, or even individual atoms.

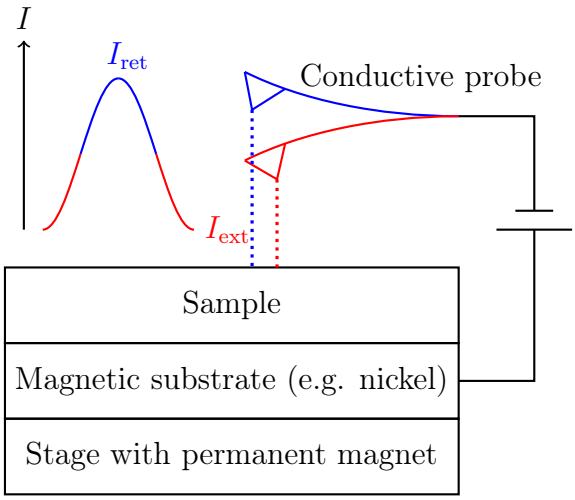

Figure 3.2: Working principle of magneto-conductive atomic force microscopy (mc-AFM), shown on the example of Bruker's proprietary "PeakForce TUNA" mode. A sample is deposited onto a magnetic substrate (optionally, with a protective layer such as gold) and a permanent magnet with adjustable orientation is placed underneath. A conductive AFM probe is kept at constant amplitude while obtaining an $I(V)$ curve while extended and/or retracted. In this work, the cantilever was constantly held in the extended regime.

If the probe is a conductive cantilever, a sample may be scanned at a single point while recording the measured current at a given voltage range, resulting in $I(V)$ curves which are often characteristic for the sample. If the sample (or the substrate on which it is deposited) is magnetic, the work function of the magnetic material becomes spin dependent and the resulting technique is referred to as "magnetoconductive AFM" or mc-AFM. As the CISS effect is concerned with the spin-dependent electron transport through a chiral potential, this setup allows for easy evaluation of a molecule's ability to act as spin filters, because $I(V)$ curves can be recorded for different magnetization directions of the substrate (such as a layer of nickel). The spin-polarization of a molecule SP may then become voltage-dependent. Typically, it is expressed as the difference between the currents measured at up- and down-magnetization, divided by the sum of both and optionally given as percentages:

$$SP(V) = \frac{I_{\mathrm{down}}(V) - I_{\mathrm{up}}(V)}{I_{\mathrm{down}}(V) + I_{\mathrm{up}}(V)} \cdot 100\ \%. \tag{3.1}$$

However, this nomenclature for "up" and "down" is arbitrary and has not been used consistently throughout literature; thus, care has to be taken when comparing results of different publications. To circumvent this issue, Clever *et al.* have recently proposed[13] the convention

$$SP(V) = \frac{I_{\text{parallel}}(V) - I_{\text{antiparallel}}}{I_{\text{parallel}}(V) + I_{\text{antiparallel}}(V)} \cdot 100\ \% \tag{3.2}$$

where "parallel" and "antiparallel" refer to the electron's spin pointing alongside or opposite to their velocity direction, respectively. Similarly then, it is important to clearly establish the definition of positive and negative voltages, as these are a direct indicators for the velocity direction. For the purpose of this work, a negative bias means an electron flow from sample to tip, while positive voltages indicate flow from tip to sample.

Setup

For the mc-AFM measurements in this work, a Bruker XR Icon was used in PeakForce TUNA Mode with a Nanoworld CDT-FMR-10 cantilever. This cantilever consisted of silicon, with a conductive diamond coating on the tip side and aluminium coating on the detector side. In the software, cantilever options were chosen for a DDESP-FM tip while choosing the spring constant as 6.2 N/m. The samples were fixed to a conductive stage with silver paste (made from fine silver powder and diethyl succinate) and dried for at least thirty minutes. The magnetization of the nickel layer was changed by rotating a permanent magnet underneath the stage. The strengths of the magnetic field on the four quadrants on the stage are given in Figure 3.3 for angles of 90° and 270° and represent the maximum possible strengths with this setup without additional magnetization along the surface plane. Here, special care was taken to measure the sample enantiomers at identical minimum and maximum field strengths by proper placement on the respective quadrants. Before recording the $I(V)$ curves, a 200 nm × 200 nm AFM image was taken with the same cantilever in order to judge the quality of the sampled area. The curves were then recorded with a start and end bias of –2 V and +2 V, using a ramping rate of 1 Hz and 512 samples per ramp. The parameters

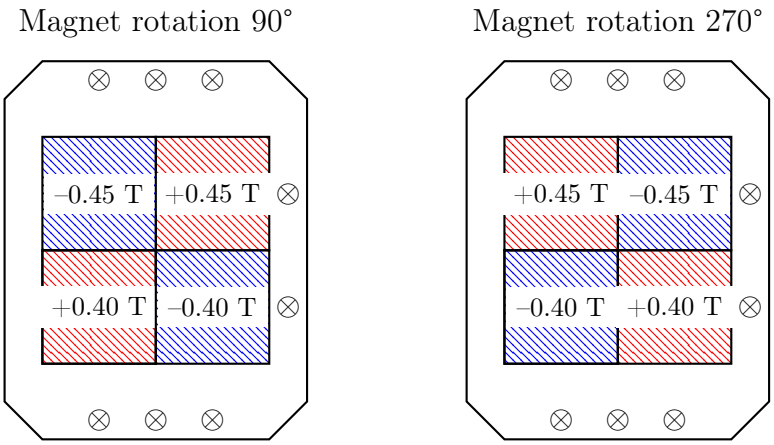

Figure 3.3: Strengths of the magnetic field on the sample stage during mc-AFM measurements for different rotations of the permanent magnet underneath.

"Deflection I Gain" and "Deflection P Gain" were set to 10 and 20, respectively, and the current sensitivity was chosen as 100 nA/V. This resulted in a slight offset of the curves which was corrected during data processing by shifting them downwards by an amount of $I(0\ \mathrm{V})$. The deflection set point of the cantilever was set to 0.100 V and the entire 200 nm × 200 nm was scanned over 100 equidistant points. While the AFM software generated two types of curves for each run – ramps from –2 V to +2 V and into the other direction –, only the ones with a negative bias start point were evaluated, as these curves tended to be less noisy; the rationale for this choice is given in Chapter 5.2.

3.3 Electronic Circular Dichroism

Another feature characteristic for chiral molecules is their absorption behavior depending on the polarization direction of light (counter- or counterclockwise); a phenomenon called "circular dichroism" (CD) in general or "electronic circular dichroism" (ECD) in particular if electronic transitions are of concern. A relationship between the strength of the CISS effect of a given molecule and its ECD spectrum could be established in as far back as 2017 [22]. However, this

relationship was mostly reduced to the rotator strength of its lowest-energy ECD absorption peak[97]

$$R_{i,j} \approx \vec{\mu}_{i,j} \cdot \vec{m}_{i,j}, \quad \text{with} \sum_{i,j} R_{i,j} = 0, \tag{3.3}$$

where $\vec{\mu}$ denote the electric and $\vec{m}$ the magnetic transition dipole moment, respectively. It was only very recently that Amsallem *et al.* found[24] that it is the magnetic – not the electronic – transition dipole moment that influences the strength of the CISS effect, by means of evaluating the absorption asymmetry factor

$$g_{\mathrm{Abs}}(\lambda) = \frac{\Delta\varepsilon(\lambda)}{\varepsilon(\lambda)}. \tag{3.4}$$

Here, $\Delta\varepsilon = \varepsilon_{\mathrm{CCW}} - \varepsilon_{\mathrm{CW}}$ is the difference in molar absorption coefficients for light with (counter-)clockwise polarization. Via Lambert-Beer's law and in the limits of a small circular dichroism, it is related to the ellipticity[98]

$$\theta = 32.98\ \Delta\mathrm{Abs} = 32.98 \cdot \Delta\varepsilon \cdot c \cdot d \tag{3.5}$$

which is more commonly measured in ECD experiments and where c are the concentration and d the path length[1]. The finding of Amsallem *et al.* is particularly useful because both transition dipole and magnetic dipole moments of a given molecule can be predicted using modern time-dependent density functional theory (TD-DFT), coupled cluster (CC), configuration interaction (CI) calculations or multireference (MR) methods. Moreover, as both $\Delta\varepsilon$ and ε linearly depend on the concentration and the path length

[1]Note that here, θ is given in units of degrees while typical measurements measure θ in millidegrees. Technically, the factor is

$$\frac{180^\circ \cdot \ln(10)}{4\pi} = 32.9821019...^\circ$$

This can be proven by defining the ellipticity of polarization in radians as $\tan[(E_R - E_L)/(E_R + E_L)]$ for two electric field vectors that are perpendicular to each other and the direction of propagation. One may then substitute the intensity together with Lambert-Beer's law $E \propto \sqrt{I_0 \exp[-A\ln(10)]}$, develop the exponentials as a first-order Taylor series and convert from radians to degrees. This is left to the reader. Note also that many sources[97] prefer rounding the factor 32.98 up to 33.00.

in absorption experiments, g_{Abs} can be easily be determined in one and the same experiment by dividing the ECD from the absorption spectrum. For example, if the ECD spectrum is measured as ellipticity in units of mdeg, one may directly obtain the absorption asymmetry spectrum via the equation

$$g_{\mathrm{Abs}}(\lambda) = \frac{1}{32982 \cdot \mathrm{mdeg}} \cdot \frac{\theta(\lambda)}{\mathrm{Abs}(\lambda)}. \tag{3.6}$$

Setup

Before spectrum collection, samples were typically separated using a Daicel Chiralpak IG column ø =20 mm, l = 250 mm, particle size 5 µm) using a Shimadzu LP6-AD together with a CBM-20A communication bus module, three valve units (FCV-20AH2, FCV-13AL, FCV-12AH), an SPD-M20A photodiode array and an FRC-10A fraction collector. During separation, the flow rate was chosen to achieve an internal pressure of ca. 20 MPa. The entire setup was controlled using `LCsolution 1.24`. After separation, the ECD spectra were recorded at room temperature using a JASCO J-1500 with a AsOne F15-UV-10 quartz cuvette (d = 1 cm). The absorption asymmetry spectra were calculated according to equation 3.6.

3.4 Computational Details

All computational methods used in this work are based upon DFT. Here, the Kohn-Sham equations are solved

$$\left[-\frac{\hbar^2}{2m}\nabla^2 + v_{\mathrm{eff}}(\mathbf{r})\right]\varphi_i(\mathbf{r}) = \varepsilon_i\varphi_i(\mathbf{r}) \tag{3.7}$$

where $\hbar$ is the reduced Planck constant, m is the electron mass, φ is the Kohn-Sham orbital with its respective energy ε and v_{eff} is the effective Kohn-Sham potential. This potential is at any point $\mathbf{r}$ composed of

$$v_{\mathrm{eff}}(\mathbf{r}) = v_{\mathrm{ext}}(\mathbf{r}) + \underbrace{q_e^2 \int \frac{\rho(\mathbf{r}')}{|\mathbf{r}-\mathbf{r}'|}\, d\mathbf{r}'}_{v_{\mathrm{coul}}} + \underbrace{\frac{\delta E_{\mathrm{xc}}[\rho]}{\delta\rho(\mathbf{r})}}_{v_{\mathrm{xc}}} \tag{3.8}$$

with an external potential v_{ext}, the Coulomb potential v_{coul} and an "exchange-correlation" potential v_{xc} which is approximated differently, depending on the choice of the employed density functional. As a "post-Hartree-Fock" method, DFT starts with a converged Hartree-Fock (HF) calculation in which the Roothaan-Hall equations

$$\mathbf{FC} = \mathbf{SC}E \tag{3.9}$$

were solved in the closed-shell case. Here, $\mathbf{C}$ is the coefficient matrix for the basis functions, $\mathbf{S}$ the overlap matrix between two basis functions $\langle j|k\rangle$ and E is the energy. $\mathbf{F}$ is the Fockian matrix to be diagonalized in this eigenvalue problem. It containing elements of the type $\langle j|\hat{F}|k\rangle$ with

$$\hat{F} = \hat{h} + \sum_{i=1}^{n/2} \left[2\hat{J} - \hat{K}\right] \tag{3.10}$$

for an n-electron closed-shell system. Furthermore, the one-electron Hamiltonian is denoted as $\hat{h}$, the Coulomb operator as $\hat{J}$, and the exchange operator as $\hat{K}$. Since in this picture, the position of one electron depends on all other electrons, the problem is solved iteratively and with a mean-field approach. For brevity's sake, an extensive treatment of the matter is forgone in this work while pointing to a handful of reference works for more information[99–101].

3.4.1 Gas-phase calculations

Setup

For the simulation of isolated molecules in the gas phase, ORCA 5.0 was used[102–104]. Convergence criteria for the self-consistent field were an energy change of $\Delta E \leq 10^{-8}$ Eh, as per the `TightSCF` keyword.

Potential energy surface (PES) scans used various density functionals including B3LYP[105] (mixing 20 % HF exchange into v_{eff} of equation 3.8), ωB97X[106] (22 % at short range and 100 % at long range) and CAM-B3LYP[107] (19 % short range, 35 % long range). In these cases, 6-311G[108], def2-TZVP[109–111] and pc-2[112–115] were used as basis sets. Where merited, metal-ligand interactions and intramolecular hydrogen bonding were modelled by

augmenting the basis to 6-311+G*[116], def2-TZVPD or aug-pc-2 on the nitrogen and hydrogen atoms of the pyrrole rings, as well as the nickel atom. When the Pople basis was used, however, nickel was augmented as 6-311-G(3df). PES scans were performed with and without Grimme's D3 dispersion correction with a zero-damping scheme[117], adding a dispersion correction term to the overall DFT energy as

$$E_{\text{disp}} = -\frac{1}{2}\sum_{i\neq j}^{N_{\text{at}}/2}\left[f_{d,6}(r_{ij})\,\frac{C_{6ij}}{r_{ij}^{6}} + f_{d,8}(r_{ij})\,\frac{C_{8ij}}{r_{ij}^{8}}\right], \tag{3.11}$$

where the sum in equation 3.11 runs over all interacting atoms i and j separated by r_{ij}, and the $C_{6,8}$ are empirical dispersion coefficients. $f_{d,6}$ and $f_{d,8}$ are damping parameters. In the case of ωB97X, Lin's D3-corrected fit[106] was used instead of ORCA's default settings.

Due to instabilities of the CISD module with the most recent `OpenMPI 4.1.4` interface in ORCA 5.0.x, **ECD spectra** were instead simulated in ORCA 4.2.1 with the B2PLYP functional[118]. Here, the exchange-correlation energy consists of 73 % exchange from the Lee-Yang-Parr functional (LYP) and 27 % exchange via second-order Møller-Plesset perturbation theory where the zeroth and first order contribution sum up to E_{HF}. The second-order contribution is

$$\Delta E_{\text{MP2}} = \sum_{a,b,i,j}\frac{|\langle ab||ij\rangle|^2}{\varepsilon_a + \varepsilon_b - \varepsilon_i - \varepsilon_j} \tag{3.12}$$

where the sum runs over all vacant (virtual) spin orbitals a, b and all occupied spin orbitals i, j. To simplify the 4-center-2-electron integrals in the numerator of equation 3.12, the "resolution of the identity" approximation was used which approximates pair products of atomic basis functions as a linear combination of auxiliary basis functions

$$\varphi_k \cdot \varphi_l \approx \sum_{\mu} C_{kl}^{\mu}\xi_{\mu} \quad \text{such that} \quad |\langle ab||ij\rangle| \approx \sum_{\mu,\nu} C_{ij}^{\mu}\langle\xi_{\mu}|\xi_{\nu}\rangle C_{ab}^{\nu}. \tag{3.13}$$

this approach was used for both the Coulomb and the exchange integrals[119], in combination with the "chain of spheres" exchange method[120] (together

referred to as RIJCOSX). The auxiliary basis was chosen automatically[121] via the `AutoAux` keyword in ORCA. Furthermore, the cc-pVTZ basis set[122–125] was used while augmenting nickel and nitrogen atoms as aug-cc-pVTZ. The innermost ten electrons of nickel were replaced by a Stuttgart-Dresden type effective core potential[126]. Solvent effects were modelled using the CPCM method[127,128] for CH_2Cl_2 as a solvent.

3.4.2 Condensed Phase Calculations

Setup

Computations involving periodic boundary conditions such as surfaces were conducted using the `pw.x` and `pp.x` utilities of the QUANTUMESPRESSO package[129–131]. The cutoff for the wavefunction and the HF exchange operator were 71 Ry. States in the SCF iterations were mixed by a factor of 0.6 with a Thomas-Fermi scheme to allow for smooth convergence. Convergence criteria were an energy change of $\Delta E \leq 4.0^{-4}$ Ry for the SCF, and changes of the total energy and forces of $\Delta E < 1.0^{-4}$ and $\Delta F < 1.0^{-3}$, respectively. All atoms were described by the density functional of Perdew, Burke and Ernzerhof[132] with a Kresse-Joubert type projector augmented wave pseudopotential (PAW) and a nonlinear core correction for non-hydrogen atoms. Grimme's empirical D3 dispersion correction was used with zero-damping.

In geometry optimizations, the charge density was cut off above 364 Ry and occupational levels were smeared by a Gaussian function using $\sigma = 0.02$ Ry. k space was evaluated at the Γ point only.

For simulation of STM images, the charge density cutoff was raised to 497 Ry and Methfessel-Paxton smearing was employed[133] with $\sigma = 0.02$ Ry. k space was evaluated using a grid of $2\times2\times1$ points that was generated with the Monkhorst-Pack scheme[134] and offset by half a grid step along vacuum direction. Calculated STM images used the Tersoff-Hamann approximation[135] which links the measured current I to the sample's wavefunction ψ_ν within the limits of a point probe:

$$I \propto \sum_{\nu} |\psi_\nu(r_{\text{tip}})|^2 \, \delta(E - E_F). \tag{3.14}$$

Here, r_{tip} denotes the distance between sample and tip and the sum runs over all states ν of the sample with their respective energies E_ν and the Fermi energy E_F.

3.4.3 Equipment and Data Processing

All molecular orbitals were rendered in Avogadro 1.2.0[136] or VMD 1.9.3[137] and pictures of crystal structures were created with VESTA 3.5.7[138]. All simulated STM data were processed with `critic2`[139,140] and plotted with `gnuplot 5.4`. Data processing, after export from Bruker's proprietary software, was handled using a custom script using `GNU Awk 5.0.1` in `GNU bash 5.0.17(1)`. All calculations were supported by the Research Center for Computational Science at the National Institutes of Natural Sciences (NINS) in Okazaki.

3.5 Complementary Methods and Materials

Instruments and materials used to acquire the data in this work were as follows:

NMR: JEOL JNM-ECS400 (^{1}H, ^{13}C, NOESY, HMQC, COSY), JEOL JNM-ECA600 (NOESY, HMQC, COSY). Unless otherwise stated, all spectra were recorded in $CDCl_3$ with 0.05 Vol.-% tetramethylsilane as an internal standard. Analysis of the data used `JEOL Delta` 5.3.1.

UV/vis: Taken on a Shimadzu UV-3600 Plus at room temperature, using an AsOne F15-UV-10 quartz cuvette (d = 1 cm) and a slit width of 2.0 mm and a time constant of 0.1 s. The machine was controlled with the provided `UVProbe 2.62` software.

EI-MS: Electron impact mass spectra were acquired using a Shimadzu GCMS-QP2010SE, increasing the temperature of the glass crucible containing the sample from room temperature to 300 °C over the course of 20 min. The internal pressure was 6.1 Pa, the temperature of the ion source was 260 °C

and the detector voltage was –0.38 V. The ionization mode was positive in all cases. The obtained spectra were evaluated using `GCMSsolution 4.52`.

AFM: Seiko Instruments S400 with an aluminium-coated SI-DF20 cantilever and a sound-proofing chamber. In the software of the machine `NanoNavi II` Version 5.61A, the "EasyMode" was used at all times. Height and phase images were evaluated in `Gwyddion 2.62`.

ESR: ESR spectra were obtained on a Bruker E500 at a concentration of 10^{-4} mol/l in $CHCl_3$ at 150 K with a frequency of 9.66 GHz at the X band, an attenuation of 23 dB, a modulation amplitude of 5 Gs and a time constant of 164 ms.

Cyclic Voltammetry: Recorded using a CH Instruments CHI 610A against a standard calomel electrode (provided by BAS Japan). Solutions were in benzonitrile (PhCN) at concentrations of 20 mg in 30 ml (ca. 0.03 mM) with 0.1 M tetrabutylammonium perchlorate as an electrolyte. The PhCN was stored over 4 Å molecular sieve in a round-bottom flask sealed with parafilm, and purged with argon at room temperature for 30 min prior to use.

X-ray Diffractometry: All data for the provided crystal structures were collected on a Rigaku HyPix-AFC with Mo Kα radiation. The cathode was held at 50 kV and 16 A, and the detector was held at a distance of 25 mm. Data was further refined with ShelXL[141], ShelXT[142] and OlexSolve using CrysAlis Pro SM and Olex2[143].

IR Spectroscopy: Taken with a Bruker IFS66v/S spectrometer as a CsI pellet of ø=5 mm. Spectra were acquired over 32 scans at a resolution of 2 cm^{-1} with a globar as the light source, KBr as a beam splitter and deuterated triglycine sulfate (DTGS) as a detector.

Silicon wafers: Boron-doped, diameter 100 ± 0.3 mm, thickness 350 ± 20 µm, resistivity $<0.02\,\Omega$ cm, surface orientation (100). Supplied by Electronics and Materials Corporation Limited. These wafers were cut into squares of 2 cm length before further processing. Before deposition of additional layers, the wafers were first cleaned with a sequence of acetone, isopropanol and another round of acetone, then cleaned with an RF oxygen plasma using a Samco FA-1 with an Elite 300HD-01RF, running at a power of 10 W for 5 min.

Mica substrate: Natural-grade and supplied by Nilaco Corporation, Tokyo. For processing, the mica was cut into squares of ca. 1 cm length and then cleaved with adhesive tape at least five times.

Physical vapor deposition: Via magnetron sputtering, using a Quorum Q300T D with argon as the plasma source at a pressure of 10^{-2} mbar. Sputter currents were 20 mA for Au, and 100 mA for Ni and Ti. Only in Chapter 4.6.2, an in-house RF sputtering apparatus with annealing capability was used, provided by the Instrument Center of the National Institute of Natural Science Okazaki. Here, the argon pressure was 1 Pa and the sputtering was controlled by adjusting the RF power (100 W for Au and 200 W for Ti targets). Sputter targets were supplied by Furūchi Chemicals. Both physical vapor deposition and spin-coating (see below) were always performed on the same day that the wafers were cleaned (silicon wafers) or cleaved (mica), typically within one hour. In cases were this was not possible, the wafers were spun with an AZ 1500 photoresist and then cured at 80 °C for at least one hour before storing them until further processing. The photoresist could be removed with isopropanol and acetone.

Spin-coating: At all times, samples were spin-coated as 40 µl toluene solutions at different concentrations, spinning the substrate at 2,500 min^{-1} for thirty seconds. The drops were deposited once the spin-coater – a Mikasa Opticoat MS-B100 – had reached the desired speed. All prepared surfaces were stored in a vacuum desiccator, purging once with argon gas before drawing vacuum down to 0.02 MPa (0.2 bar, 150 torr). Solutions for spin-coating could be kept at –22 °C indefinitely, provided that the caps of the vials were sealed with Parafilm.

Chapter 4

Results

4.1 Isomerism in H_3TPBV

As briefly mentioned in its Chapter 3.1.6, the photooxidation of Mg(TPP) · 2 Py under strictly water-free conditions (the late variant) gave *EZZZ*-H_3TPBV together with the product in approximately equal yield. This assignment can be made on the basis the coupling of a pyrrole hydrogen with a β-pyrrole hydrogen atom in the H,H-COSY spectrum. While this kind of isomerism has been well documented in literature by Falk[77,144–147], the interconversion by thermal means (and seemingly also via Lewis acid-catalysis) is surprising, as this reaction has thus far only been shown to be proceed with light, of which there is arguably plenty during the photocleavage of Mg(TPP). The fact that *EZZZ*-H_3TPBV could be isolated from reaction in $CHCl_3$ but not toluene shows that the equilibrium between *EZZZ* and *ZZZZ* is highly solvent-dependent. Indeed, as Falk described earlier[144,145,147], this is the case in many oligopyrroles. Because it was not possible to separate the *EZZZ* isomer with a chiral HPLC (with any eluent composition, only one single peak eluted), both helicities are likely to rapidly racemize. Hence, further work on this molecule was not conducted.

4.2 Geometrical Structure

4.2.1 Ni(TPBT) and H_2TPBT

For study of the CISS effect, the most striking feature of the open-chain tetrapyrroles is certainly their helicity. Here, x-ray crystallographic data obtained of Ni(TPBT) showed that the 20-phenyl group of Ni(TPBT) aligns along the rest of the tetrapyrrole helix; a configuration referred to as "syn-periplanar" (*sp*). The result is a well-defined helix in which all participating atoms are sp^2-hybridized. The helix' pitch, radius and overall height can be estimated as 3.5 Å, 3.2 Å and 5.7 Å, respectively. Overall, the helix spans approximately one and a quarter turns, as opposed to Ni(OEFB)[70] with approximately on full turn. This already allows for a first benchmarking approach of the CISS effect by evaluating their spin polarization depending on the helix length (discarding possible contributions from the different substitution pattern).

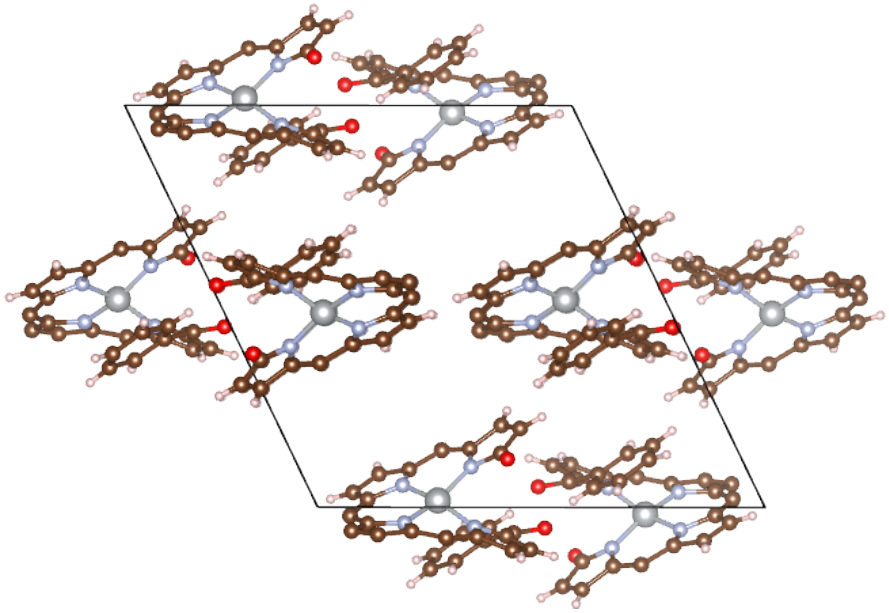

Figure 4.1: Crystal structure of a *rac*-Ni(TPBT), viewed along the *b*. The 20-phenyl group is located on the bottom part of the figure, syn-periplanar to the molecular helix. $C{=}O_{Lactam}$ faces away from the reader. Phenyl groups in 5-, 10- and 15-position as well as solvent molecules are omitted.

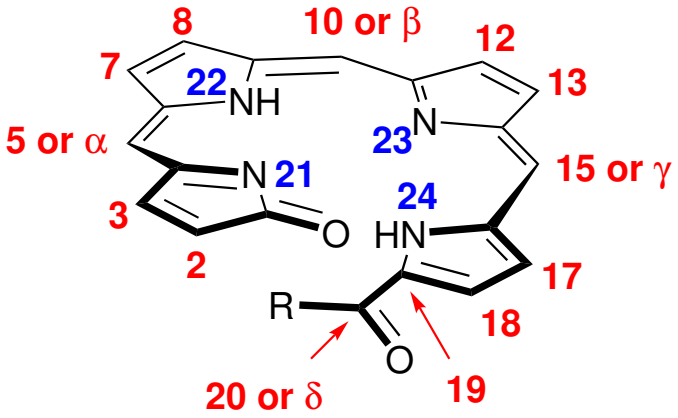

Figure 4.2: Numbering scheme of the bilatrienone helix, following the recommendations of Falk[147].

In Ni(TPBT), the space group found upon crystallization from $CHCl_3$ at room temperature is $P2_1/c$, indicating an achiral crystal structure containing both (M) and (P) isomers. Both are easily identified in Figure 4.1 as each one half of an (M)- and (P)-pair. The lattice parameters are a = 16.346 Å, b = 14.436 Å, c = 16.6793 Å, and β = 114.852(5)°.

4.2.2 *ap*/*sp* Interconversion in Ni(TPBT) and H_2TPBT

Finding Ni(TPBT) in the *sp*-configuration is rather surprising, considering that DFT-based calculations by the Mizutani work group[80] predicted the free-base H_2TPBT to adapt an "anti-periplanar" (*ap*) configuration. This raises the question whether both *ap* and *sp* are interconvertible and if so, how large their interconversion barrier is. To obtain reasonable estimates, a potential energy surface (PES) scan of a single Ni(TPBT) was performed by twisting the 20-phenyl group, represented by the dihedral angle spanned by C(18-20) and the *ipso* carbon for R = Ph in Figure 4.2. This angle was varied in steps of 10°, starting at the value observed in the crystal structure (142.1°) and ending at an angle of –37.9°, i.e. a 180° rotation. The geometries obtained by these incremental rotations were then optimized further, keeping only the above twisting angle fixed ("relaxed PES scan"). The presence of phenyl groups and the seemingly favored *sp*-configuration suggested that dispersive

interactions between the 20-phenyl group and the rest of the molecules play a substantial role in this problem. In this case, the exchange-correlation energy, one of the core entities in DFT calculations, can become range-dependent. To account for this fact, the PES scans were performed using three different density functionals: B3LYP as the most commonly employed range-unseparated functional in modern DFT, as well as CAM-B3LYP and ωB97X as two range-separated variations. Furthermore runs of all three employed functionals were performed with and without Grimme's empirical D3 correction. For the runs employing ωB97X with dispersion correction, the ωB97X-D3 functional was used instead of a combination of ωB97X and D3. This overall approach resulted in comprehensive study of $3 \times 3 \times 2 = 18$ separate PES scans, with the most important findings summarized here.

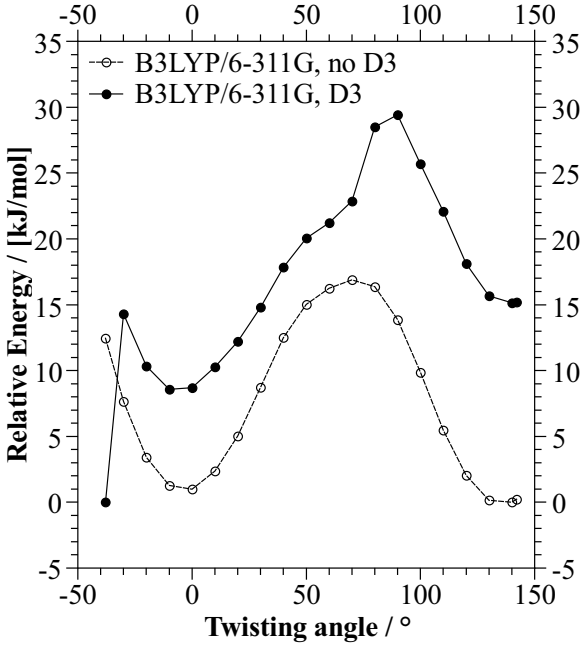

Figure 4.3: Results of PES scans of a Ni(TPBT) molecule using the B3LYP functional with the 6-311G basis set (a) with (b) without Grimme's D3 dispersion correction. Basis set augmentations for nickel and nitrogen were made according to the main text.

Figure 4.3 shows the result of two separate PES scans performed with B3LYP/6-311G, with data points for dispersion correction in shaded dots and with dispersion-less data points hollowed out. As can clearly be seen, applying the dispersion correction during the PES scan stabilizes the *sp* over the *ap*-isomer; in this case, by ca. 5 kJ/mol with an activation barrier of 15 kJ/mol (*sp* → *ap*) or 21 kJ/mol (*ap* → *sp*). Of all nine D3-corrected PES scans, only the range-separated functionals correctly predict the *sp*-conformation to be energetically favored over the *ap*-conformation. Interestingly, B3LYP/6-311G and B3LYP/def2-TZVP predict the wrong conformation to be stable with D3 correction, whereas the right one was predicted without. This rather peculiar behavior of B3LYP integrates into a series of other shortcomings of the functional[148–151], especially when used in combination with basis sets of the Pople family. Considering only the most accurate combinations of CAM-B3LYP and ωB97X-D3 with the three basis sets, the twisting angle for the hypothetical *ap* isomer is –10° ± 0° which is energetically disfavored by 11.9 ± 6.3 kJ/mol over *sp*. The activation energy for conversion from *ap* to *sp*-isomer (142.1°) is 14.8 ± 2.0 kJ/mol and 26.7 ± 7.7 kJ/mol for *sp* → *ap*. For comparison, the chair conformation in cyclohexane is more stable than its boat conformation by 21 kJ/mol with an activation energy of 43 kJ/mol (chair → half-chair) conformation[91]. These results obtained by the range-separated functionals clearly show that attractive dispersion interactions between the 20-phenyl group and the rest of the conjugated helical TPBT molecule stabilize the formation of a well-defined helix.

The information about the precision of the above-mentioned functionals also aid as a starting point for the same PES scans conducted on the free-base H_2TPBT whose crystal structure could not be obtained. Taking the two different protonation patterns in the free-base into consideration, the *ap*-22,24*H* isomer (see Figure 4.4) was found to be the most stable and separated from its 22,24*H* isomer by a minute 3.7 kJ/mol. The 21,23*H* protonation pattern is considerably higher in energy, by 191.6 kJ/mol. Here, the *ap*/*sp* isomers are even closer in energy and separated by less than 1 kJ/mol. Because in both protonation patterns, the energy differences for *ap*/*sp* are less than 4 kJ/mol – a value considered considered as “chemical accuracy”, i.e the

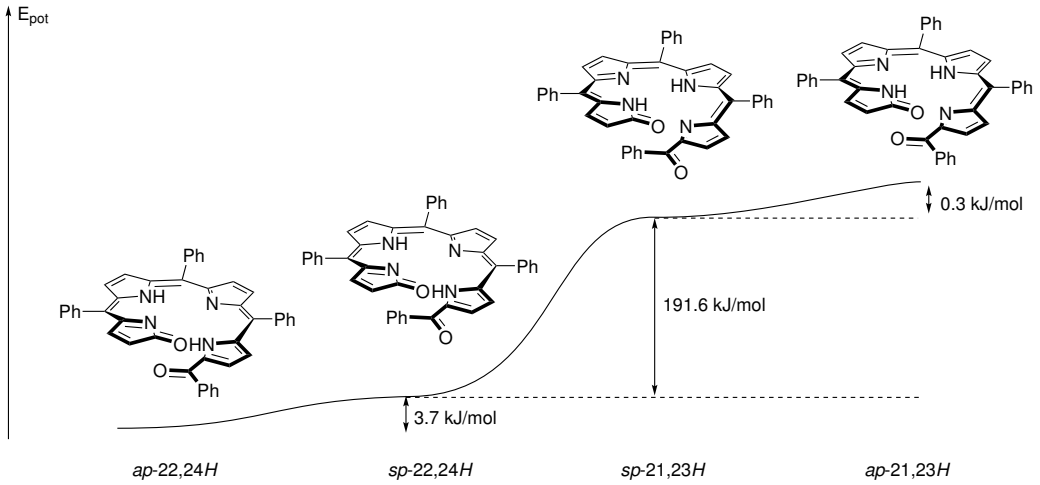

Figure 4.4: Comparison between the potential energies of H_2TPBT isomers. The solid line serves as a guide to the eye.

accuracy needed to make accurate chemical predictions[152] – and the accuracy of modern DFT functionals falls into the range of 8–13 kJ/mol[152], it should become clear that based on these results, rapid *ap*/*sp*-interconversion can be expected in H_2TPBT at room temperature. Moreover, it is not outright clear whether the distinction between the protonation patterns can be made quite clearly, as the four pyrrole rings are in close proximity to each other in the molecule and are thus expected to exchange their two protons rapidly. Thus, it becomes quite evident that metal-free H_2TPBT is not suitable for the use in spintronics. Consequently, further work with this molecule was not pursued.

4.2.3 Ni(OEFB) Hydrate

These structural differences between H_2TPBT and its metal complexes notwithstanding, both have in common that small nucleophiles (especially water and methanol) can attack the carbon atom in 15-position to form a stereocenter and interrupt the π-conjugation of the TPBT helix. This phenomenon has been subject of thorough study elsewhere[78,80,86], along with an early application of the resulting covalent hydrate in a molecular switch[79]. While this compound could not be crystallized in this work, it was possible

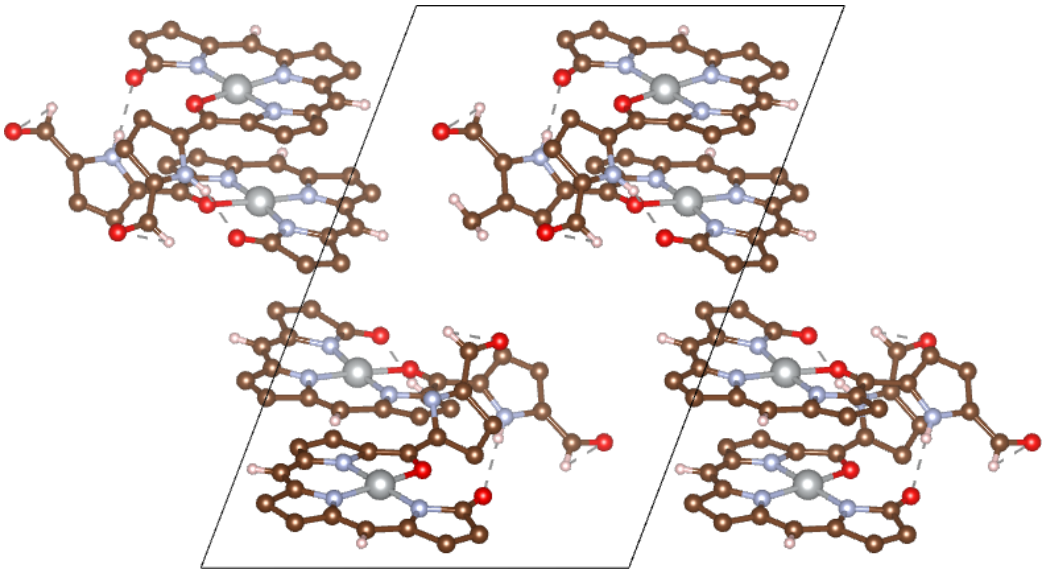

Figure 4.5: Dimers of (M/P)-Ni(OEFB) hydrate found in its crystal structure, viewed along the *a* axis of the crystal. Note the opening of the molecular helix and the different coordination partners of the nickel atom, as well as the stabilization by intermolecular hydrogen bonding. Ethyl groups are omitted for clarity.

to obtain the crystal structure (Figure 4.5) of the same molecule with an octaethyl-substitution pattern as a nickel complex. This molecule could be obtained by photocleavage[70] of Mg(OEP) · 2 py in 10 % yield, previously unreported in literature.

From this crystal structure, it becomes obvious that the coordination behavior of the central metal atom is not limited to the nitrogen atoms of the tetrapyrrole. Much rather, the oxygen atom in the 15-position is predominantly coordinated so that the adjacent pyrrole ring flips out of the helical structure and stabilizes another molecule of opposite helicity via >N–H$\cdots$O= hydrogen bonding. This flexibility of the pyrrole ring is obviously not limited to one direction (clockwise/anticlockwise motion) so that it is reasonable to expect racemization if this nucleophilic attack of the water molecule takes place in the enantiopure compound, even with bulkt phenyl substituents. Moreover, it is reasonable to assume that in this configuration of the hydrate, any hypothetical *ap* or *sp* configurations will rapidly interchange in solution.

For this reason, work with the covalent hydrate of Ni(TPBT) – as was done by Kita *et al.* in the case of racemic Zn(TPBT) hydrate[78] – was not pursued.

4.3 Electronic Structure and Noninnocence

Much like with the porphyrins[153], the coordination behavior of the open-chain tetrapyrroles is not limited to nickel as the central atom but is known to include zinc[78,79,86] and cadmium[61] in the tetraaryl case and cobalt[70], nickel[70], copper[70] and zinc[75] in the octaethyl case. In the case of octaethylbilindiones – where the benzoyl group of TPBT is replaced by oxygen – coordination with manganese[67], iron[66] and even palladium[72,154] was successful. Trying to expand the "periodic table of TPBT" in a similar fashion, metalation with copper indeed gave the expected Cu(TPBT). However, it was found that much like Cu(OEFB)[155], the resulting complex showed noninnocent behavior, i.e. an absence of clear signals in ^{1}H-NMR spectra and a clear signal in EPR experiments.

This integrated EPR spectrum for a 10^{-4} mol/l solution in $CHCl_3$ at 150 K is given in Figure 4.6 where a clear peak from the copper atom is visible at ca. 3,360 Gs and a smaller peak appears at ca. 3,570 Gs which arises from the contribution of an organic radical. Fitting Lorentzian peak shapes at the respective positions, the g^{ESR} values may be obtained via the position of their centers x_c. Doing so, it was found that $g^{\mathrm{ESR}}_{\mathrm{Cu}} = 2.0547$ and $g^{\mathrm{ESR}}_{\mathrm{Ligand}} = 1.9333$ which is in good agreement with the work of Subramanian *et al.*[155] who found approximately $g^{\mathrm{ESR}}_{\mathrm{Cu}} = 2.0697$ and $g^{\mathrm{ESR}}_{\mathrm{Ligand}} = 2.0081$ for Cu(OEFB). The UV/vis spectra of Ni(TPBT) and Cu(TPBT) as 10^{-5} mol/l solutions in CH_2Cl_2 are given in Figure 4.7.

Notable differences in the noninnocent Cu(TPBT) are the much weaker absorption in the 600 nm region as well as the split of the 800 nm absorption band, a phenomenon also absorbed in Cu(OEFB) by Koerner *et al.*[70]. Because Asano *et al.* observed an absorption peak in the same region when dehydrating the hydrate of the free-base H_2TPBT[80], because Smith *et al.* observed $\lambda_{\mathrm{max}} = 850$ nm in Cd(TPBT)[61], and because H_3TPBV is missing

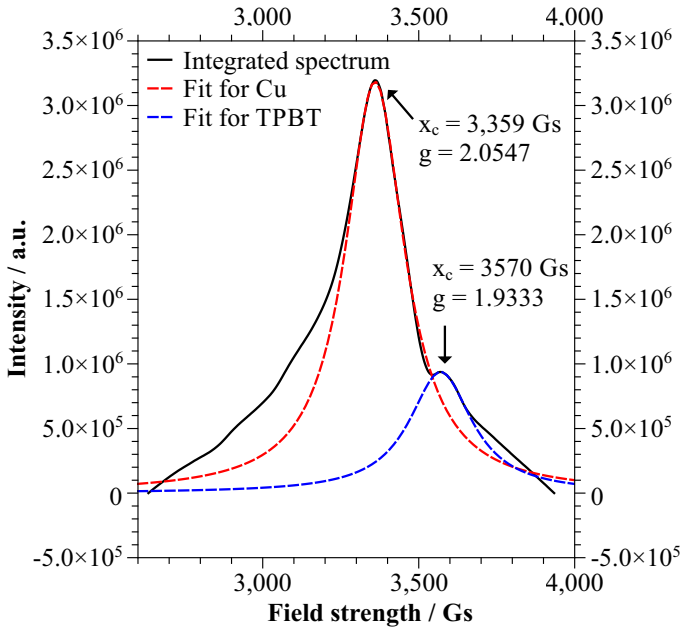

Figure 4.6: ESR results for Cu(TPBT) as a 10^{-4} mol/l solution in $CHCl_3$ at 150 K. Both Lorentzian fits were obtained from a Levenberg-Marquardt algorithm with a tolerance of 0.0001, and have values of R^2(Cu) = 0.9986 and R^2(TPBT) = 0.9996.

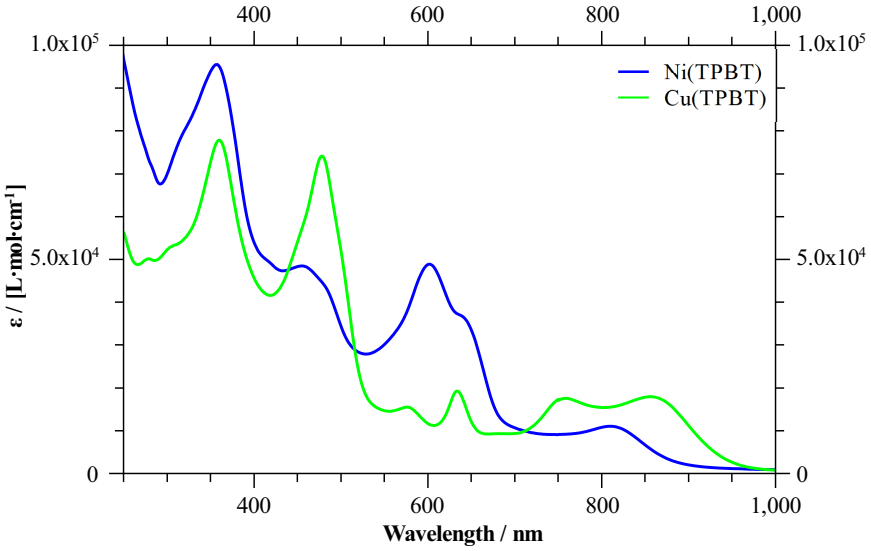

Figure 4.7: Room-temperature absorption spectra of Ni(TPBT) and Cu(TPBT) as 10^{-5} mol/l solutions in CH_2Cl_2.

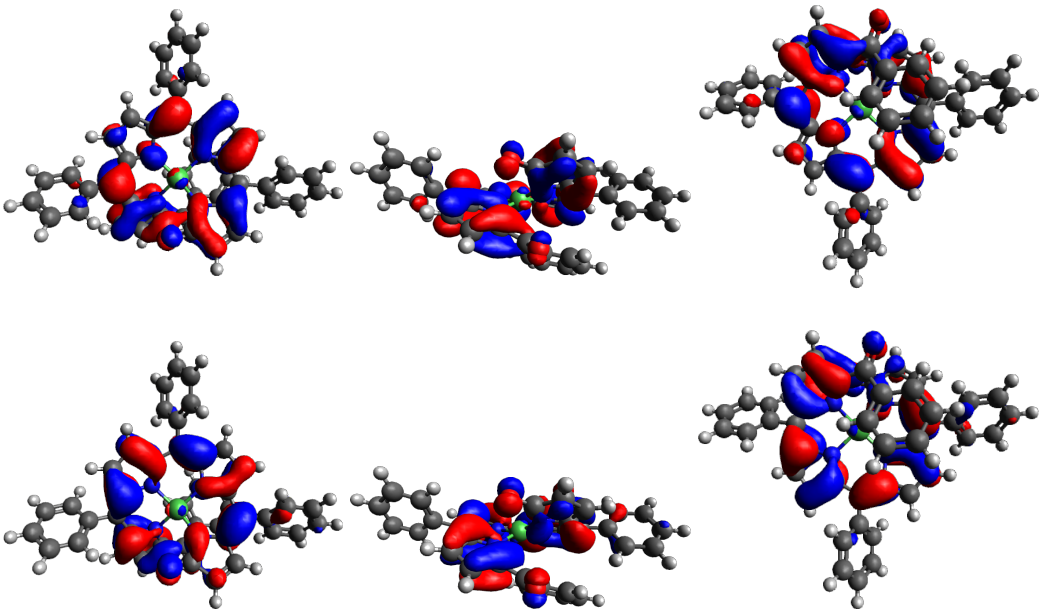

Figure 4.8: Bottom, front and top views of the LUMO+0 (–1.8066 eV, top row) and HOMO-0 (–6.9748 eV, bottom row) of Ni(TPBT), calculated using the ωB97X-D3 functional with the def2-TZVP basis set and an isosurface value of 0.025.

such a band, this HOMO-LUMO transition can only originate from the TPBT ligand and is clearly not a *d*-*d* transition or attributable to metal-to-ligand charge transfer (MLCT). Further evidence is provided by the frontier orbitals of Ni(TPBT) which were calculated using the ωB97X-D3 functional with the def2-TZVP basis set – a combination that seems adequate, given its good performance in the PES scans.

The structures of the HOMO and the LUMO, given in Figure 4.8 for an isosurface value of 0.025 (where $iso \propto \Psi^2 \in [0;1]$) clearly show no involvement from the *d* orbitals of the central nickel atom. Much rather, these contributions (obtained via Löwdin population analysis) are only visible for HOMO-2 (–8.5991 eV, Ni d_{xz} 11.5 %), HOMO-3 (–8.6690 eV, Ni d_{yz} 10.2 %) and HOMO-4 (–8.7857 eV, Ni d_{z^2} 16.1 %). It should also be noted that in these helical frontier orbitals, the overlap between two adjacent turns is very low and only observable for an isosurface value of ≤ 0.023 in the HOMO

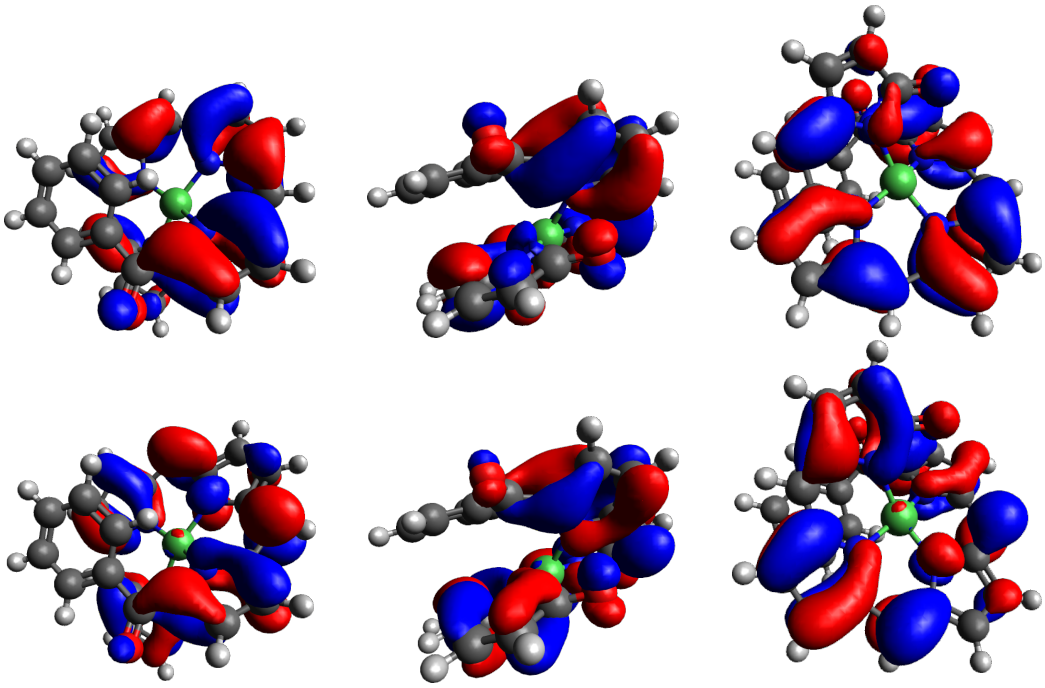

Figure 4.9: Frontier orbitals of truncated Ni(TPBT), obtained via calculation with the B2PLYP functional and the cc-pVTZ basis set. Augmentations are mentioned in the main body. Shown in the top row is LUMO+0 (MO 117) at –0.08872 Eh (–2.4142 eV) and shown in the bottom row is HOMO-0 (MO 116) at –0.22253 Eh (–6.0553 eV).

(overlap of two $\pi_{C=C}$ orbitals of the pyrrole rings) and 0.014 ($\pi_{C=C}$ with $\pi^*_{C=O}$) in the LUMO, i.e. this overlap is generally smaller in the LUMO. These findings remain qualitatively accurate even when more sophisticated methods such as second-order Møller-Plesset perturbation theory are used (Figure 4.9), while noting that for these calculations, the phenyl groups in 5-, 10- and 15-position were truncated to mitigate the drastic scaling of this method. While a more thorough discussion of the respective ECD-active transitions follows in the next section, the results presented here – small intrahelical orbital overlap, highly receptive HOMO-LUMO transition, and potential for noninnocence – are encouraging for the CISS measurements in Chapter 5.

4.4 Separability and Enantiostability

4.4.1 Ni(TPBT)

While the results thus far clearly show that helical tetrapyrroles of the TPBT and OEFB family are promising in showing the CISS effect, two important properties have thus far been overlooked: The separability of the two helicities and their enantiostability after separation. Hence, nickel and copper complexes of TPBT, Ni(OEFB) and H_3TPBV were run through a 25 cm Daicel Chiralpak IG column with varying eluent compositions, maintaining an internal pressure of ca. 20 MPa throughout the experiments.

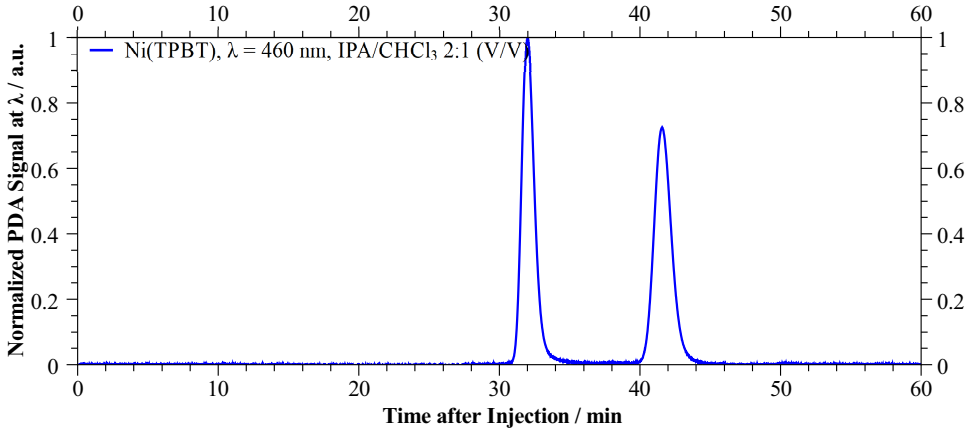

Figure 4.10: Left: HPLC chromatogram of *rac*-Ni(TPBT) using a Daicel Chiralpak IG column with isopropanol/$CHCl_3$ 2:1 (V/V.) Right: ECD spectra of the first fraction, taken in the eluent after 0–28 days. Arrows indicate the spectral changes over time.

Upon testing mixtures of isopropanol, chloroform, ethyl acetate, hexane as well as the neat solvents, it was found that Ni(TPBT) can be comfortably separated at baseline using a 2:1 mixture of isopropanol and $CHCl_3$, with the respective HPLC chromatogram given in Figure 4.10. The obtained fractions, even when taken directly after the column with large amounts of (potentially nucleophilic, see earlier) isopropanol, retain their helicity when stored in a sealed vial over the course of at least four weeks: Spectral changes are barely noticeable and arguably range within the error margin arising from

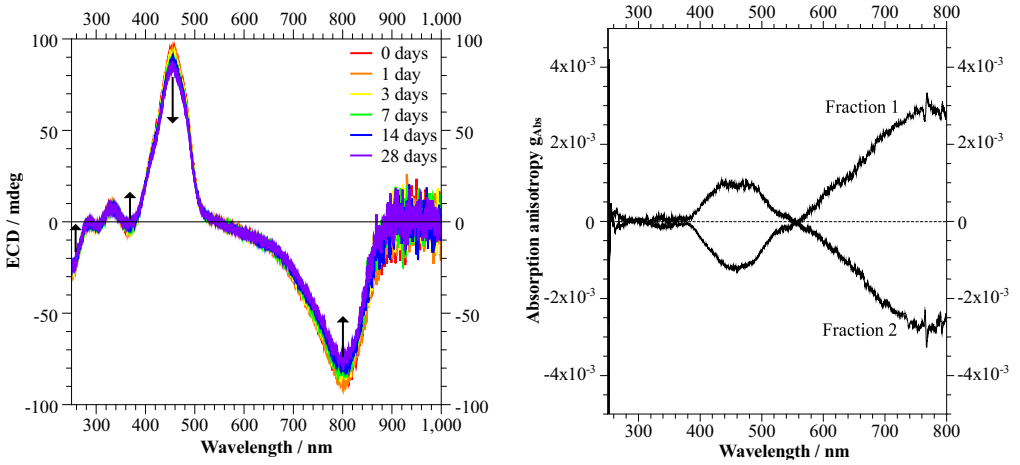

Figure 4.11: Left: ECD spectra of the first fraction of Ni(TPBT), taken in the eluent after 0–28 days. Arrows indicate the spectral changes over time. Right: Absorption asymmetry spectrum of both fractions, taken in CCl_4.

the signal-to-noise-ratio at any given wavelength. The ECD spectra over the course of up to four weeks, among with the absorption asymmetry spectrum in CCl_4 are given in Figure 4.11 where the g value of ca. 3×10^{-3} for the HOMO-LUMO transition is unexpectedly large.

However, as it was not possible to crystallize the enantiomers, the elution order was ambiguous. To solve this issue, the ECD spectra were simulated for the (M)-isomer using the B2PLYP functional and the cc-pVTZ basis set with augmentations made according to Chapter 3.4.1; an approach that was motivated by Goerigk and Grimme[156] who obtained accurate ECD spectra with this method. Because mixing correlation energy from second-order Møller-Plesset theory into the exchange-correlation energy drastically increases the scaling, the phenyl groups in 5-, 10- and 15-positions were substituted by hydrogen atoms. The resulting simulated spectrum, given in Figure 4.12, shows good agreement with experiments, within the approximations mentioned earlier and show that the (M)-Ni(TPBT) leaves the chiral column first.

From the B2PLYP results, it was also possible to obtain further information about the HOMO-LUMO transition, that has been shown to correlate with the CISS effect for half a decade[21–24,157]. The most important entities of note are the rotator strength and the alignment of the transition dipole moment with

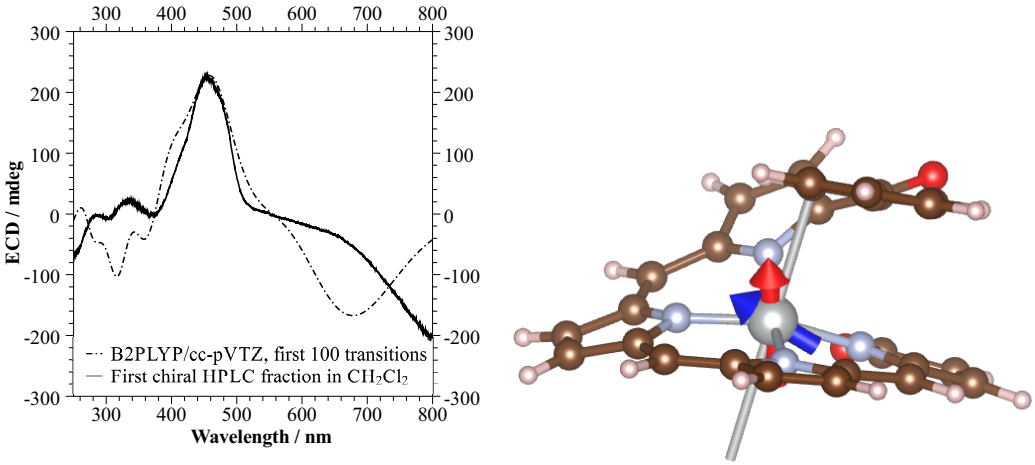

Figure 4.12: Left: Experimental ECD spectrum for (M)-Ni(TPBT) (solid line) and the predicted spectrum for the same molecule with 5-, 10- and 15-phenyl groups substituted by hydrogen atoms, using the cc-pVTZ basis set and the B2PLYP functional (dashed black line). Calculated spectrum is normalized with respect to the experimental one. Right: Structure of the Ni(TPBT) molecule used for the B2PLYP TD-DFT calculations. Given as a grey line is the normal vector of the plane spanned by the bottom three nitrogen atoms. Arrows represent the magnetic transition dipole moment of the ECD-active HOMO-LUMO transition (red) and the predicted transition at 467 nm (blue, scaled by a factor of two). The angle spanned by the red vector and the helical axis is ca. 19.7°.

the helical axis, as these are currently believed to enhance chirality-induced spin selectivity. Here one may find $R_{\mathrm{B2PLYP}} = -6.3932 \cdot 10^{-42}$ cgs and 19.7°, respectively.

4.4.2 Cu(TPBT)

While the copper analog, Cu(TPBT) could be similarly separated with ease (see Figure 4.13), the two fractions were essentially ECD-silent despite the high HT values measured at the ECD detector briefly after leaving the column[1]. The exact cause of this behavior is unknown, but it seems reasonable to assume

[1] As the ECD spectra were measured on a separate machine at the National Institute for Physiological Science (NIPS) at the Yamate campus in Okazaki, the time delay between leaving the column and the ECD measurement was typically 20–30 min.

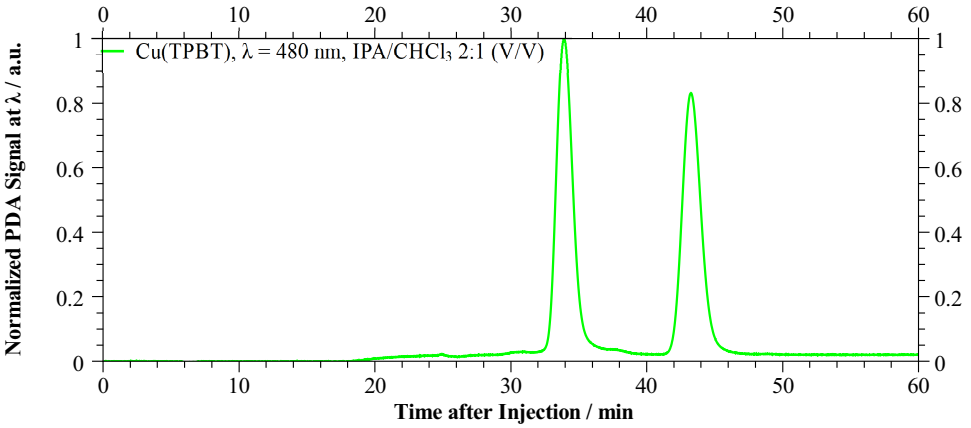

Figure 4.13: HPLC chromatogram of *rac*-Cu(TPBT) using a Daicel Chiralpak IG column with isopropanol/$CHCl_3$ 2:1 (V/V).

that the observed noninnocence of this compound may be a contributing factor. The most likely pathway currently appears to be homolytic cleavage of a Cu–N bond which would enable rapid re-racemization via twisting of a pyrrole ring, similar to the mechanism proposed for the covalent hydrate of Ni(OEFB). Whether the Cu(TPBT) enantiomers can be stabilized – for example via adsorption on a chiral substrate[158] or interactions with a ferromagnetic substrate[50] – is currently speculated.

4.4.3 Ni(OEFB)

A similarly frustrating issue was encountered when trying to separate Ni(OEFB). This compound was completely inseparable in any mixture of isopropanol and $CHCl_3$, including the neat solvents. The separation was possible at baseline by using a 1:1 mixture of ethyl acetate and hexane (Figure 4.14), while noting that the solubility was so low that 3 l of eluent had to be used to obtain amounts of the enantiopure substance in the lower double-digit milligram regime. However, the resolved enantiomers were equally stable as their tetraphenyl analog Ni(TPBT) and a racemization could not be observed over the course of four weeks (see Figure 4.15). This result comes as a surprise considering that Mizutani *et al.* found rapid racemization[74,75] of zinc aetiobiliverdin-IV γ, where the formyl group is substituted by a methyl ether.

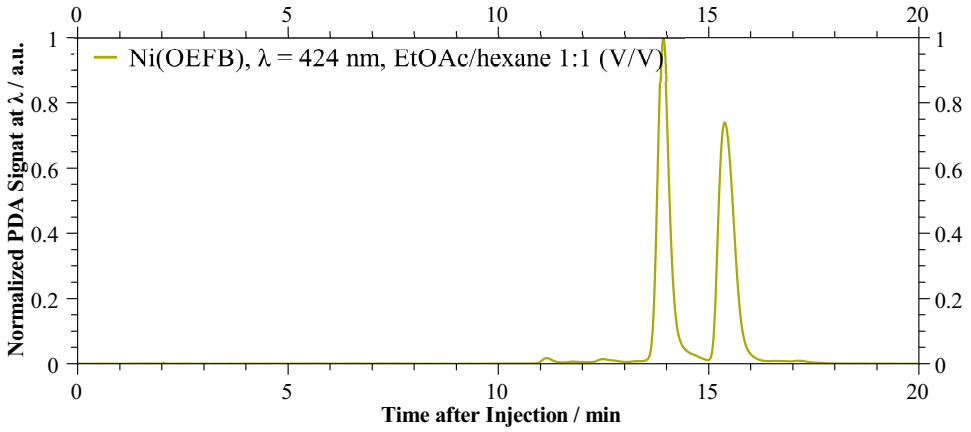

Figure 4.14: HPLC chromatogram of *rac*-Ni(OEFB) using a Daicel Chiralpak IG column with EtOAc/hexane 1:1 (V/V).

The enantiostability of Ni(OEFB) is then likely caused by intramolecular hydrogen bonding between the formyl hydrogen and the oxygen of the opposite lactam ring, rather than by sterical hindrance. Moreover, of all the molecules investigated in this work, it showed by far the largest g_{Abs} at a value of 10^{-2}. Correspondence between theoretical and experimental ECD spectra was similar: Here, the rotator strength is $R_{\mathrm{B2PLYP}} = 5.3701947 \cdot 10^{-42}$ cgs, and the HOMO-LUMO magnetic transition dipole moment and the helical axis span an angle of 16.9°. It is also noted that, although the ECD spectra were simulated for the (M)-enantiomers of both Ni(TPBT) and Ni(OEFB), their HOMO-LUMO transition has an opposite ECD sign.

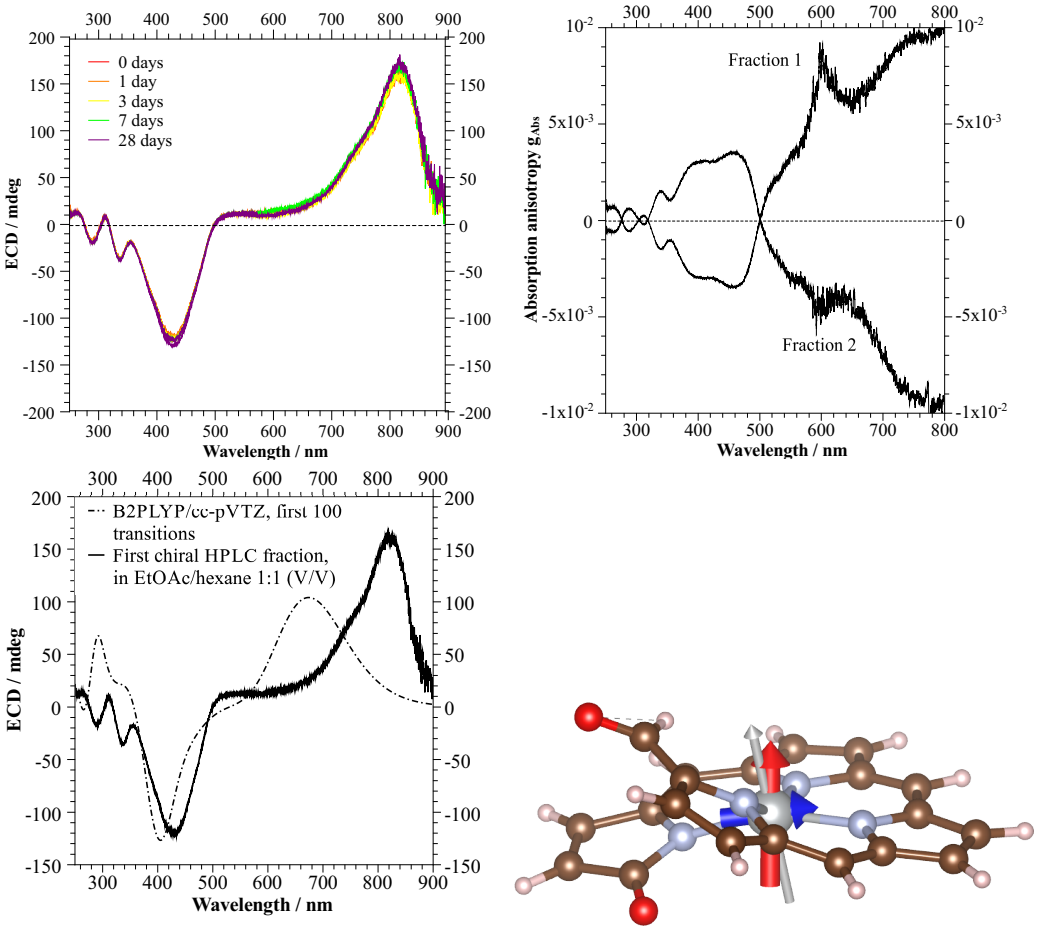

Figure 4.15: Top left: ECD spectra of the first fraction of Ni(OEFB), taken in the eluent after 0–28 days. Arrows indicate the spectral changes over time. Top right: Absorption asymmetry spectrum of both fractions, taken in the HPLC eluent. Bottom left: Experimental ECD spectrum for (M)-Ni(OEFB) (solid line) and the predicted spectrum for the same molecule with ethyl groups substituted by hydrogen atoms, using the cc-pVTZ basis set and the B2PLYP functional (dashed black line). Calculated spectrum is normalized with respect to the experimental one. Bottom right: Structure of the Ni(OEFB) molecule used for the B2PLYP TD-DFT calculations. Given as a grey line is the normal vector of the plane spanned by the bottom three nitrogen atoms. Arrows represent the magnetic transition dipole moment of the ECD-active HOMO-LUMO transition (red) and the predicted transition at 402 nm (blue, scaled by a factor of five). The angle spanned by the red vector and the helical axis is ca. 16.9°.

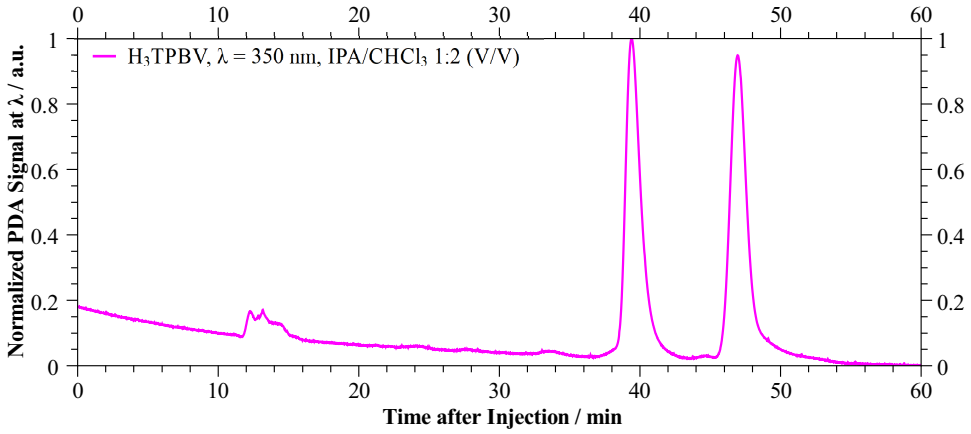

Figure 4.16: HPLC chromatogram of *rac*-H_3TPBV using a Daicel Chiralpak IG column with isopropanol/$CHCl_3$ 1:2 (V/V). Eluting at 14 min is an irreproducible impurity.

4.4.4 H_3TPBV

The separation and enantiostability of H_3TPBV, obtained from photocleavage of Mg(TPP), was equally good at higher solubility in the eluent. However, the *EZZZ* isomer eluted as one single band with every eluent tried (EtOAc, hexane, IPA, $CHCl_3$, and mixtures thereof) and the fraction was ECD silent, indicating that it rapidly racemizes even on the column. Moreover, contaminations of the *ZZZZ* isomer with this molecule made the separation considerably more difficult as their peaks could not be separated at baseline, making the separation considerably lossy.

While for this molecule, no ECD spectrum has been simulated yet (these efforts are currently ongoing), the assignment of the HPLC fractions – the (M)-isomer elutes in the early fraction – is likely the same as in the previous compounds. In the experimental absorption asymmetry spectrum, the highest ECD-active transition has a Kuhn factor of 5×10^{-4}, the lowest of the investigated molecules.

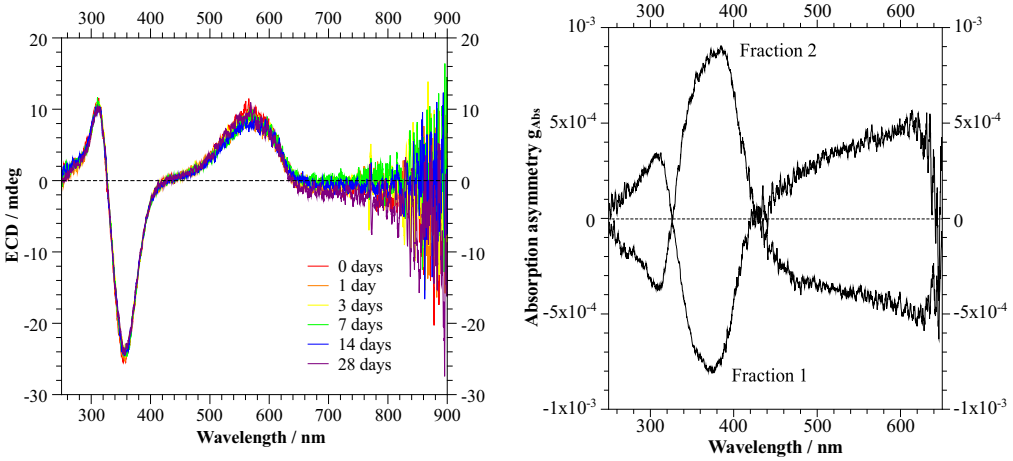

Figure 4.17: Left: Spectral changes in the ECD spectrum of the first fraction of H_3TPBV, taken in the eluent. Right: Absorption asymmetry spectrum of both fractions, taken in the eluent.

4.5 Cyclic Voltammetry

The use of cyclic voltammetry in this work appeared justified not only because related natural products like biliverdin are redox-active but also because the mc-AFM measurements rely on the transport in electrons. As such, the resulting $I(V)$ curves from which the spin-polarization is obtained may become enhanced or suppressed in the vicinity of bias values where electrochemical reactions take place. In addition, cyclic voltammograms may give more information about the relationship between the TPBV and the TPBT ligand since, if both show oxidation and reaction at similar voltages, a redox reaction can be established. This, in turn, may provide grounds for further work with these molecules towards coated electrodes for spin-dependent redox reactions, as has been done in the case of water-splitting[35,39]. To these ends, cyclic voltammograms (Figure 4.18) were recorded for Ni(TPBT), Cu(TPBT) and Ni(OEFB) while similar data for Ni(OEFB) was already recorded by Koerner *et al*[70].

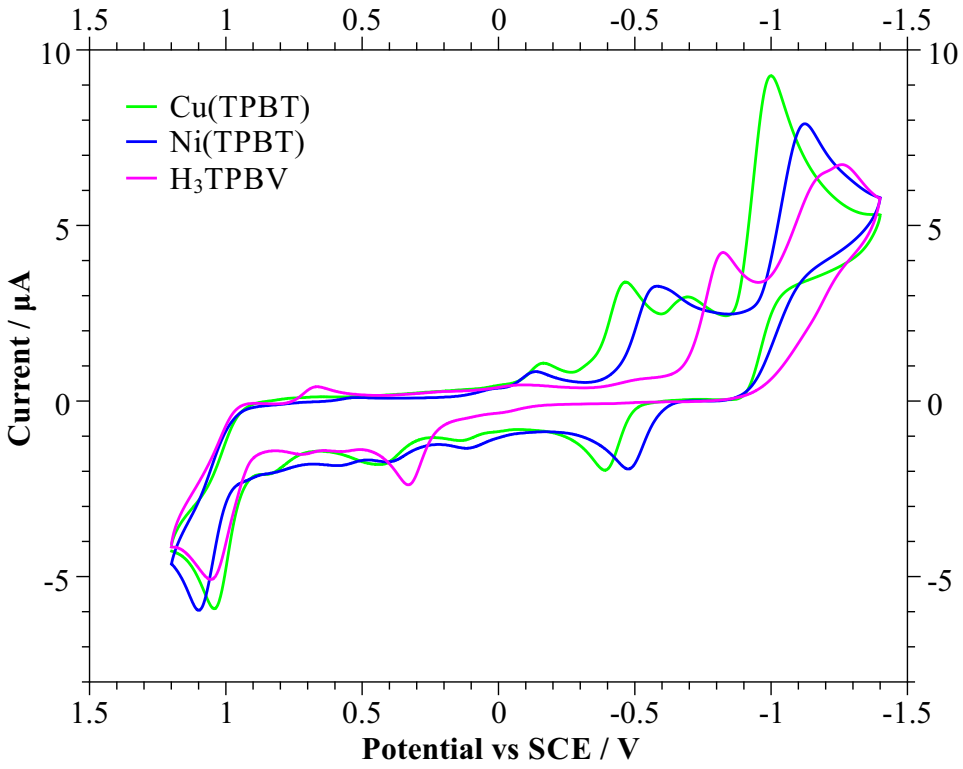

Figure 4.18: Cyclic voltammograms of Ni(TPBT), Cu(TPBT) and H_3TPBV, taken against standard calomel electrode in benzonitrile as 0.03 M solutions. 0.1 M tetrabutylammonium perchlorate was used as an electrolyte.

Here, common reversible oxidation peaks are easily found at 1.1–1.0 V, while the reversible reduction peaks scatter more widely. Similar reactions in Cu(TPBT) and Ni(TPBT) occur at –0.43 V and –0.52 V, respectively. The only striking difference between the nickel and the copper complex is an additional irreversible reaction at –0.690 V for Cu(TPBT). Overall, the results not only suggest a redox relation between TPBV and TPBT via one-electron reaction. The data also shows that in the millivolt regime, the $I(V)$ curves of the compounds is likely to be modulated by redox reactions. Considering the situation in the respective porphyrins[159,160], additional redox reactions may appear beyond ±1.5 V, likely making the $I(V)$ and SP curves considerably noisy.

4.6 Behavior on Surfaces

4.6.1 Theoretical Predictions

In order to better understand the electronic interactions of the synthesized molecules with surfaces, knowledge about their orientation is paramount. Other compounds that are well established in CISS research, such as the helicenes, have identical groups at each terminus of their helical structure. The helical tetrapyrroles introduced in this work, however, are terminated by a lactam group and either a formyl or a benzoyl group so that the interaction between molecule and surface becomes dependent on the orientation. Using the covalent hydrate of Zn(TPBT) (c.f. Figure 1.3c), Matsui *et al.* could show[79] that the bilatrienones face the gold surface with its extended π electron system parallel to the surface such that the helical axis is pointing parallel to the surface. However, the additional hydroxy group at the 15-position as well as the sp^3 hybridization of the respective carbon and the accompanying distortion of the helical geometry raise the question whether the benzoyl-on adsorption geometry found by the authors would hold true for Ni(TPBT). This question becomes all the more pressing since Carmeli *et al.* have found[5] that the CISS effect depends on the orientation of the dipole moment of substrate and adsorbate. Indeed, most recent developments in theoretical descriptions of CISS have started to appreciate this fact[28,89]. In addition, the tetrapyrroles can be expected to face the surface with their π-conjugated electronic system parallel to the surface. In doing so, the C=O bonds of either termini will not be visible in easily accessible methods such as PM-IRRAS because their vibrations become selection-rule-forbidden; hence the molecules' surface orientation becomes ambiguous unless sophisticated methods are applied.

To circumnavigate this problem, solid-state DFT calculations were applied to optimize the structures of selected molecules (in both configurations) on surfaces of Au(111) and HOPG(0001). The total energies of the resulting structures were then compared. For the starting structure, a 7×7 Au(111) surface was used with a depth of three atoms. For HOPG, a 7×7 surface with

a depth of four atoms was used and in both cases, the vacuum gap was 18 Å. The tetrapyrroles were then introduced to the xy-center of the supercell and their structure was optimized while keeping the surface fixed. For the starting structure of the TPBT complexes, a single molecule of Ni(TPBT) from its crystal structure was used. While the same approach for OEFB complexes appears equally appropriate, several studies on metal complexes of the related H_2OEP have shown[161–164] that the ethyl groups are rather flexible and prefer facing away from the surface. Hence, the starting structure of Ni(OEFB) was modified accordingly before relaxing the corresponding surfaces.

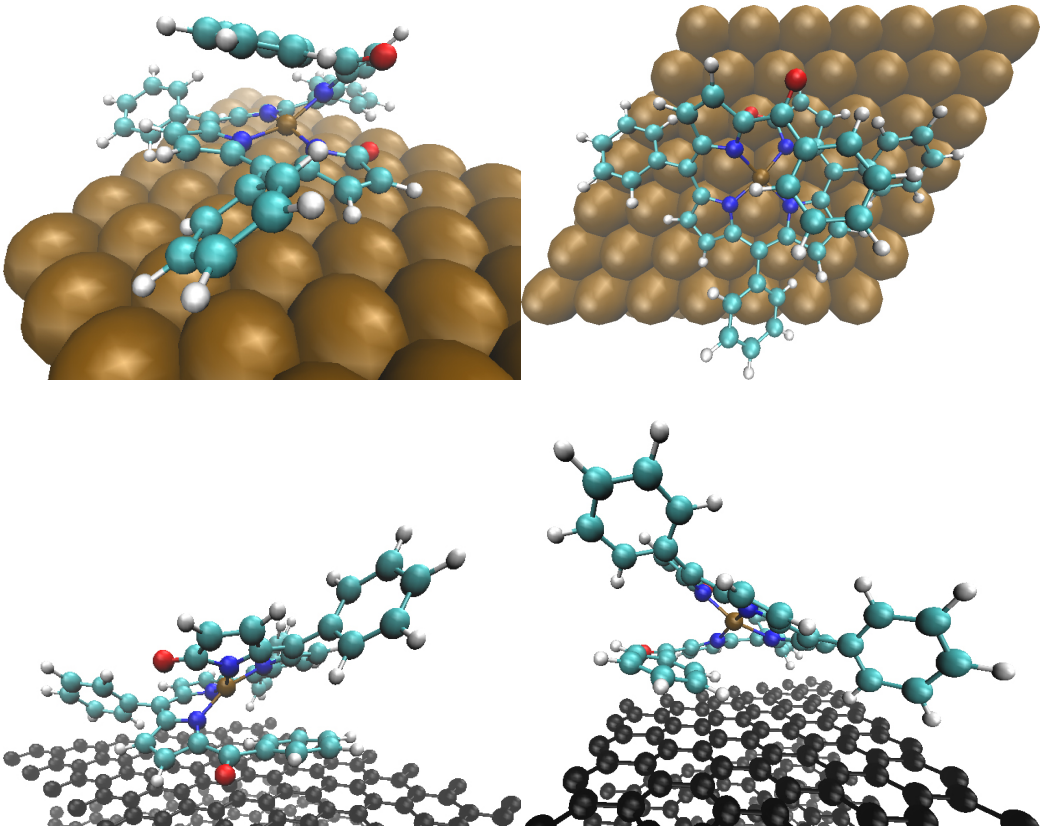

Figure 4.19: The most stable configurations of Ni(TPBT) on surfaces, predicted using DFT simulations with the PBE functional. Top row: Lactam-on configuration on a 7×7 supercell of Au(111), more stable by 69.897 kJ/mol (0.724 eV/u.c.). Bottom row: Benzoyl-on configuration on a 7×7 graphene, more stable by 82.983 kJ/mol (0.860 eV/u.c.). Note that choice of the substrate affects the adsorption geometry.

Figure 4.19 shows the optimized structures of Ni(TPBT) on Au(111) and HOPG, along with their relative energies. In the former case, the lactam-on configuration is preferred by 69.897 kJ/mol or 0.724 eV. The height of the molecule on the surface is ca. 7.56 Å or 0.8 nm. If the same molecule is deposited on HOPG, the adsorption behavior changes drastically: In fact, the opposite surface orientation is now energetically preferred so that the benzoyl-on configuration becomes more stable by 82.938 kJ/mol or 0.860 eV. Here, the height of the Ni(TPBT) molecule on the surface is approximated as 10.39 Å or 1.0 nm. Assuming the helical axis of the molecule as normal to the plane spanned by the three topmost nitrogen atoms, the tilt angle relative to the surface is ca. 20 °C on Au(111) and HOPG. The results suggest that π-π interactions are an important factor in the preferred surface orientation of these molecules.

This hypothesis is further supported by the results obtained for the octaethyl-substituted tetrapyrroles (see Figure 4.20). Here, the phenyl groups are replaced by ethyl groups in the β-pyrrole position and cannot contribute to the overall π-π interactions. As a result, the formyl-on configuration becomes energetically preferred by only 4.384 kJ/mol or 0.045 eV/u.c. for Au(111) and the lactam-on configuration becomes preferred by 4.575 kJ/mol or 0.047 eV/u.c. on HOPG.

Again, it is important to remember that most modern DFT functionals have an accuracy of 8–13 kJ/mol[152], meaning that even when assuming chemical accuracy (i.e. 4 kJ/mol[152]), enough thermal energy of the molecules may interconvert the configurations in a laboratory setting if their energy difference is sufficiently low. Moreover, the results of Chikulkuri *et al.* for Co(OEP) show[164] that the bonding to the HOPG(0001) surface is significantly weaker than on Au(111). Because of their structural similarities, a similar behavior can be expected for M(OEFB) complexes. Moreover, because the TPBT ligand in Ni(TPBT) is structurally quite similar to H_3TPBV, computational work with this molecule has not been conducted and the adsorption behavior is believed to be identical.

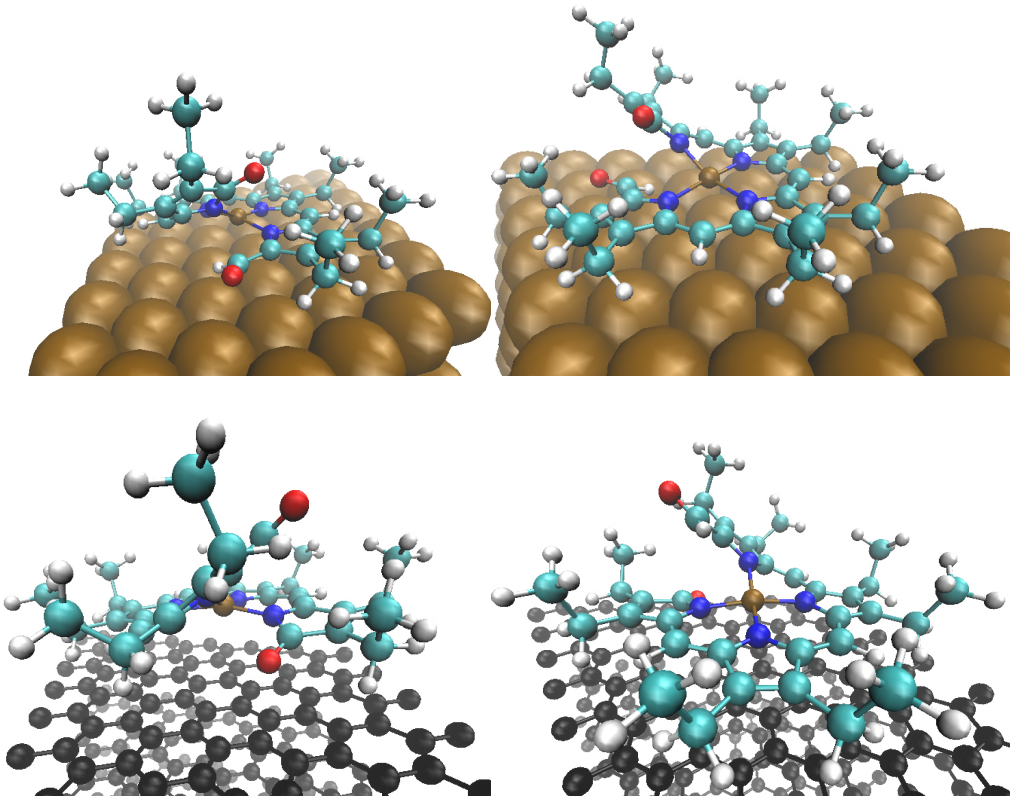

Figure 4.20: The most stable configurations of Ni(OEFB) on surfaces, predicted using DFT simulations with the PBE functional. Top row: Formyl-on configuration on a 7×7 supercell of Au(111), more stable by 4.384 kJ/mol (0.045 eV/u.c.). Bottom row: Lactam-on configuration on a 7×7 graphene supercell, more stable by 4.575 kJ/mol (0.047 eV/u.c.). Note that the adsorption geometry, compared to Ni(TPBT), has essentially become ambiguous within the limits placed by modern DFT accuracy.

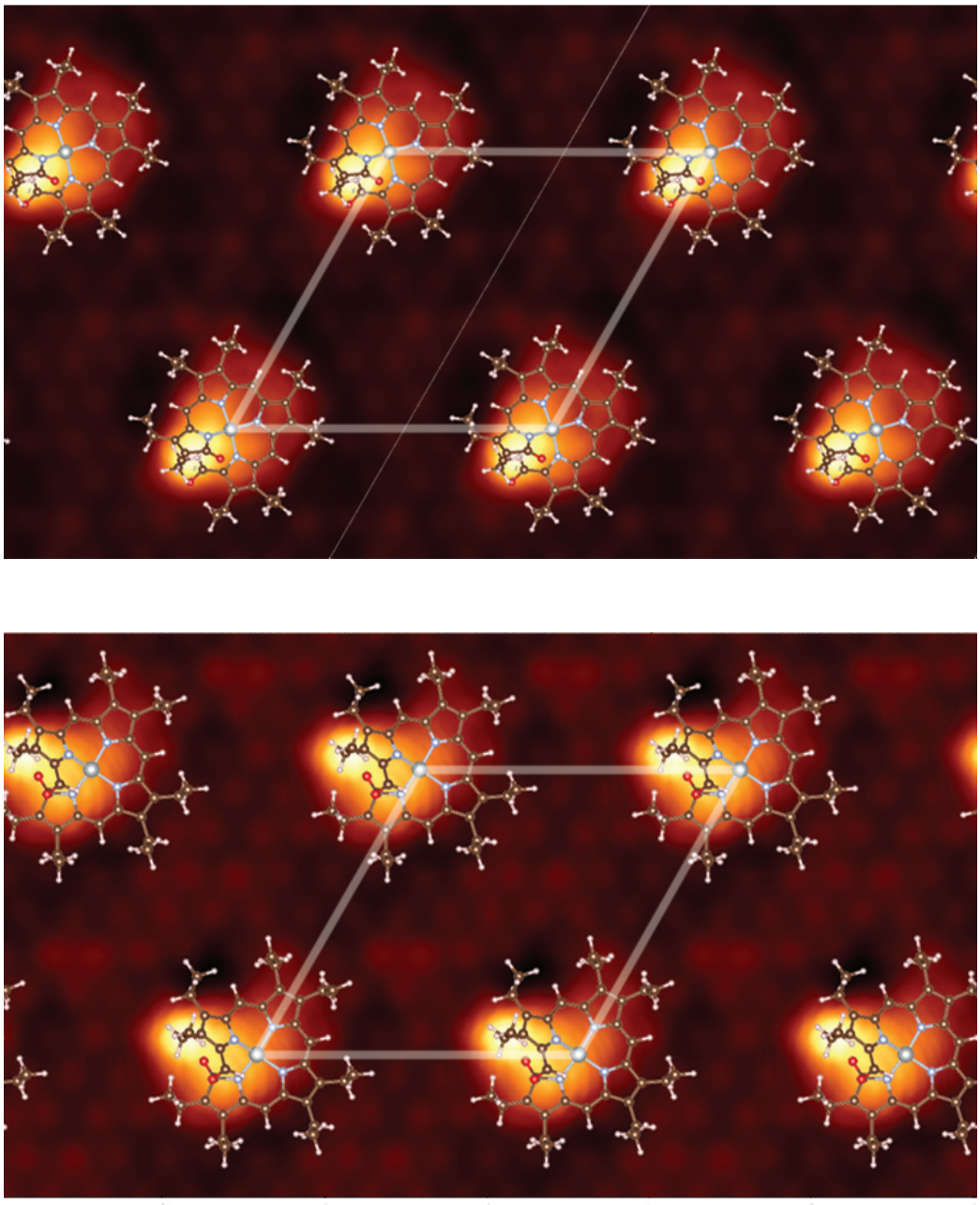

Figure 4.21: Simulated constant-height STM images of Ni(OEFB) on Au(111) at a tip bias of –1.5 V. Top: Formyl-on configuration. Bottom: Lactam-on configuration. Brighter and darker areas represent a higher and lower local density of states (LDOS), respectively. Indicated in white is the 7×7 Au(111) supercell.

In the subsequent STM simulations given in Figure 4.21, the lacking phenyl group in Ni(OEFB) makes both adsorption geometries nearly indistinguishable. This observation persists for varying tip biases (0.5 V, 1.0 V, 2.0 V and 2.5 V), whereas the different adsorption geometries of Ni(TPBT) are clearly distinguishable (Figure 4.22).
Quite the same behavior as in Ni(OEFB) can be observed upon leaving out peripheral substituents altogether, resulting in the hypothetical formylbiliverdinato nickel(II), or Ni(FB), displayed in Figure 4.23. Here, the formyl-on configuration remains energetically more stable on Au(111), again by a margin of only 5.938 kJ/mol or 0.062 eV. On HOPG, the adsorption geometries become essentially equally stable, differing in energy by only 0.425 kJ/mol or 0.004 eV/u.c.. Experimental work with this class of molecules has not been conducted.

Table 4.1: Results of the geometry optimizations for Ni(TPBT), Ni(OEFB) and Ni(FB) on Au(111) and HOPG surfaces.

Molecule	**Most stable geometry**		**ΔE / [kJ/mol]**	
	Au(111)	HOPG	Au(111)	HOPG
Ni(TPBT)	Lactam-on	Benzoyl-on	69.897	82.983
Ni(OEFB)	Formyl-on	Lactam-on	4.384	4.575
Ni(FB)	Formyl-on	Lactam-on	5.938	0.425

Obviously, these results (summarized in Table 4.1) cannot capture the complete picture of interactions between molecules, for example, in densely-packed monolayers of enantiopure or racemic substances. However, they do serve as a first approximation to be corroborated in further experiments. Moreover, the heights of the molecules on the surface and their heights in the crystal structure provide valuable starting points for evaluating AFM images. These measurements, in turn, are helpful for determining the suitable concentrations for spin-coating applications and results obtained from such experiments are discussed in the following section.

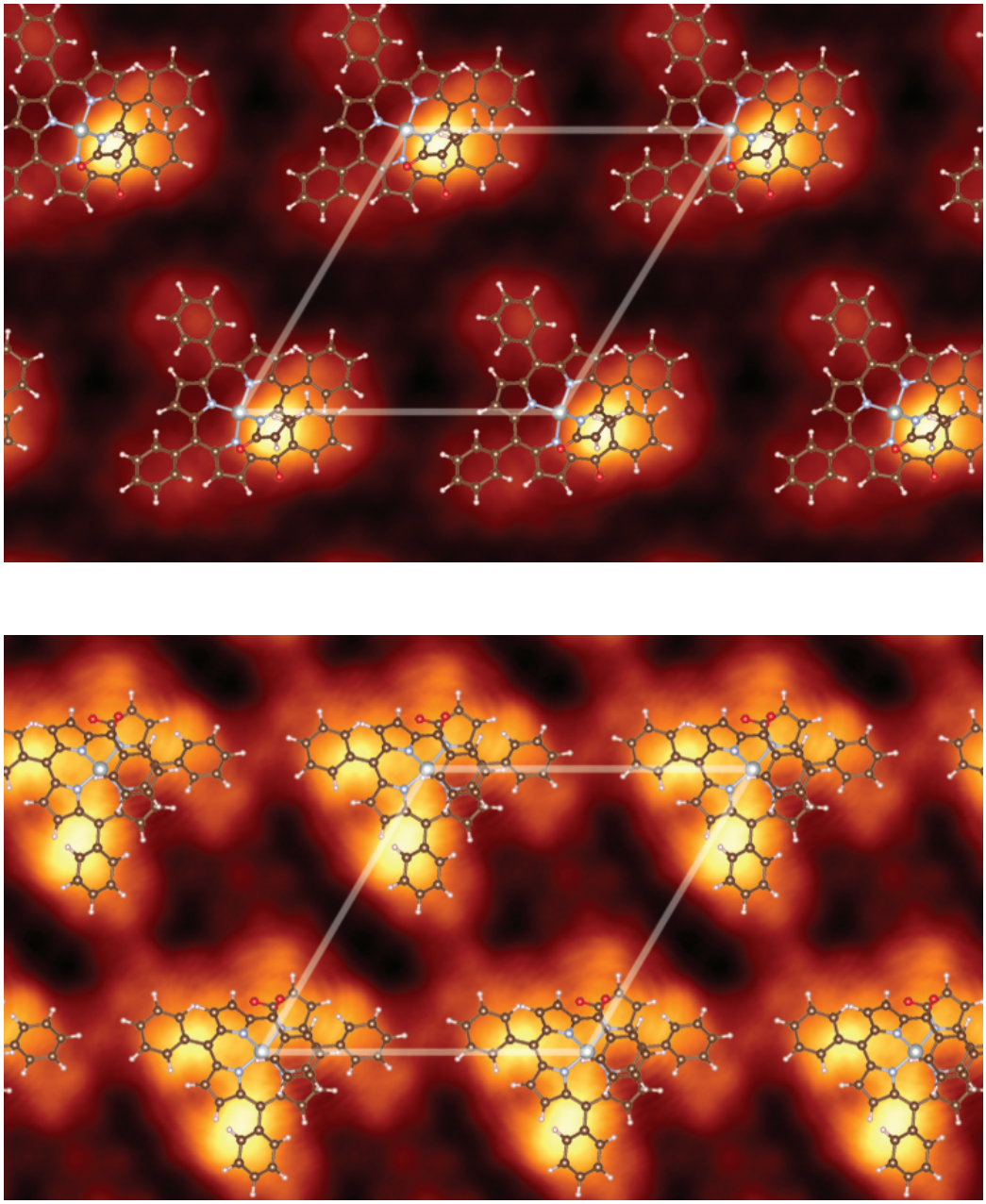

Figure 4.22: Simulated constant-height STM images of Ni(OEFB) on Au(111) at a tip bias of –1.0 V. Top: Benzoyl-on configuration, 0.44 nm above the sample. Bottom: Lactam-on configuration, 0.49 nm above the sample. Brighter and darker areas represent a higher and lower local density of states (LDOS), respectively. Indicated in white is the 7×7 Au(111) supercell.

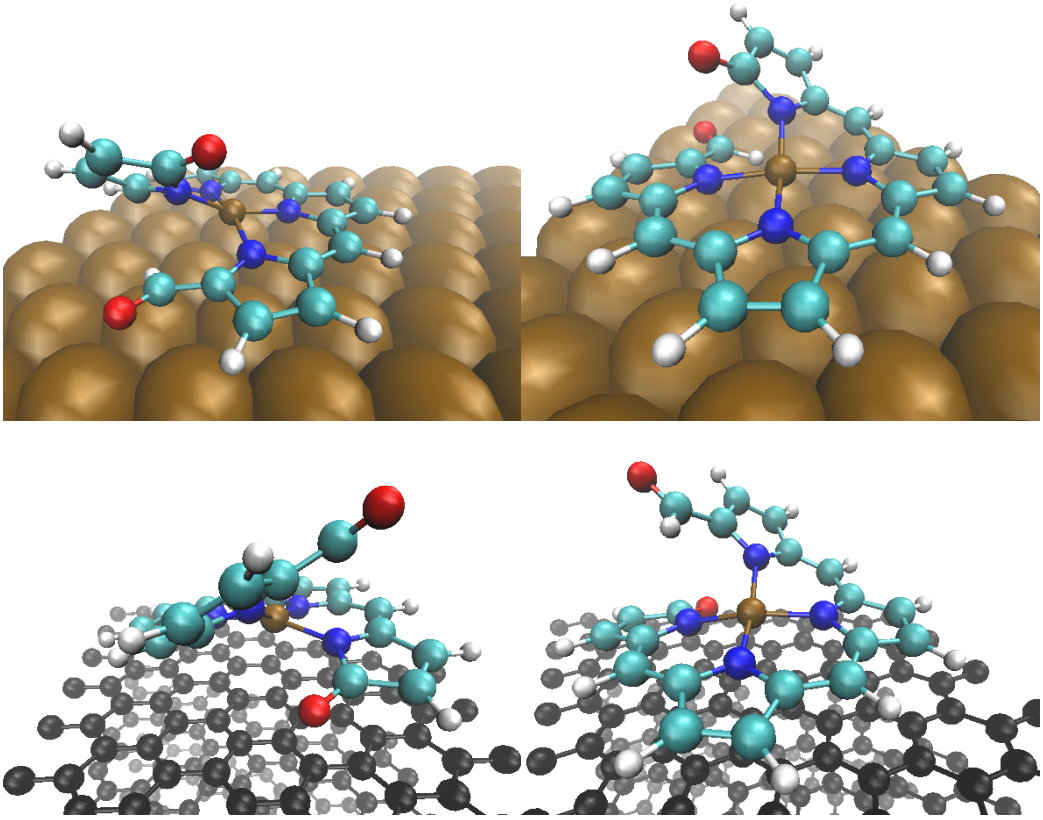

Figure 4.23: The most stable configurations of Ni(FB) on surfaces, predicted using DFT simulations with the PBE functional. Top row: Formyl-on configuration on a 7×7 supercell of Au(111), more stable by 5.938 kJ/mol (0.062 eV/u.c.). Bottom row: Lactam-on configuration on a 7×7 graphene, more stable by 0.425 kJ/mol (0.004 eV/u.c.). Note that the adsorption geometry, compared to Ni(TPBT), has essentially become ambiguous within the limits placed by modern DFT accuracy.

4.6.2 Deposition on Surfaces

As the field of molecular electronics often relies on well-defined surfaces for the manufacture of nanoscale devices, optimizing the deposition conditions of the helical tetrapyrroles is of considerable importance. In the field of single-molecule electronics in general and the study of the CISS effect in particular, obtaining smooth monolayers or sub-monolayers is typically desired. To this end, methods like molecular beam epitaxy with precisely manufactured surfaces – often from single crystals – gives the most well-defined systems but require ultrahigh vacuum conditions and highly specialized setups. Instead, spin-coating presents a suitable and easily accessible alternative in many cases. For this reason, the conditions for this manufacturing process were optimized with the goal of achieving an easily visible submonolayer. This goal is pursued so that for subsequent mc-AFM experiments measuring the CISS effect, single molecules can easily be distinguished by evaluating the surface topology or the conductivity.

For determining the optimal spin-coating concentration, surfaces of 50 nm gold on 2 cm × 2 cm Si(100) wafers were chosen, as the top gold layer easily yields a smooth Au(111) reconstruction upon annealing[165,166]. The silicon wafers were first cleaned with acetone, isopropanol and hexane, then blow-dried with dry argon and lastly cleaned with microwave-generated ozone at a power ow 10 W for 5 min. Onto the clean wafers, an adhesive layer of 5 nm titanium was deposited at 10^{-4} Pa via sputtering with nitrogen at a rate of 0.35 nm/s. Then followed a 50 nm layer of gold at a rate of 1.15 nm/s and annealing at 250 °C and 10^{-4} Pa for 18 h. Doing so significantly smoothed the surface to give polycrystalline Au(111). Figure 4.24 shows its AFM images with domain sizes of ca. 100 nm and single-atom gold steps running along a 30° to the x axis. Onto these wafers, samples of Ni(TPBT) were spin-coated with 40 µl toluene solutions at 2500 min^{-1} for 30 s. The concentrations were varied as 50, 100, 200 and 500 µM. After spin-coating, the AFM images in the Figures 4.24–4.26 were recorded.

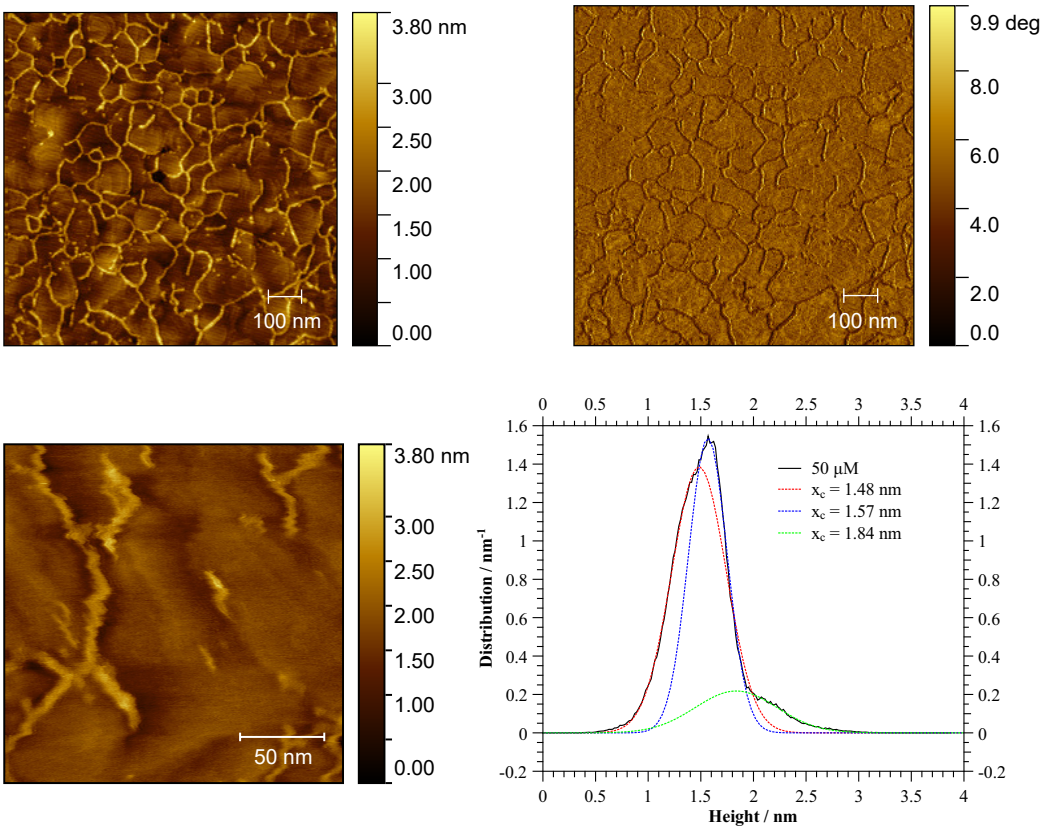

Figure 4.24: Top row: 1 µm×1 µm height (left) and phase (right) AFM images of a 50 nm gold layer on the Si(100) surface with a 5 nm titanium adhesion layer. The sample was annealed at 10^{-4} Pa and 250 °C for 18 h. The polycrystalline (111) reconstruction is easily visible with domain sizes of 100 nm and the topmost gold atoms in diagonally aligned rows. The RMS roughness of this sample was 495.9 pm. Bottom row: 200 nm×200 nm height AFM image of the Au/Ti/Si(100) surface, spincoated with 50 µM *rac*-Ni(TPBT) in toluene, next to the height histogram across the entire sampled area. Here, the RMS roughness was 295.3 pm.

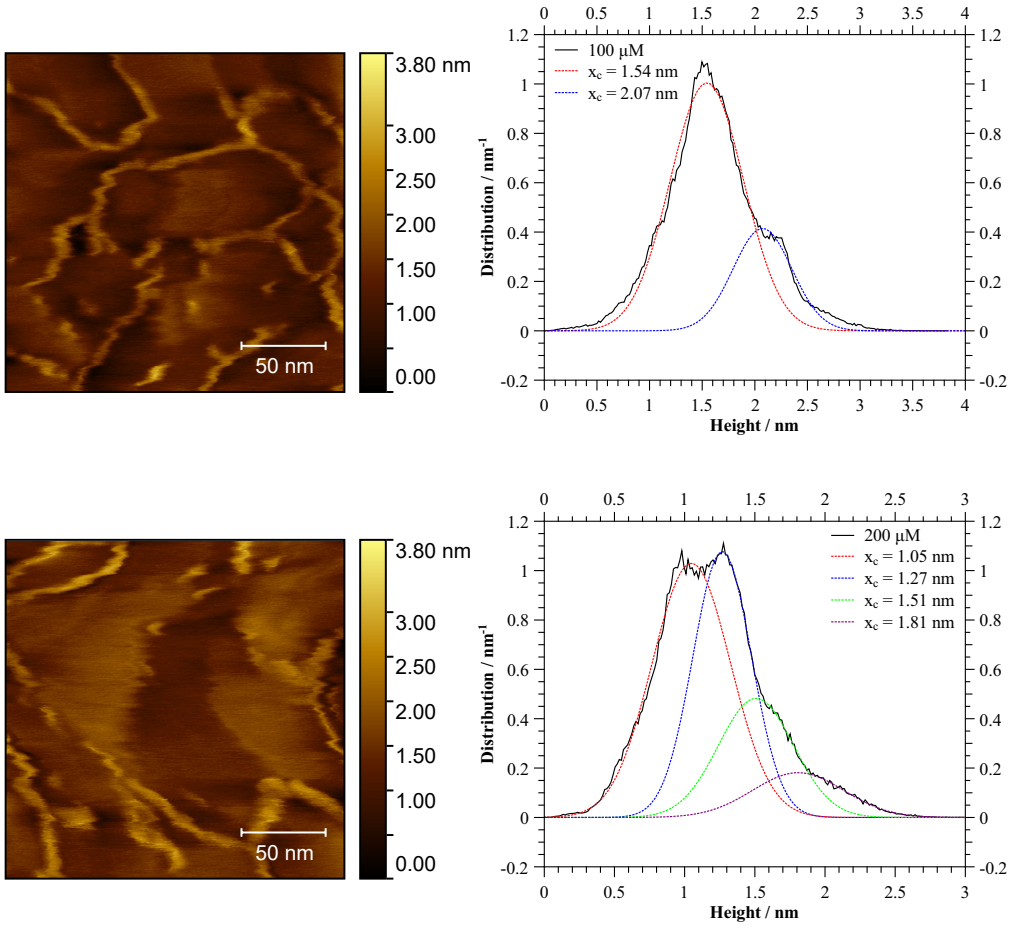

Figure 4.25: 200 nm×200 nm height AFM images of the Au/Ti/Si(100) surfaces in Figure 4.24, spincoated with various concentrations of *rac*-Ni(TPBT) in toluene, next to their height histograms across the entire sampled area. Top: 100 µM (RMS roughness 338.5 pm). Bottom: 200 µM (RMS roughness 348.8 pm).

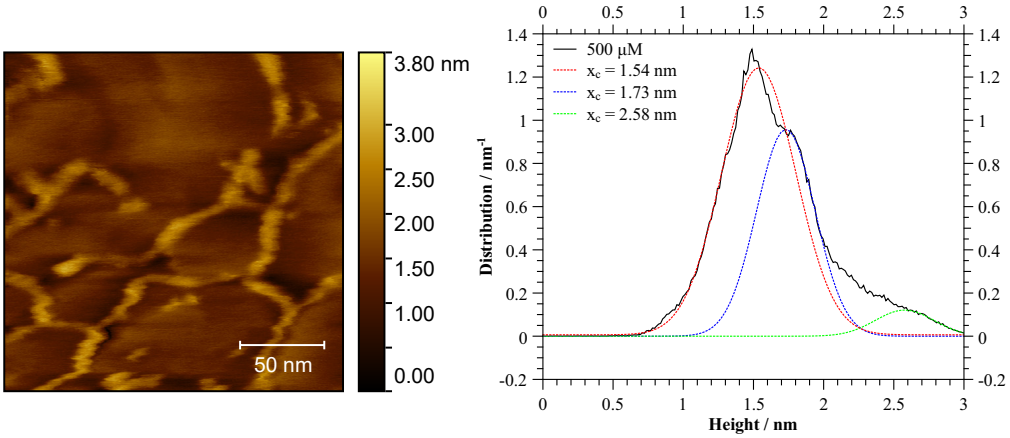

Figure 4.26: 200 nm×200 nm height AFM images of the Au/Ti/Si(100) surfaces in Figure 4.24, spincoated with *rac*-Ni(TPBT) as a 500 µM solution in toluene, next to the height histogram across the entire sampled area. Here, the RMS roughness was 350.1 pm.

While assigning the large differently-shaded areas on the height images to domains containing Ni(TPBT) may be tempting, it should be kept in mind that the same phenomenon is visible in the bare substrates shown in Figure 4.24. Hence, consulting the recorded height histograms of the respective images is arguably more appropriate for determining the optimum spin-coating concentration of Ni(TPBT): Here, fitting Gaussian peak functions through the local minima reveals contributions from the annealed gold layer for concentrations of 50 µM and 100 µM with a smaller shoulder peak arising from the terrace size observable in Au(111)[167,168]. This feature, while visible in the latter picture, could not be properly fitted. At all concentrations, another contribution at larger heights is clearly visible. The distance is ca. 0.6–0.7 nm and is within the range set by the DFT calculations (0.77 nm) and the experimentally obtained crystal structure (ca. 0.57 nm). Contributions from bilayers to the height histogram only become visible at concentrations exceeding 200 µM.

4.7 Conclusion: Expectations for observing CISS

So far in this work, four different helical tetrapyrroles were synthesized, namely Ni(TPBT), Cu(TPBT), Ni(OEFB) and H_3TPBV. The structure of the TPBT complexes showed a well-defined helix with the 20-phenyl group pointing alongside the rest of the helix to result in a total of one and a quarter turns. The discrepancy of this experimental finding with previous literature could be traced back to insufficient treatment of dispersion interaction in previous models. The synthesis of the TPBT complexes was optimized to suppress the formation of the covalent hydrate, which was shown to be an unlikely candidate for CISS studies due to the rotational freedom at one helix terminus. The variable HOMO-LUMO transitions obervable in UV/vis could be shown to originate from the tetrapyrrole helix with negligible intrahelical overlap in the frontier molecular orbitals. Moreover, these transitions not only show an unexpectedly large absorption asymmetry factor of up to 0.01, promising large spin selectivity; they also seem highly receptive towards external perturbations, including noninnocent behavior in Cu(TPBT). The separability of both helicities as well as their enantiostability is outstanding over several weeks and the AFM images suggest that very smooth mono- or bilayers are possible via spin-coating, requiring very little need for optimization.

On the other hand, the adsorption behavior of molecules without a 20-phenyl group – such as the OEFB complexes – is ambiguous which complicates the connection of experimental results with interface models of the CISS effect. In addition, cyclic voltammetry revealed a variety of redox reactions in the $\pm 1\,\mathrm{V}$ regime so that the mc-AFM measurements are likely to be accompanied by substantial noise inherent to the molecules at hand.

Table 4.2: Helical pitch h, radius r, turns n, wavelength of the HOMO-LUMO transition, its absorption asymmetry factor and the alignment of its transition magnetic dipole moment with the helical axis; collected for the three most suitable CISS study candidates in this work. † Calculated from geometry optimization of the 21,22,24H-isomer with details identical to H_2TPBT.

Molecule	h / **Å**	r / **Å**	n	λ_{max} / nm	$g_{\mathrm{Abs}}^{\mathrm{max}}$	$\theta(\vec{m}_{0,1}, \mathrm{axis})/°$
Ni(TPBT)	3.259	1.870	1.25	810	0.3×10^{-2}	19.7
Ni(OEFB)	3.187	1.953	1	802	1.0×10^{-2}	16.9
H_3TPBV	3.777†	1.987†	1	588	0.5×10^{-3}	–

The most features seemingly most important for the manifestation of the CISS effect are given in Table 4.2 for Ni(TPBT), Ni(OEFB) and H_3TPBV. Unfortunately, almost all models of the CISS effect can only provide qualitative instead of quantitative predictions. Moreover, the only quantitative models typically allow only for predictions based on extrapolation and via comparison with very simplified model structures. For example, Fransson's model of CISS as an electron correlation effect[18] predicts a spin polarization of of >6 % for all molecules in the above table if one assumes a number of $m = 24$ sites per turn an $M = 1$ turns. While the model does not allow for further quantitative assessments, it also predicts an even higher value of SP because the molecules are almost entirely sp^2-hybridized. Another model put forward by Mishra *et al.*[23] even predicts values in excess of 14 % if their values for the helical length are extrapolated accordingly. Lastly, the alignment of the first transition dipole moment with the helical axis is fairly good and less than 20° in Ni(TPBT) and Ni(OEFB), predicting a comparatively high spin polarization in the predictions of Ortuño *et al.*[157]. Similar expectations can be made when considering the comparatively high absorption asymmetry values[21–24].

The limitations of those models notwithstanding, it becomes evident that these molecules should provide a large enough spin polarization to be visible in the mc-AFM experiments in the following section, as well as allow for systematic benchmarking in the future. Thus far into this work, the following

ranking in terms of spin polarization appears reasonable, based on the g values and the helical pitch: Ni(TPBT) $\approx$ Ni(OEFB) $\gg$ H_3TPBV.

Chapter 5

Observing the CISS Effect

5.1 Sample Preparation

The method of choice for measuring the CISS effect in this work was, as mentioned previously, magnetoconductive AFM with a magnetic substrate rather than a magnetic tip. In this setup, the sample consists of nickel whose magnetization can easily be switched. In order to avoid oxidation to nickel oxide under ambient conditions, a protective layer of gold has to be deposited. However, annealing the resulting Au/Ni interface – as would be customary for surfaces deposited via RF sputtering – is not possible without risking considerable damage due to interdiffusion of these two layers at elevated temperatures[169]. Hence, it was of utmost importance that the surfaces carrying the Ni/Au system are as smooth as possible without annealing. The above-mentioned silicon wafers clearly did not meet this criterium so that the substrate was switched to common mica [muscovite, $KAl_2(AlSi_3O_{10})(F,OH)_2$]. Appropriately cut samples, 1 cm × 1 cm in size, were exfoliated three to four times with adhesive tape before a single layer was removed in the same way for further processing on the tape. The AFM images in Figure 5.1 show clearly that these mica substrates were atomically flat and retained much of their smoothness upon deposition of 120 nm nickel and 3 nm gold and that annealing of the system is not necessarily to obtain an adequately smooth

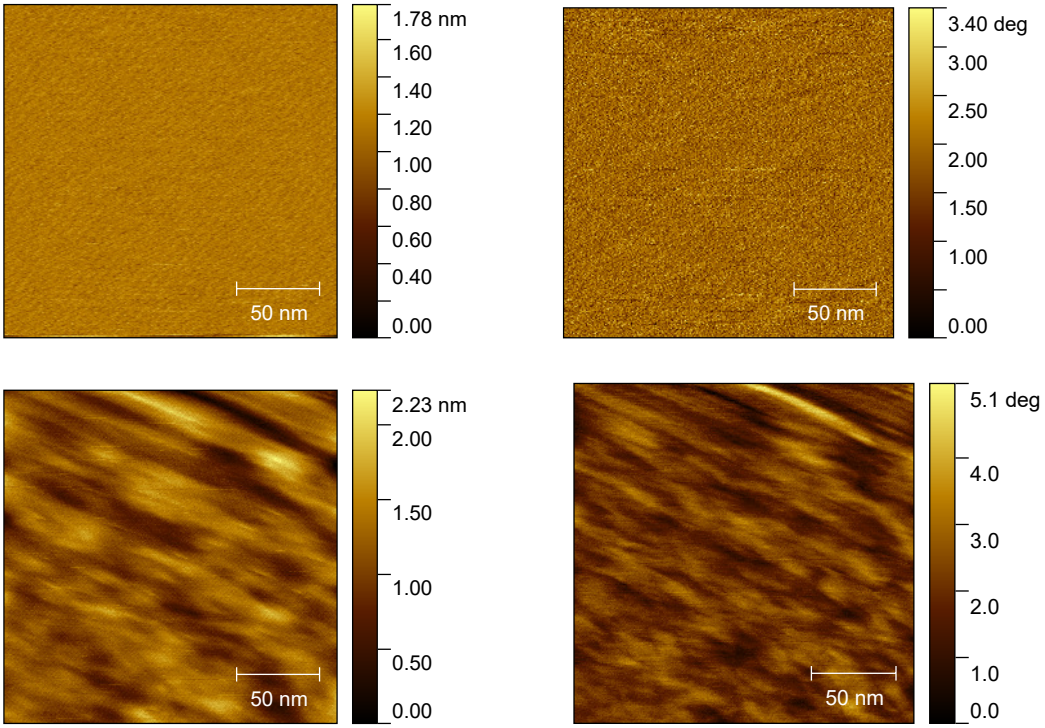

Figure 5.1: 200 nm×200 nm AFM height (left) and phase (right) images of freshly cleaved mica (top) and 3 nm Au/120 nm Ni/mica (bottom). Values of the RMS roughness were 68.39 pm and 263.9 pm, respectively.

surface. From these samples, 200 µM solutions of enantiopure Ni(TPBT) in toluene were then deposited. Their surface topology along with phase images and a horizontal line profile for y≈150 nm is given in Figure 5.1 for the deposition of (M)-Ni(TPBT). In these images, domains measuring 40–50 nm in size are easily observable. Their height, as is depicted in the line profile, is consistent with the height of monolayers and bilayers and at the chosen concentration, the monolayers are remarkably smooth with limited growth of easily distinguishable bilayers. While the rippled lines in the 200 nm images certainly seem intriguing, the data does not allow for proper assignment to two-dimensional Ni(TPBT) superstructures and may also be attributable to measurement artifacts until further investigation with scanning tunnel microscopy in future work. Nonetheless, in combination with the ones obtained for the Si/Ti/Au system in Figure 5.2, the above results

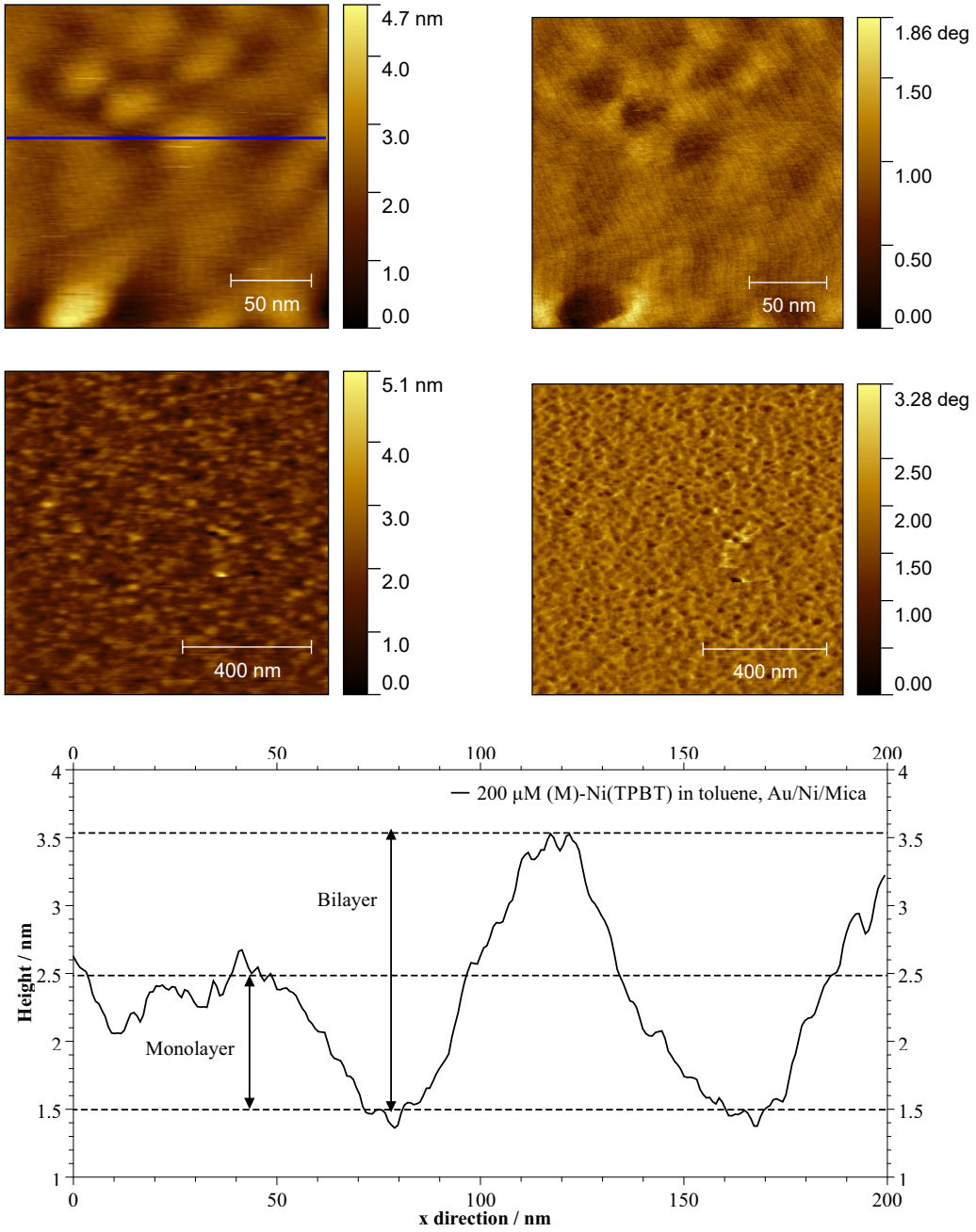

Figure 5.2: AFM height (left) and phase (right) images of 200 µM (M)-Ni(TPBT) in toluene, spincoated on the 3 nm Au/120 nm Ni/mica system. Shown are height and phase images for 200 nm×200 nm (top, RMS roughness 263.9 pm), 1 µm×1 µm (center, 445.9 pm) and a height profile of the 200 nm×200 nm picture along the blue line.

clearly show that Ni(TPBT) can form well-defined monolayers quite easily when spin-coated as a 200 µM toluene solution on a reasonably flat substrate. Even moreso, the surfaces remain remarkably flat even at much higher concentrations; an encouraging step towards the mc-AFM measurements that were conducted next.

5.2 CISS via mc-AFM Measurements

Shown in Figure 5.3 are the averaged $I(V)$ curves of the (P)-enantiomers of H_3TPBV, Ni(OEFB) and Ni(TPBT). Shaded regions of the decadic plots indicate the 95 % confidence interval CI_{95} for the average current I_{avg} such that

$$CI_{95}(I) = \left[I_{\mathrm{avg}} - \gamma \frac{\sigma}{\sqrt{n}}; I_{\mathrm{avg}} + \gamma \frac{\sigma}{\sqrt{n}} \right] \tag{5.1}$$

with the number of average curves n, their standard deviation σ and $\gamma = -1.96$ the 0.975-quantil of Student's t-distribution. Note that in this figure, the nomenclature according to Clever *et al.* (equation 3.2 on page 25) applies: At negative biases, the current flows from the sample to the tip, and from the tip to the sample at positive biases. Likewise, a negative magnetic field points from the tip to the sample, and a positive field points from the sample to the tip. Hence, the blue curve denotes an antiparallel configuration for field and electron velocity at $V < 0$ and a parallel configuration at $V > 0$. For the red curve, the notation is consequently the opposite.
As becomes apparent from the data, all (P)-isomers investigated here have a higher conductivity for the antiparallel field-velocity configuration if the current flows from the sample to the tip. As a result, the spin polarization becomes negative. Conversely, if the current flows in the other direction (at positive biases), the parallel field-velocity configuration becomes more conducting. This phenomenon in chiral molecules is the manifestation of the CISS effect and its magnitude can be determined by evaluating equation 3.2

$$SP(V) = \frac{I_{\mathrm{parallel}}(V) - I_{\mathrm{antiparallel}}}{I_{\mathrm{parallel}}(V) + I_{\mathrm{antiparallel}}(V)} \cdot 100\ \%.$$

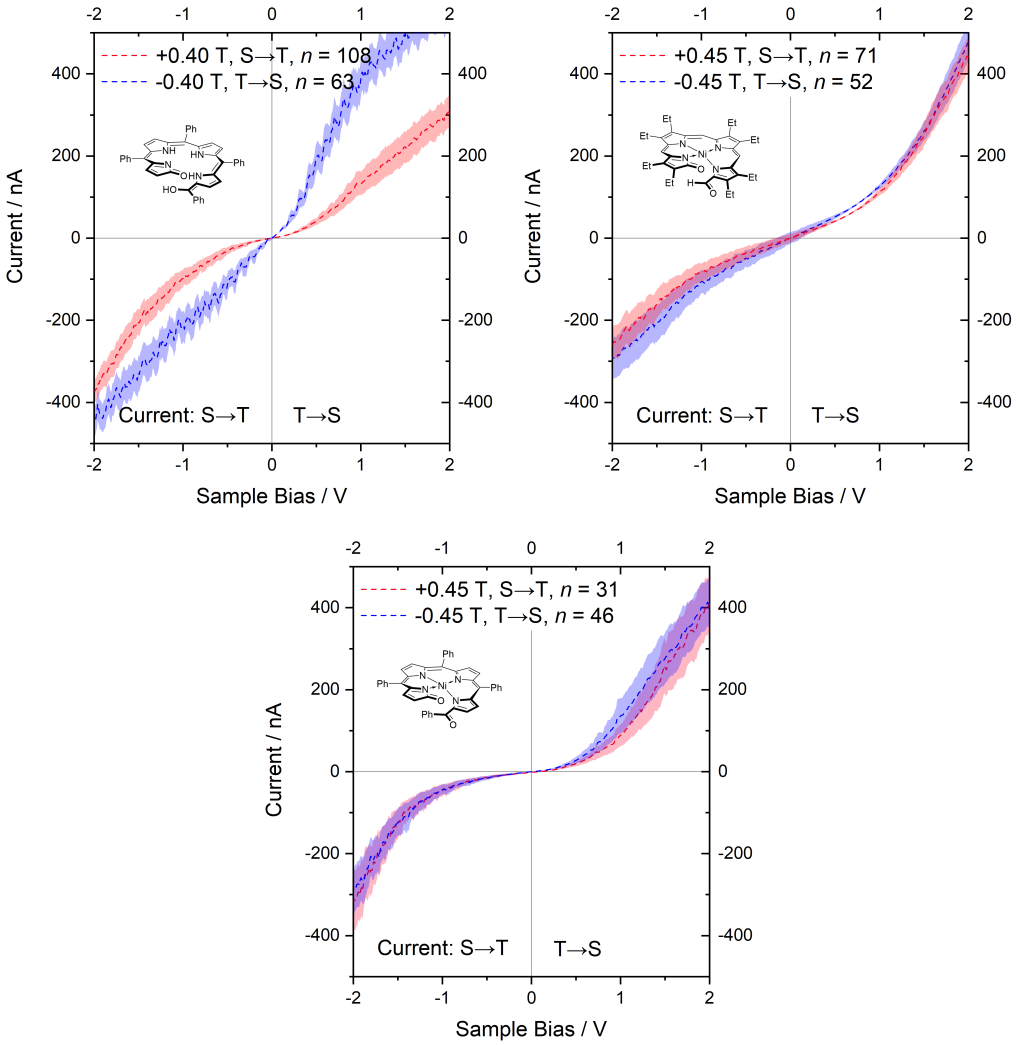

Figure 5.3: Averaged $I(V)$ curves obtained from magnetoconductive AFM measurements of the (P)-enantiomers of three helical tetrapyrroles, spin-coated on 3 nm Au/120 nm Ni/Mica from 200 µM solutions in toluene. Measurements were evaluated for scanning from negative to positive bias and feature the 95 % confidence interval as shaded areas for n individual curves. Top left: H_3TPBV. Top right: Ni(OEFB). Bottom: Ni(TPBT).

In doing so, the plots in Figure 5.4 are obtained. The large mean deviations in some parts of the SP plots can be sufficiently explained by recalling that in those areas, the molecules show oxidation/reduction in cyclic voltammetry[70]. As these processes have previously been shown to be single-electron processes, it appears likely that the resulting tetrapyrrole species are interfering with the measurement setup at least to some extent. In the light of this behavior, the spin polarization of up to 25–30 % in H_3TPBV is especially surprising. In some cases, values in excess of 40 % could be observed. However, these are omitted in this work due to their lacking reproducibility. Recalling the phenomenological description of chirality-induced spin selectivity in Chapter 1, opposite spin polarization can be expected in the opposite helicities, i.e. the (M)-enantiomers. These measurements are planned in the near future, together with developing a CISS measurement method that is not overly reliant on electron transfer. Until such a method is developed by either the author of this work or the research community as a whole, Mott scattering experiments can serve as a more elaborate substitute, as the next section provides.

5.3 Collaborative Projects

In an attempt to expand the potential scope of applications of helical tetrapyrroles towards more sophisticated molecular electronics setups requiring ultrahigh vacuum conditions, the below projects were pursued together with Paul Möllers of the Zacharias group at the University of Münster, Germany. Written and oral consent has been received prior to submission of this thesis.

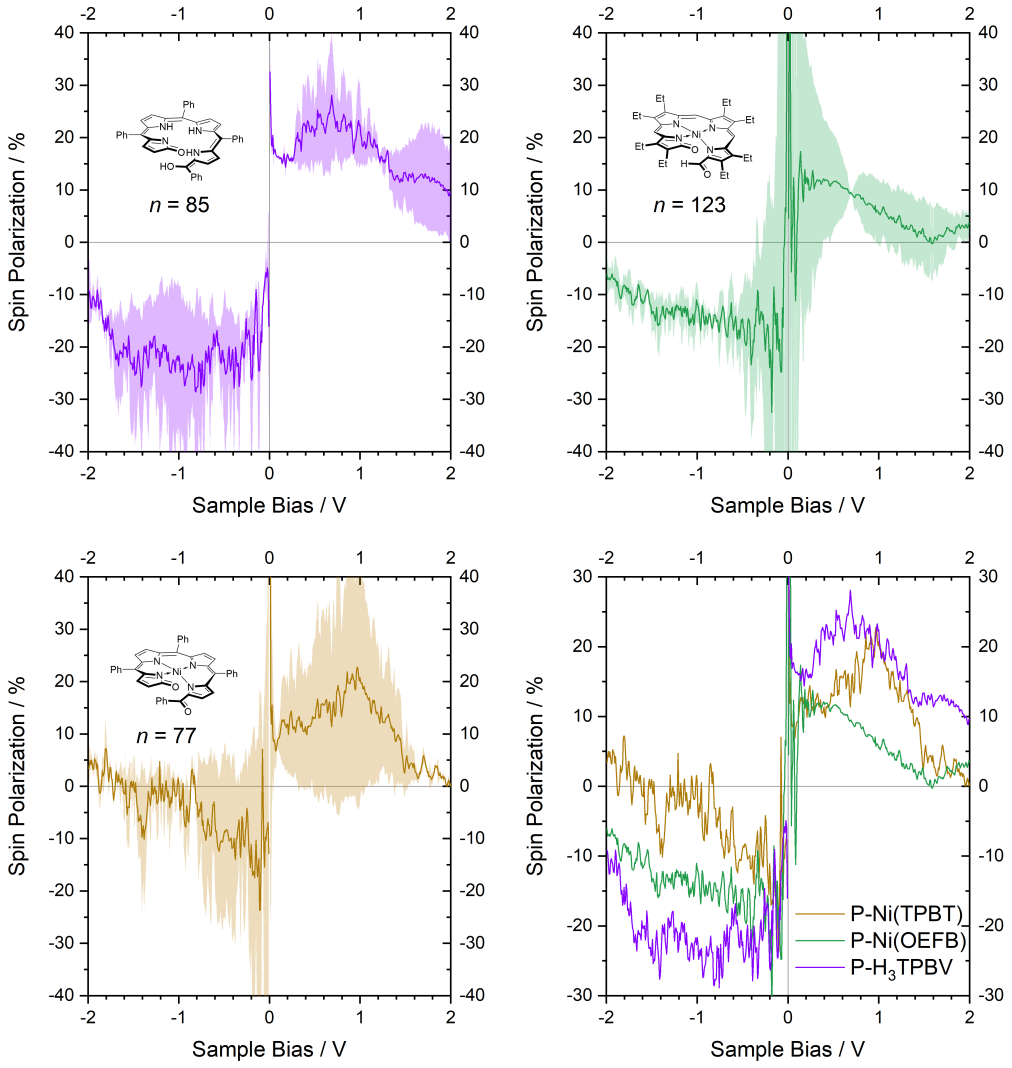

Figure 5.4: Spin polarization curves obtained from magnetoconductive AFM measurements of the (P)-enantiomers of three helical tetrapyrroles, spin-coated on 3 nm Au/120 nm Ni/Mica from 200 µM solutions in toluene. Measurements were evaluated for scanning from negative to positive bias and feature the mean deviation as shaded areas for n individual curves. Top left: H_3TPBV. Top right: Ni(OEFB). Bottom left: Ni(TPBT). Bottom right: Cumulative plot.

5.3.1 Monolayer Formation under Ultrahigh Vacuum

Arguably, one of the key advantages of UHV conditions is the high control over the environment of the sample. For example, the lowered presence of gases such as oxygen, CO_2, trace H_2S, or ambient moisture allows for experiments with surfaces that are chemically reactive by forming adsorbate structures. Moreover, one can derive from the kinetic theory of gases states and the ideal gas law that the mean free path λ of a particle increases with decreasing pressure p according to the equation

$$\lambda = \frac{k_B T}{\sigma p} \tag{5.2}$$

where k_B is Boltzmann's constant, T is the temperature and σ the effective cross-sectional area of the spherical particle under consideration[170]. This idea becomes intuitive if one considers that at a lower pressure, less other particles are present which can act as elastic or inelastic scatterers. This becomes especially important in CISS-related experiments that depend on free-electron beams such as the Mott polarimetry introduced in Chapter 5.3.2 on page 80. To this end, it is advantageous to form a well-defined and smooth monolayer on a substrate that is as close to idealized conditions as possible, as this allows for determining the amount of spin-polarization per molecular layer and by extension, the amount of "CISS per molecule".

In order to form such a monolayer, Paul Möllers and the author chose to first heat a Knudsen cell with racemic Cu(TPBT) in a UHV chamber[1] ($p < 5\times10^{-9}$ mbar) while evaluating the signal of an attached quadrupol mass spectrometer at m/z = 104 and 105 (from loss of a benzoyl fragment). Once the optimal temperature had been determined as 170 °C as a compromise of evaporation speed and thermal stability, the Cu(TPBT) was deposited onto a freshly Ar^+-sputtered Cu(111) crystal that was held at room temperature, and the sample was heated to various temperatures for 20 min to allow for thermodesorption (TDS) of the molecules. The resulting surface was then

[1] The inside of the chamber was coated with mu-metal for shielding from external magnetic fields and the entire setup was surrounded by three Helmholtz coils in order to compensate the earth's magnetic field.

probed with photons in the vacuum ultraviolet regime to excite electrons at different binding energies out of the sample and into a detector (ultraviolet photoelectron spectroscopy or UPS). The photons had an energy of 10.5 eV or a wavelength of 118 nm (generated by tripling the third harmonic of a Nd:YVO_4 laser) and were directed onto the sample at a 60° angle such that the respective electrical field vector exhibited components both parallel and perpendicular to the surface to excite the surface state. After the acquisition of the UPS spectra, the heating of the sample and subsequent UPS experiments were repeated at a higher temperature. The resulting spectra are given in Figure 5.5 where the spectrum of the clean Cu(111) crystal is shaded in grey. In the figure, one can clearly see that upon deposition of the Cu(TPBT)

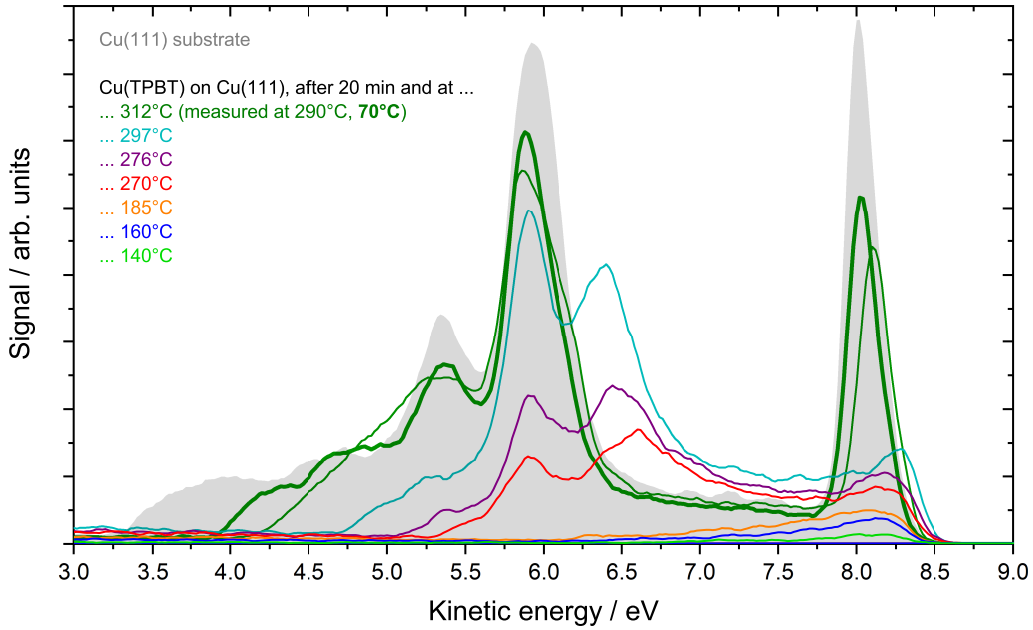

Figure 5.5: UPS results for TDS experiments with rac-Cu(TPBT) on Cu(111) at various temperatures. All data was smoothed with a ten-point Savitzky-Golay filter. Data provided by Paul Möllers.

molecules, all states of the Cu(111) crystal are suppressed, indicating the formation of a thick multilayer. As the sample is heated to 297–312 °C, the initial surface state at 8 eV of the bare substrate is recovered, along with an additional state at $E_{\mathrm{kin}} = 6.5$ eV which is currently being ascribed to a

Cu(TPBT) monolayer[171]. This state is not visible at elevated temperatures so that the bare substrate is fully recovered. However, it is currently not clear whether the desorption of the molecule is accompanied by decomposition or whether it is decomposition-free. In any case, the results clearly show that the TPBT complexes in this work are suitable for experiments under UHV conditions and the easy evaporation and thermodesorption are encouraging for further studies – such as in the Mott polarimetry experiments that followed. Here, the the samples were first evaporated at a surface temperature of 240 °C and a crucible temperature of 170 °C.

5.3.2 CISS in Ni(TPBT) via Mott Polarimetry

Mott polarimetry, contrary to magnetoconductive AFM relies on CISS as an electron transmission, rather than an electron transport phenomenon. Here, photoelectrons are generated by irradiation with an ultraviolet laser pulse. After weakly relativistic scattering, these electrons take different trajectories based on their spin so that they can be registered using two separate detectors. If a molecule is CISS-active, the registered signal at both will reveal an asymmetry A in the count rates N according to

$$A = \frac{N_u - N_l}{N_u + N_l} \cdot 100\%, \text{ where } SP = \frac{N_\uparrow - N_\downarrow}{N_\uparrow + N_\downarrow} = \frac{A}{S_{\text{eff}}(\theta)} \tag{5.3}$$

and where $N_{u,l}$ denote the count rates at the detectors in Figure 5.6 and $N_{\uparrow,\downarrow}$ denote the numbers of spin-up and spin-down electrons. $S_{\text{eff}} \in [-1; 1]$ is the effective Sherman function[172], a device-dependent entity that describes the probability of a spin-up electron to be scattered at an angle θ from the target, or the analyzing power of the polarimeter. If $S_{\text{eff}}(\theta) = -1$, such an electron is with 100 % probability scattered to the upper detector at θ, whereas it is exclusively scattered to the lower if $S_{\text{eff}}(\theta) = +1$. Similarly, the probabilities for either side are equal if $S_{\text{eff}}(\theta) = 0$. In this work, the setup was identical to previous work of the Zacharias group[6,35,173–175].

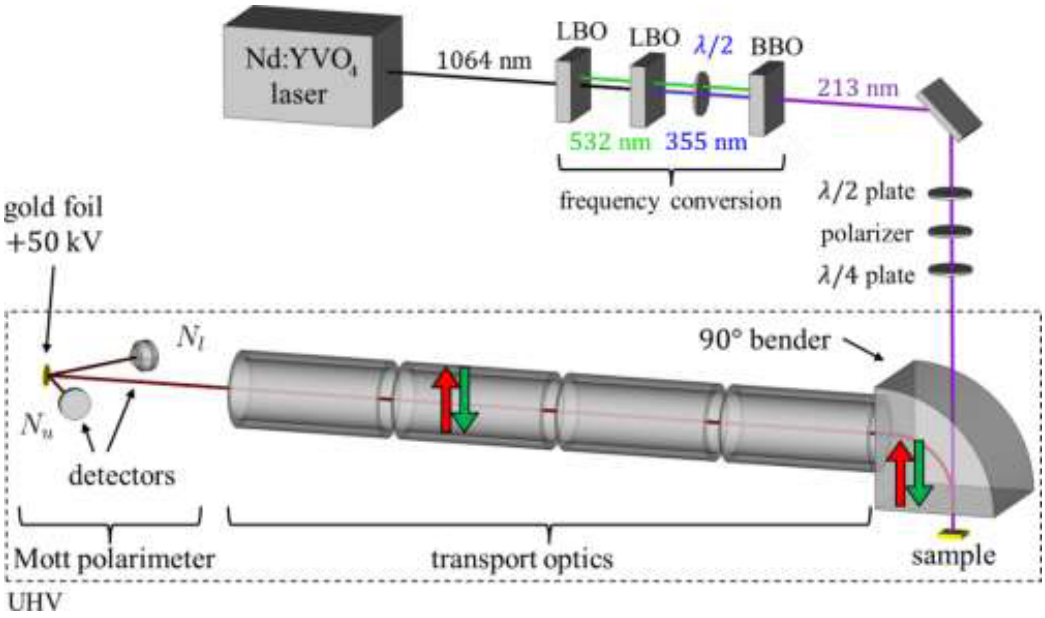

Figure 5.6: Setup for the Mott scattering experiments[35]. LBO: Lithium borate LiB_3O_5. BBO: β-Barium borate $Ba(BO_2)_2$. Reprinted with permission from Ghosh *et al.* Copyright 2019 American Chemical Society.

The laser pulse, generated as the fifth harmonic from the same Nd:YVO_4 laser in Chapter 5.3.1, had a wavelength of 213 nm (5.83 eV) with a duration of ca. 200 ps and a repetition rate of 20 kHz. The photoelectrons of up to ≈1 eV leaving the sample – enantiopure Ni(TPBT) on Cu(111) – were then collected orthogonal to the surface and bent electrostatically onto a 90° trajectory to convert a longitudinal to a transversal spin polarization. Accelerated to 50 keV, the photoelectrons are then directed onto a gold foil and scattered towards two semiconductor detectors placed at ±120° relative to the incident electron beam. Each experimental run consisted of ca. 10^6 laser pulses with polycrystalline gold as a reference. The setup was kept under the same conditions as the one in Chapter 5.3.1 and is shown schematically in Figure 5.6.

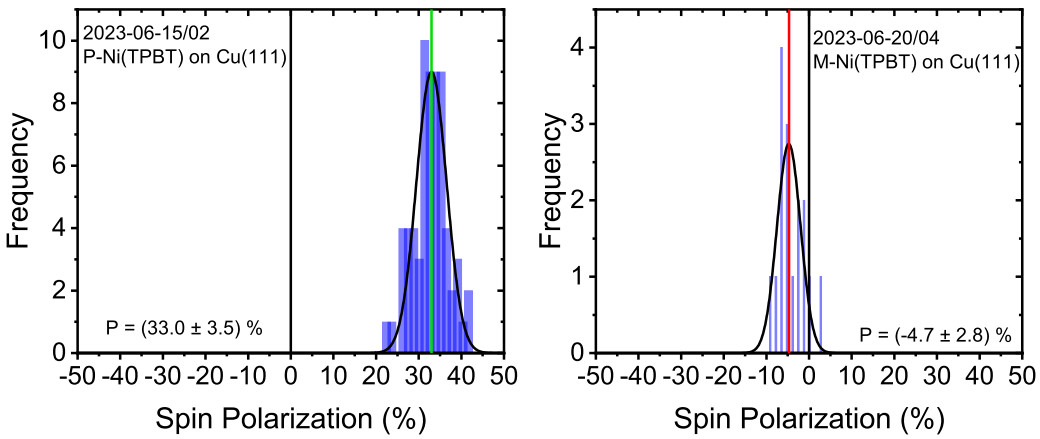

Figure 5.7: Histograms showing the spin polarization of enantiopure Ni(TPBT) on the Cu(111) surface during Mott polarimetry. Left: P-enantiomer. Right: M-enantiomer. Data provided by Paul Möllers.

Figure 5.7 shows the results obtained thus far with this setup. At up to 33.0±3.5 %, the maximum spin polarization lies between helicene[2] with 6–8 % and double-stranded DNA[6] of 78 base pairs with up to 60 %. The lower value for the M-isomer is likely due to the low amount of sample left during the evaporation[171] as on some spots on the sample, no polarization was observable. Another sample has been sent to Mr. Möllers shortly before submission of this work. The cooperation is currently ongoing and future plans include the measurement of enantiopure Ni(OEFB) and H_3TPBV. Overall, these preliminary results are highly encouraging, especially considering that Ni(TPBT) showed only an intermediate spin polarization in the mc-AFM experiments; it is thus believed by the author that even higher values may be observable for H_3TPBV.

5.4 Conclusion

In this section, the chirality-induced spin selectivity effect could be observed in monolayers of the three helical tetrapyrroles Ni(TPBT), Ni(OEFB) and H_3TPBV. The spin polarization in mc-AFM experiments reached values as high as 25–30 % in H_3TPBV, much higher than quantitative models of the effect currently suggest. The magnitude of the CISS effect follows the trend

Table 5.1: Selected molecular properties of H_3TPBV, Ni(TPBT) and Ni(OEFB), along with their maximum spin polarization observed in mc-AFM experiments: Helical pitch h, partial charge $\overline{q}_{\text{helix}}$, dipole moment $\vec{p}$ and magnitude of the first transition dipole moment $|\vec{m}_{0,1}|$. All obtained via Löwdin population analysis with the ωB97X functional and the def2-TZVP basis set, with augmentations as in Chapter 3.4.1. $|\vec{m}_{0,1}|$ was obtained from the ECD simulations given in Chapter 4.4.

Molecule	h / **Å**	$\overline{q}_{\text{helix}}$	$\vec{p}$ / **D**	$\lvert\vec{m}_{0,1}\rvert$ / **a.u.**	SP_{max} / %
H_3TPBV	3.777	–0.029	4.4497	–	28
Ni(TPBT)	3.259	+0.022	5.7398	1.2681	20
Ni(OEFB)	3.187 [70]	–0.057	6.0895	1.4902	18

H_3TPBV > Ni(TPBT) > Ni(OEFB), meaning that the spin polarization seemingly decreases with the molecule's absorption asymmetry factor $g_{\text{abs}}^{\text{max}}$ of the lowest-energy ECD-active transition – a finding contrary to prevailing literature.

Moreover, the magnitude of the effect does not seem to follow a particular trend regarding the number of turns in the helix or any of the other molecular properties pictured in Table 5.1 and Figure 5.8. However, it does seem to depend on the helical pitch, with the caveat being that the values for H_3TPBV are calculated[2] and not based on an experimental crystal structure.

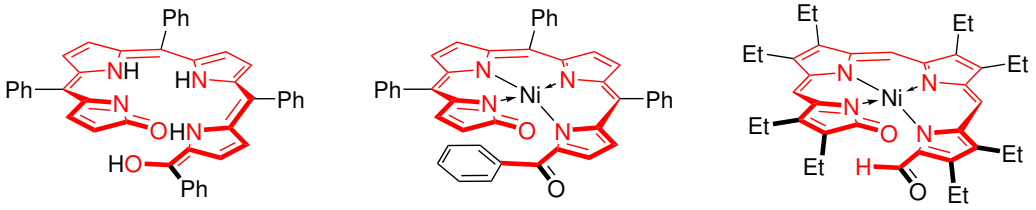

Figure 5.8: Charge densities of the atoms evaluated in Ni(TPBT), Ni(OEFB) and H_3TPBV for the population analysis, depicted in red.

[2] 21,22,24*H*-isomer, ωB97X functional with def2-TZVP basis set, augmentations as in the PES scans of H_2TPBT. Based on the distances between lactam-O and C19, C20 and C2, and enoyl-O and C4.

Despite the currently unclear behavior of the spin polarization in these molecules, their overall large magnitudes are quite encouraging for future experiments. Additionally, the fact that all synthetic protocols devised in this work scale up to at least the triple-digit milligram regime with comparatively simple chemicals should make these molecules accessible to a broad variety of disciplines and applications.

Returning to the original theme of this work – the versatility and the potential for benchmarking CISS –, the spin polarization should be high enough to be detectable in a variety of setups, and with a variety of modifications of the tetrapyrrole helix. Hence, this work will close with a brief literature review, focusing of possible modifications that previous research has shown to be facile.

Chapter 6

Outlook

6.1 Modifiable Variables

Clearly, the results shown in Chapter 5.2 were quite surprising in the magnitude of the CISS effect, especially considering that structurally similar molecules such as the helicenes[2] only show a spin polarization of 6–8 %, a discrepancy of up to 450 %. This begs the question: *Why does an organic molecule filter up to a third of electron spins at room temperature?* While, as pointed out earlier, no comprehensive theoretical model of the CISS effect exists to date, several starting points for a more systematic study are possible from a purely molecular perspective. These, along with the feasability of such studies, are given below based on a short literature review.

For a more thorough review of the syntheses of oligopyrroles, Falk's book "The Chemistry of Linear Oligopyrroles and Bile Pigments" may be consulted[147]. However, it should be noted that many of his own syntheses that Falk cites here are either lost with time (see Chapter 6.1.2) or lost in translation, as most of his publications were in German without an English translation beyond the abstract. To mitigate the latter aspect, the author of this thesis offers to provide translation of articles to the committee upon prior notice.

6.1.1 Helical Pitch and Radius

One of the first ideas that comes to mind when one thinks of a helix – the underlying structural motif of Ni(TPBT) – are the pitch and the radius. Luckily, the work group of Alan Balch published a wide variety of different crystal structures of bilindione and biliverdin complexes which – together with the crystal structure obtained in this work – provide a large enough sample size for systematic comparison.

From Table 6.1, it becomes clear that the radius of the tetrapyrrole helix, regardless of metal, substitution pattern, or coordination pattern, is essentially fixed at 1.973 Å ± 0.044 Å. Similarly, the pitch of the molecular helix is surprisingly consistent (3.106 Å ± 0.083 Å) even in the presence of bulky terminal substituents like phenyl groups. Moreover, even drastically different coordination patterns, such as the formation of dimers or the coordination with Pd_2^{2+} do not seem to affect the geometry. The geometrical properties of H_3TPBV, obtained from the same computational setup as the geometry optimization of H_2TPBT, are included only for completeness' sake and should be taken with care until an experimental crystal structure is obtained.

On the other hand, the HOMO-LUMO transitions (which in this work have previously been established to be ECD active and thus related to the CISS effect) and their strengths in UV/vis vary to a large degree, even when heavier central atoms like palladium or a lack of thereof are not considered. Moreover, these transitions show a strong dependence on the solvent. This can be explained by the axial coordination of a pyridine molecule to the central metal atom of the complex, as evident by the crystal structure. Whether this affects the absorption asymmetry factor g_{Abs} cannot be decided: The Balch group who published these results never attempted enantioseparation[176], probably because literature[74,75,177] provides strong evidence that their separation with chiral HPLC might not be possible due to quick racemization of similar molecules at room temperature.

Table 6.1: Structural parameters (radius r and pitch h) of various tetrapyrrole complexes, along with their lowest-energy transition in UV/vis spectra (in $CHCl_3$ unless otherwise stated) and its respective absorption anisotropy factor $g_{\mathrm{Abs}}^{\mathrm{max}}$. Pitches are based on the oxygen-oxygen distances in OEB complexes, and based on the distance between the formyl-carbon and the lactam-oxygen in OEFB complexes. Values for ε are in units of $[10^4\,\mathrm{l\,mol^{-1}\,cm^{-1}}]$ and $g_{\mathrm{Abs}}^{\mathrm{max}}$ in units of 10^{-2}.[a] Taken in pyridine. [b] Taken in CH_2Cl_2. [c] Taken in methanol. [d] Taken in IPA/$CHCl_3$ 2:1. [e] Taken in EtOAc/hexane 1:1. [f] Taken in IPA/$CHCl_3$ 1:2. [g] Calculated from geometry optimization of the 21,22,24*H*-isomer with details identical to H_2TPBT.

Structure	r / Å	h / Å	λ_{max} / nm	$\varepsilon(\lambda_{\mathrm{max}})$	$g_{\mathrm{Abs}}^{\mathrm{max}}$
H_3OEB[178]	—	—	648[c]	1.6[c]	—
{Mn(OEB)}$_2$[67]	1.981	3.186	880	2.9	—
{Mn(OEB)}$_2$[67]	1.981	3.186	906[a]	1.2[a]	—
Mn(OEB)[67]	1.965	3.143	—	—	—
{Fe(OEB)}$_2$[66]	2.094	3.095	643	1.6	—
{Fe(OEB)}$_2$[66]	—	—	636[a]	1.0[a]	—
Co(OEB)[67]	1.891	3.116	642	1.9	—
			909[a]	0.7[a]	—
Cu(OEB)[179]	1.957	3.154	646	3.1	—
{Pd(OEB)}$_2$[154]	2.039	2.945	788	1.4	—
Pd$_4$(OEB)$_2$[72]	2.039	2.945	831	2.2	—
Co(OEFB)[70]	1.953	3.187	766	0.5	—
Ni(OEFB)[70]	1.953	3.187	802	0.9	1.0[d]
Cu(OEFB)[70]	1.953	3.187	844	1.0	—
Ni(TPBT)	1.870	3.259	810[b]	1.1[b]	0.3[e]
Cu(TPBT)	—	—	857[b]	1.8[b]	—
H_3TPBV	1.987[g]	3.777[g]	588[87]	2.2[87]	0.05[f,g]

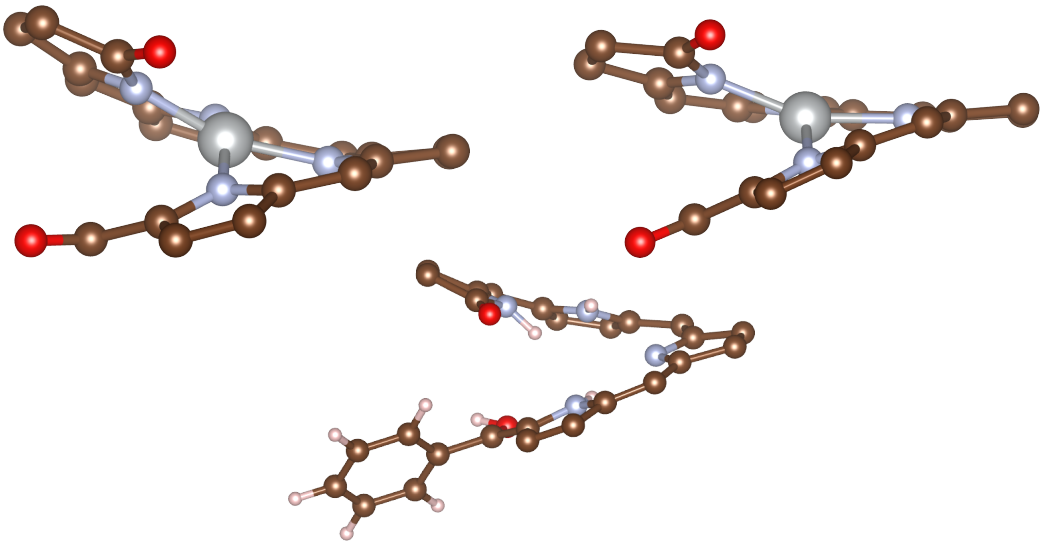

Figure 6.1: Side view of the tetrapyrrole helix in the crystal structures of Ni(TPBT) on the top left and Ni(OEFB) on the top right. The bottom strcuture of H_3TPBV was obtained from geometry optimization of the 21,22,24*H*-isomer using the ωB97X with the def2-TZVP basis set and augmentations as for H_2TPBT. Peripheral substituents have been omitted for clarity.

Despite the helical radius and pitch being consistent across the tetrapyrrole molecules in literature, larger crowding may be possible if respective phenyl groups are substituted for an *iso*-butyl or an even bulkier *tert*-butyl group. These attempts, however, come with their own challenges: If one attempts the synthesis in a similar way as in Ni(TPBT), one has to cleave the respective porphyrinato iron(III) complex first. While synthesis of the metal-free porphyrins has been well documented[180] by Senge *et al.*, they also describe that the additional sterical crowding severely bends the porphyrins out of planarity. As a result, their *meso*-positions become highly nucleophilic and unexpected side reactions are observed if typical metalation procedures (metal acetate in MeOH/$CHCl_3$) are used. In his own experiments with H_2TTBP, the author of this thesis found that metalation with $FeCl_2$ in refluxing DMF neither showed presence of the initial educt, the expected metalloporphyrin nor any typical cleavage products thereof, as per EI-MS analysis of the crude reaction mixture after 1 h. Additionally, one has to consider that even a

moderate pitch in the helical compounds (as shown earlier) makes these molecules similarly susceptible to even weak nucleophiles such as water or methanol. While this behavior will likely establish some sort of "sweet spot" as a compromise between helical pitch and synthetic feasibility, the quest for subjecting the tetrapyrrole backbone to a maximum of sterical abuse remains interesting for further work; not only for the research of chirality-induced spin selectivity but for the field of porphyrinoid research as well.

6.1.2 Helix Length

While this work has been exclusively concerned with the metal complexes of tetrapyrroles, the scope can of course easily be expanded to higher oligopyrroles such as the penta- and hexapyrroles by employing the Lindsey condensation[181–184].

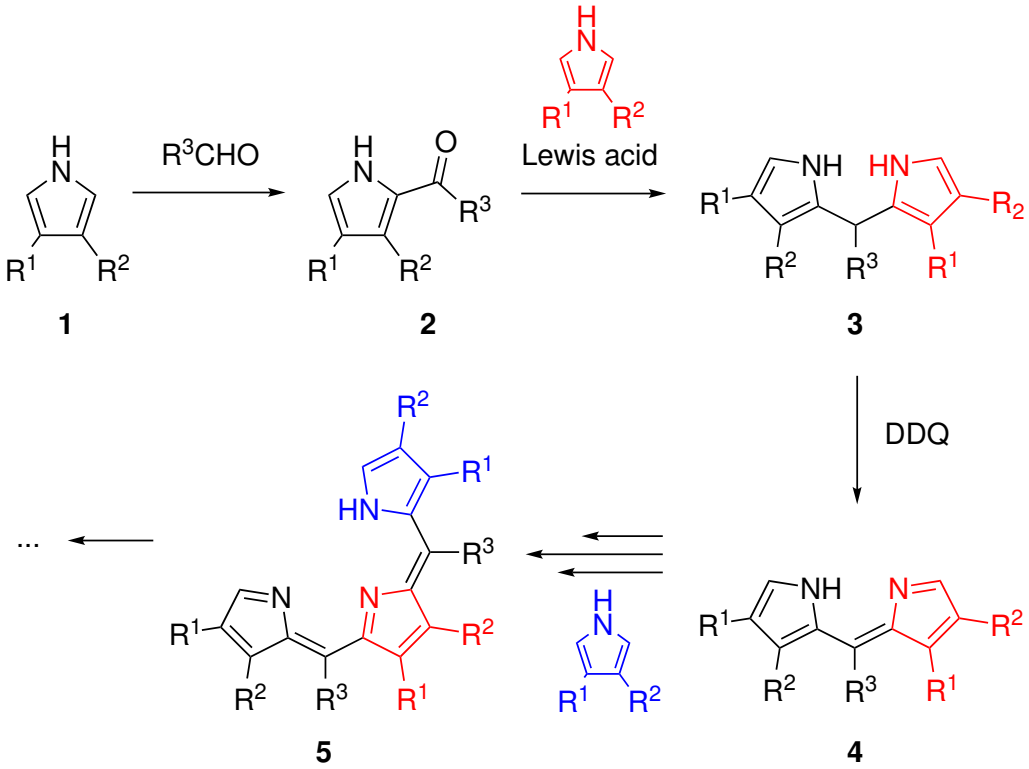

Figure 6.2: Synthesis of oligopyrroles under Lindsey conditions, shown here until the trimer. Note that the residues R do not have to be equal.

The synthesis commences with the formylation of a suitable pyrrole **1** to give a 2-pyrrole-carbaldehyde **2** or a 2,4-pyrrole-dicarbaldehyde. The product, in turn, is then reacted with another pyrrole under Lewis acid catalysis (such as CF_3CO_2H, AcOH or $BF_3 \cdot OEt_2$) to give the corresponding dipyrromethane **3** from which – after optional oxidation with DDQ or chloranil to give the methene **4** – higher oligopyrroles such as **5** can be synthesized. This method has indeed been tried and tested for over half a century, and its scope includes the synthesis of the boron dipyrromethene (BODIPY) dyes[185] and porphyrins with asymmetric substitution patterns[184]. In some cases, incorporation of heteroatoms into the structure was successful. One example is the condensation of two tripyrroles with sulfur dichloride. While the exact reaction conditions are not clear – in it's first and only edition, Falk's book[147] cites source 685 as "in press" and no according publication could be found in the Web of Science –, the exact conditions are probably similar to a 1988 publication[186]. Moreover, as the higher oligomers provide more nitrogen atoms as electron pair donors, the stability of the complexes can be expected to increase due to the chelate effect, and complexation of the lanthanide metals may become feasible to give interesting properties for the fabrication of chiral OLEDs. In practice, this synthetic approach, if completely unsaturated molecules are desired, appears limited to the penta- and hexapyrroles[187,188] due to the instability of the higher oligomers[147] (see source 811 therein). While the exact reason for this decreasing stability has not been evaluated in literature to the author's knowledge, the considerable sterical strain due to deviation from planar sp^2 geometry will likely play a major role. Another problem arises if $R^1 \neq R^2$, as this lifts equivalence of the pyrrole carbons in 2- and 4-position and attach of the aldehyde will lead to a more complex mixture of pyrrolecarbaldehydes; a problem which in porphyrin chemistry has been named the "type-isomer problem"[58].

6.1.3 Electron Density

As the tetrapyrrole motif contains a long and highly π-conjugated system of carbon and nitrogen atoms, it stands to reason that electron-donating or withdrawing groups will have a strong effect on its electronic properties; This phenomenon that can be estimated from its peaks in the UV/vis spectra, in an effect that is known from college-level chemistry as a "hypochromic" or "hypsochromic" shift. Just as in Chapter 6.1.1, the compounds available for systematic comparison are severely limited. In the spectra[70] provided by Koerner *et al.*, the HOMO-LUMO transition – which in Chapter 4.3 on page 42 has been established to take place in the tetrapyrrole helix – can be found at 802 nm with $\varepsilon = 9.2{\times}10^3\,\mathrm{L\,mol^{-1}\,cm^{-1}}$, which is not much different than Ni(TPBT) both in wavelength (810 nm) and magnitude ($11.0{\times}10^3\,\mathrm{L\,mol^{-1}\,cm^{-1}}$), suggesting that more drastical differences in electron donation or withdrawal are needed for a substantial effect. To this end, several tetraphenylporphyrinato iron(III) have already been synthesized according to literature procedure[189,190], but their cleavage has not yet been attempted due to time constraints with the candidate's research project.
This point of systematic study is especially interesting, as to the author's knowledge, no sufficient emphasis has been placed on whether the electron density in a chiral structure affects its spin selectivity. Hence, it will be pursued by the author of this work in a subsequent postdoctoral endeavour.

6.1.4 Central Metal

As the main body of this work is concerned with the respective metal complexes of H_2TPBT (a tetradentate ligand) and because the "periodic table of porphyrins" has been almost complete since the 1980s[153], the question about integrating other metals into the TPBT system arises almost naturally. To this end, the synthesis of Ni(TPBT) carried out with different metal acetates: $Zn(OAc)_2$, $Cd(OAc)_2$, $Hg(OAc)_2$ and $Mn(OAc)_2$. All cases, however, were unsuccessful. The resulting zinc complex decomposed to the covalent hydrate during workup and the crude of the cadmium complex showed no product peak in the EI-MS spectrum. The mercury variant produced large amounts of

a blue solid that was insoluble in all organic solvents and could not be evaporated under EI-MS conditions. After final acetic acid reflux and neutralization of the manganese crude, a sizeable amount of what appeared to be mostly charred solid was recovered. Given the rich redox chemistry of manganese salts, it appeared likely that it had aided in decomposing the H_2TPBT, and the synthesis was abandoned. From this admittedly very limited experience, it seems that coordination of d-group elements is not as straightforward as it is with nickel and copper. Most metals for which this "acetate method" fails in the porphyrins are typically inserted with more drastical methods, such as via boiling the metal acetylacetonate in phenol[191,192], or via metal alkyls[193]. However, as most of these are at least moderately nucleophilic, it stands to reason that they are not compatible with H_2TPBT, as they would attack the molecule in 15-position and open the helix, similar to water or methanol, while being even more difficult to remove. Metals that have thus far been considered to be the most promising are cobalt and iron, providing that they are inserted under inert gas atmosphere to avoid the oxidation from M^{II} to M^{III}.

Similar attempts have been made with H_3TPBV, using nickel and copper while noting that reflux in acetic acid readily oxidized the educt. Reflux of H_3TPBV with $Al(acac)_3$ in phenol (or incubation in imidazol at 200 °C) have not been sucessful either, as they led to thermal decomposition. The most promising element to be inserted into the TPBV moiety clearly has to be boron, as the boron dipyrromethe (BODIPY) dyes to which they are related are known for their strong fluorescence and good quantum yield. Its insertion has thus far not been successful with $BF_3 \cdot OEt_2$ in $CHCl_3$ and DBU as a base under protective atmosphere. However, the author believes that the synthesis of B(TPBV) is generally possible after more optimization, as the crude often showed strong fluorescence under 365 nm light.

6.2 Chiral Closed-Chain Tetrapyrroles

Another approach for benchmarking the CISS effect with tetrapyrroles comes in the form of chiral porphyrins, specifically their N,N-dimethylated species. In as far back as 1977, Al-Hazimi *et al.* could show[194] that reacting H_2TPP with methyl iodide and K_2CO_3 metalated the porphyrin on adjacent nitrogen atoms. The resulting *trans*-N_a,N_b-dimethyltetraphenylporphyrin is inversion-asymmetric while retaining its 22 π electrons and thus its aromaticity and ring current effects. Moreover, similar to the Ni(TPBT) molecule introduced in this work, the chiral porphyrin absorbs light in the near infrared range at 710 nm. While its surface chemistry and physics is still unexplored, H_2TPP has been well established and characterized in this field by now and the differences in, for example, adsorption behavior can be reasonably expected to not differ. Both N_a,N_b-dimethyl-TPP and the M(TPBT) have the highly symmetric H_2TPP as a common precursor for which, as mentioned above, modification of the phenyl substituents are vast and systematic variations should be just as easy while trading the strict helicity of the TPBT complexes with a higher tolerance for nucleophiles. Thus, benchmarking the CISS effect with this group of porphyrins surely presents another dissertation in its own right and is under further consideration for follow-up work. Nonetheless, preliminary experience with this molecule has thus far shown that the synthesis by Hazimi *et al.* is reproducible and the enantiomers are separable with mixtures of IPA/$CHCl_3$ in principle, but at considerable losses due to peak overlap.

6.3 Closing Remarks

This dissertation has been concerned with connecting the broad field of open-chain tetrapyrroles and its complexes with the rapidly moving field of organic spintronics. To this end, several of these molecules were synthesized up to a potential gram-scale. Apart from the noninnocent copper complexes, all other molecules showed a variety of properties making them interesting not only for the field of spintronics but for the fields of molecular electronics and nanotechnology as well. This group of molecules is not only easy to

synthesize from simple precursors, they also give smooth surfaces from spin-coating with ease, requiring very little optimization. Lastly, the CISS effect revealed by magnetoconductive AFM and Mott polarimetry is outstanding for organic molecules, although their rich electrochemistry does interfere with the recording of the $I(V)$ curves at least to some extent. Literature review has revealed the plethora of options for a more systematic study of the CISS effect which is believed to aid in the development of a truly concise theoretical model of this intriguing phenomenon, hopefully in the near future. Furthermore, it is hoped by the author that this dissertation not only served its original purpose but also made the field of tetrapyrrole chemistry appealing to the reader in general; a field that – from his impressions of three years – is just as fascinating as it is currently barren and in dire need of a "revival". Until then, the next section is dedicated to expressing the utmost gratitude of the author to all the people making this piece of work possible.

Chapter 7

Acknowledgements

Writing a dissertation is not an easy task. Neither is it to write said dissertation in a different country or during a global pandemic. Hence, I have more people to thank for than I would do under typical circumstances.

Firstly, I would like to thank my mother Elke Urban for giving me the gift of life that evolved into so much more than I could have possibly fathomed when I was still a child. Furthermore, I am deeply thankful for my entire family for their love, inspiration and support, both during my time in Germany and my time in Japan. All words of every language ever invented by man cannot grasp the love I feel for you. I would also like to thank my girlfriend for her incredible love that continues to transcend geographical and cultural boundaries.

From the academic side, I would firstly like to thank Prof. Hiroshi Yamamoto for accepting me to IMS, for giving me invaluable help and feedback along every step of this three-year journey, and for giving me enough leeway to pursue my own inspirations. His workgroup has always been a pleasure to work with, no matter the project at hand. Then, of course, my gratitude goes towards the thesis evaluation committee, consisting of Prof. Kazuyuki Ishii and Prof. Masahiro Ehara. The latter of which I would like to thank especially for his valuable guidance concerning the gas phase DFT calculations. I would also like to thank the entire Yamamoto work group at IMS for accepting me

as their colleague, for the exciting discussions and seminars, and for the great time both inside and outside this institute.

To the entirety of NINS, I am deeply indebted, both for help with starting my life here in Okazaki and for providing me with measurement time and valuable input. Regarding the further, I am most indebted to Ms. Hisayo Nagasono and Mr. Ryosuke Murata. Regarding the latter, I would like to thank Dr. Daichi Hirobe and Dr. Takuro Sato for their help with experimental advice concerning all areas of physical theory and nanofabrication. I would also like to thank Prof. Emi Minamitani for her advice on my calculations of molecules on surfaces. Of the Instrument Center, I would like to especially thank Dr. Taketoshi Minato, Dr. Kei-ichi Nakamoto and Dr. Tadashi Ueda for their assistance in the mc-AFM measurements, Dr. Haruyo Nagao for assistance with the 2 D NMR measurements, Dr. Yoshinori Okano for assisting with x-ray crystallography, and Dr. Motoyasu Fujiwara for assistance with the ESR experiments. I would further like to thank the Research Center for Computational Science for providing computational time and the coffee machine of the CIMOS building for the much needed caffeine. Of course, I would also like to thank the guard office of NINS as well as the Okazaki Fire Department for their invaluable help during early stages of recreating the H_3TPBV synthesis of Matsuura *et al.*

My colleagues back at the University of Münster in Germany, especially Paul Möllers and Tobias Reiker, I would like to thank for the valuable input about my work and for the inspiration that led to our collaborative effort. Moreover, I would like to especially thank Prof. Helmut Zacharias who made the contact with Prof. Yamamoto possible in the first place.

I would also like to thank all the people in Okazaki, the Aichi prefecture and the entire country of Japan for welcoming me into this incredible country and for all the amazing discoveries and encounters I was able to make in my three years here. Of all of these, I would like to especially thank Shintaro Takaoka, who was my pen-pal since elementary school and has been a great friend ever since then.

Financial support by the Japanese Ministry of Education, Culture, Sports, Science and Technology (MEXT) in the form of its MEXT Scholarship (Monbukagakusho) is gratefully acknowledged.

Bibliography

[1] Ray, K.; Ananthavel, S. P.; Waldeck, D. H.; Naaman, R. *Science* **1999**, *283*, 814–816.

[2] Kettner, M.; Maslyuk, V. V.; Nürenberg, D.; Seibel, J.; Gutierrez, R.; Cuniberti, G.; Ernst, K.-H.; Zacharias, H. *The Journal of Physical Chemistry Letters* **2018**, *9*, 2025–2030.

[3] Kondou, K.; Shiga, M.; Sakamoto, S.; Inuzuka, H.; Nihonyanagi, A.; Araoka, F.; Kobayashi, M.; Miwa, S.; Miyajima, D.; Otani, Y. *Journal of the American Chemical Society* **2022**, *144*, 7302–7307.

[4] Suda, M.; Thathong, Y.; Promarak, V.; Kojima, H.; Nakamura, M.; Shiraogawa, T.; Ehara, M.; Yamamoto, H. M. *Nature Communications* **2019**, *10*.

[5] Carmeli, I.; Skakalova, V.; Naaman, R.; Vager, Z. *Angewandte Chemie International Edition* **2002**, *41*, 761.

[6] Göhler, B.; Hamelbeck, V.; Markus, T. Z.; Kettner, M.; Hanne, G. F.; Vager, Z.; Naaman, R.; Zacharias, H. *Science* **2011**, *331*, 894–897.

[7] Xie, Z.; Markus, T. Z.; Cohen, S. R.; Vager, Z.; Gutierrez, R.; Naaman, R. *Nano Letters* **2011**, *11*, 4652–4655.

[8] Kettner, M.; Bhowmick, D. K.; Bartsch, M.; Göhler, B.; Zacharias, H. *Advanced Materials Interfaces* **2016**, *3*, 1600595.

[9] Mondal, P. C.; Kantor-Uriel, N.; Mathew, S. P.; Tassinari, F.; Fontanesi, C.; Naaman, R. *Advanced Materials* **2015**, *27*, 1924–1927.

[10] Bhowmick, D.; Sang, Y.; Santra, K.; Halbauer, M.; Capua, E.; Paltiel, Y.; Naaman, R.; Tassinari, F. *Crystal Growth & Design* **2021**, *21*, 2925–2931.

[11] Mondal, P. C.; Fontanesi, C.; Waldeck, D. H.; Naaman, R. *ACS Nano* **2015**, *9*, 3377–3384.

[12] Aiello, C. D.; et al. *ACS Nano* **2022**, *16*, 4989–5035.

[13] Clever, C.; Wierzbinski, E.; Bloom, B. P.; Lu, Y.; Grimm, H. M.; Rao, S. R.; Horne, W. S.; Waldeck, D. H. *Israel Journal of Chemistry* **2022**, *62*.

[14] Evers, F.; et al. *Advanced Materials* **2022**, *34*, 2106629.

[15] Yeganeh, S.; Ratner, M. A.; Medina, E.; Mujica, V. *The Journal of Chemical Physics* **2009**, *131*, 014707.

[16] Du, G.-F.; Fu, H.-H.; Wu, R. *Physical Review B* **2020**, *102*.

[17] Zhang, L.; Hao, Y.; Qin, W.; Xie, S.; Qu, F. *Physical Review B* **2020**, *102*.

[18] Fransson, J. *The Journal of Physical Chemistry Letters* **2019**, *10*, 7126–7132.

[19] Dianat, A.; Gutierrez, R.; Alpern, H.; Mujica, V.; Ziv, A.; Yochelis, S.; Millo, O.; Paltiel, Y.; Cuniberti, G. *Nano Letters* **2020**, *20*, 7077–7086.

[20] Li, X.; Nan, J.; Pan, X. *Physical Review Letters* **2020**, *125*.

[21] Kulkarni, C.; Mondal, A. K.; Das, T. K.; Grinbom, G.; Tassinari, F.; Mabesoone, M. F. J.; Meijer, E. W.; Naaman, R. *Advanced Materials* **2020**, *32*, 1904965.

[22] Bloom, B. P.; Graff, B. M.; Ghosh, S.; Beratan, D. N.; Waldeck, D. H. *Journal of the American Chemical Society* **2017**, *139*, 9038–9043.

[23] Mishra, S.; Mondal, A. K.; Pal, S.; Das, T. K.; Smolinsky, E. Z. B.; Siligardi, G.; Naaman, R. *The Journal of Physical Chemistry C* **2020**, *124*, 10776–10782.

[24] Amsallem, D.; Kumar, A.; Naaman, R.; Gidron, O. *Chirality* **2023**.

[25] Wikimedia Commons user "Eyal.capua"; *A schematic representation of the chiral-induced spin selectivity (CISS) effect.*; Wikimedia Commons, licensed under the Creative Commons Attribution-Share Alike 4.0 International; 2015. `https://commons.wikimedia.org/wiki/File:CISS_Effect.png`.

[26] Gersten, J.; Kaasbjerg, K.; Nitzan, A. *The Journal of Chemical Physics* **2013**, *139*, 114111.

[27] Sukenik, N.; Tassinari, F.; Yochelis, S.; Millo, O.; Baczewski, L. T.; Paltiel, Y. *Molecules* **2020**, *25*, 6036.

[28] Alwan, S.; Dubi, Y. *Journal of the American Chemical Society* **2021**, *143*, 14235–14241.

[29] Kumar, A.; Capua, E.; Kesharwani, M. K.; Martin, J. M. L.; Sitbon, E.; Waldeck, D. H.; Naaman, R. *Proceedings of the National Academy of Sciences* **2017**, *114*, 2474–2478.

[30] Kumar, A.; Capua, E.; Vankayala, K.; Fontanesi, C.; Naaman, R. *Angewandte Chemie International Edition* **2017**, *56*, 14587–14590.

[31] Wang, J.; Lu, H.; Pan, X.; Xu, J.; Liu, H.; Liu, X.; Khanal, D. R.; Toney, M. F.; Beard, M. C.; Vardeny, Z. V. *ACS Nano* **2020**, *15*, 588–595.

[32] Mtangi, W.; Tassinari, F.; Vankayala, K.; Jentzsch, A. V.; Adelizzi, B.; Palmans, A. R. A.; Fontanesi, C.; Meijer, E. W.; Naaman, R. *Journal of the American Chemical Society* **2017**, *139*, 2794–2798.

[33] Tassinari, F.; Banerjee-Ghosh, K.; Parenti, F.; Kiran, V.; Mucci, A.; Naaman, R. *The Journal of Physical Chemistry C* **2017**, *121*, 15777–15783.

[34] Zhang, W.; Banerjee-Ghosh, K.; Tassinari, F.; Naaman, R. *ACS Energy Letters* **2018**, *3*, 2308–2313.

[35] Ghosh, K. B.; Zhang, W.; Tassinari, F.; Mastai, Y.; Lidor-Shalev, O.; Naaman, R.; Möllers, P.; Nürenberg, D.; Zacharias, H.; Wei, J.; et al. *The Journal of Physical Chemistry C* **2019**, *123*, 3024–3031.

[36] Metzger, T. S.; Mishra, S.; Bloom, B. P.; Goren, N.; Neubauer, A.; Shmul, G.; Wei, J.; Yochelis, S.; Tassinari, F.; Fontanesi, C.; Waldeck, D. H.; Paltiel, Y.; Naaman, R. *Angewandte Chemie International Edition* **2019**, *59*, 1653–1658.

[37] Bloom, B. P.; Lu, Y.; Metzger, T.; Yochelis, S.; Paltiel, Y.; Fontanesi, C.; Mishra, S.; Tassinari, F.; Naaman, R.; Waldeck, D. H. *Physical Chemistry Chemical Physics* **2020**, *22*, 21570–21582.

[38] Ghosh, S.; Mishra, S.; Avigad, E.; Bloom, B. P.; Baczewski, L. T.; Yochelis, S.; Paltiel, Y.; Naaman, R.; Waldeck, D. H. *The Journal of Physical Chemistry Letters* **2020**, *11*, 1550–1557.

[39] Ghosh, S.; Bloom, B. P.; Lu, Y.; Lamont, D.; Waldeck, D. H. *The Journal of Physical Chemistry C* **2020**, *124*, 22610–22618.

[40] Metzger, T. S.; Siam, R.; Kolodny, Y.; Goren, N.; Sukenik, N.; Yochelis, S.; Abu-Reziq, R.; Avnir, D.; Paltiel, Y. *The Journal of Physical Chemistry Letters* **2021**, *12*, 5469–5472.

[41] Dor, O. B.; Yochelis, S.; Mathew, S. P.; Naaman, R.; Paltiel, Y. *Nature Communications* **2013**, *4*.

[42] Koplovitz, G.; Primc, D.; Dor, O. B.; Yochelis, S.; Rotem, D.; Porath, D.; Paltiel, Y. *Advanced Materials* **2017**, *29*, 1606748.

[43] Al-Bustami, H.; Koplovitz, G.; Primc, D.; Yochelis, S.; Capua, E.; Porath, D.; Naaman, R.; Paltiel, Y. *Small* **2018**, *14*, 1801249.

[44] Koplovitz, G.; Leitus, G.; Ghosh, S.; Bloom, B. P.; Yochelis, S.; Rotem, D.; Vischio, F.; Striccoli, M.; Fanizza, E.; Naaman, R.; Waldeck, D. H.; Porath, D.; Paltiel, Y. *Small* **2018**, *15*, 1804557.

[45] Al-Bustami, H.; Bloom, B. P.; Ziv, A.; Goldring, S.; Yochelis, S.; Naaman, R.; Waldeck, D. H.; Paltiel, Y. *Nano Letters* **2020**, *20*, 8675–8681.

[46] Goren, N.; Das, T. K.; Brown, N.; Gilead, S.; Yochelis, S.; Gazit, E.; Naaman, R.; Paltiel, Y. *Nano Letters* **2021**, *21*, 8657–8663.

[47] Yang, S.-H.; Naaman, R.; Paltiel, Y.; Parkin, S. S. P. *Nature Reviews Physics* **2021**, *3*, 328–343.

[48] Nuzzo, D. D.; Kulkarni, C.; Zhao, B.; Smolinsky, E.; Tassinari, F.; Meskers, S. C. J.; Naaman, R.; Meijer, E. W.; Friend, R. H. *ACS Nano* **2017**, *11*, 12713–12722.

[49] Kim, Y.-H.; Zhai, Y.; Lu, H.; Pan, X.; Xiao, C.; Gaulding, E. A.; Harvey, S. P.; Berry, J. J.; Vardeny, Z. V.; Luther, J. M.; Beard, M. C. *Science* **2021**, *371*, 1129–1133.

[50] Banerjee-Ghosh, K.; Dor, O. B.; Tassinari, F.; Capua, E.; Yochelis, S.; Capua, A.; Yang, S.-H.; Parkin, S. S. P.; Sarkar, S.; Kronik, L.; Baczewski, L. T.; Naaman, R.; Paltiel, Y. *Science* **2018**, *360*, 1331–1334.

[51] Tassinari, F.; Steidel, J.; Paltiel, S.; Fontanesi, C.; Lahav, M.; Paltiel, Y.; Naaman, R. *Chemical Science* **2019**, *10*, 5246–5250.

[52] Metzger, T. S.; Tokatly, Y.; Avigad, E.; Yochelis, S.; Paltiel, Y. *Separation and Purification Technology* **2020**, *239*, 116501.

[53] Santra, K.; Bhowmick, D.; Zhu, Q.; Bendikov, T.; Naaman, R. *The Journal of Physical Chemistry C* **2021**, *125*, 17530–17536.

[54] Wang, C.; Guo, A.-M.; Sun, Q.-F.; Yan, Y. *The Journal of Physical Chemistry Letters* **2021**, *12*, 10262–10269.

[55] Jeremy M. Berg, L. S., John L. Tymoczko *Biochemistry*, 6th ed.; W. H. Freeman and Company, New York, 2006; Chapter 24. The Biosynthesis of Amino Acids, pp 704–705.

[56] Warburg, O.; Negelein, E. *Berichte der deutschen chemischen Gesellschaft (A and B Series)* **1930**, *63*, 1816–1818.

[57] Albert Guijarro, M. Y. *The Origin of Chirality in the Molecules of Life. A Revision from Awareness to the Current Theories and Perspectives of this Unsolved Problem*; RSC Publishing, 2009.

[58] Senge, M. O.; Sergeeva, N. N.; Hale, K. J. *Chemical Society Reviews* **2021**, *50*, 4730–4789.

[59] Evans, B.; Smith, K. M.; Cavaleiro, J. A. S. *Tetrahedron Letters* **1976**, *17*, 4863–4866.

[60] Evans, B.; Smith, K. M.; Cavaleiro, J. A. S. *Journal of the Chemical Society, Perkin Transactions 1* **1978**, 768.

[61] Smith, K. M.; Brown, S. B.; Troxler, R. F.; Lai, J.-J. *Photochemistry and Photobiology* **1982**, *36*, 147–152.

[62] Fuhrhop, J. H.; Mauzerall, D. *Journal of the American Chemical Society* **1969**, *91*, 4174–4181.

[63] Wasser, P. K. W.; Fuhrhop, J.-H. *Annals of the New York Academy of Sciences* **1973**, *206*, 533–548.

[64] Fuhrhop, J.-H.; Mauerzall, D. *Photochemistry and Photobiology* **1971**, *13*, 453–458.

[65] Fuhrhop, J. H.; Salek, A.; Subramanian, J.; Mengersen, C.; Besecke, S. *Justus Liebigs Annalen der Chemie* **1975**, 1131–1147.

[66] Balch, A. L.; Latos-Grazynski, L.; Noll, B. C.; Olmstead, M. M.; Safari, N. *Journal of the American Chemical Society* **1993**, *115*, 9056–9061.

[67] Balch, A. L.; Mazzanti, M.; Noll, B. C.; Olmstead, M. M. *Journal of the American Chemical Society* **1994**, *116*, 9114–9122.

[68] Attar, S.; Balch, A. L.; Van Calcar, P. M.; Winkler, K. *Journal of the American Chemical Society* **1997**, *119*, 3317–3323.

[69] Koerner, R.; Olmstead, M. M.; Calcar, P. M. V.; Winkler, K.; Balch, A. L. *Inorganic Chemistry* **1998**, *37*, 982–988.

[70] Koerner, R.; Olmstead, M. M.; Ozarowski, A.; Phillips, S. L.; Van Calcar, P. M.; Winkler, K.; Balch, A. L. *Journal of the American Chemical Society* **1998**, *120*, 1274–1284.

[71] Koerner, R.; Olmstead, M. M.; Ozarowski, A.; Balch, A. L. *Inorganic Chemistry* **1999**, *38*, 3262–3263.

[72] Lord, P.; Olmstead, M. M.; Balch, A. L. *Angewandte Chemie International Edition* **1999**, *38*, 2761–2763.

[73] Johnson, J. A.; Olmstead, M. M.; Balch, A. L. *Inorganic Chemistry* **1999**, *38*, 5379–5383.

[74] Mizutani, T.; Yagi, S.; Honmaru, A.; Murakami, S.; Furusyo, M.; Takagishi, T.; Ogoshi, H. *The Journal of Organic Chemistry* **1998**, *63*, 8769–8784.

[75] Mizutani, T.; Yagi, S.; Honmaru, A.; Goldacker, T.; Kitagawa, S.; Furusyo, M.; Takagishi, T.; Ogoshi, H. *Supramolecular Chemistry* **1999**, *10*, 297–308.

[76] Mizutani, T.; Yagi, S. *Journal of Porphyrins and Phthalocyanines* **2004**, *08*, 226–237.

[77] Yamauchi, T.; Mizutani, T.; Wada, K.; Horii, S.; Furukawa, H.; Masaoka, S.; Chang, H.-C.; Kitagawa, S. *Chem. Commun.* **2005**, 1309–1311.

[78] Kita, K.; Tokuoka, T.; Monno, E.; Yagi, S.; Nakazumi, H.; Mizutani, T. *Tetrahedron Letters* **2006**, *47*, 1533–1536.

[79] Matsui, E.; Matsuzawa, N.; Harnack, O.; Yamauchi, T.; Hatazawa, T.; Yasuda, A.; Mizutani, T. *Advanced Materials* **2006**, *18*, 2523–2528.

[80] Asano, N.; Uemura, S.; Kinugawa, T.; Akasaka, H.; Mizutani, T. *The Journal of Organic Chemistry* **2007**, *72*, 5320–5326.

[81] Furuta, N.; Mizutani, T. *Supramolecular Chemistry* **2010**, *23*, 74–82.

[82] Nakamura, R.; Kakeya, K.; Furuta, N.; Muta, E.; Nishisaka, H.; Mizutani, T. *The Journal of Organic Chemistry* **2011**, *76*, 6108–6115; PMID: 21688807.

[83] Kakeya, K.; Aozasa, M.; Mizutani, T.; Hitomi, Y.; Kodera, M. *The Journal of Organic Chemistry* **2014**, *79*, 2591–2600; PMID: 24597593.

[84] Kakeya, K.; Shimizu, A.; Akasaka, K.; Mizutani, T. *Journal of Porphyrins and Phthalocyanines* **2015**, *19*, 726–733.

[85] Mizutani, T. *Journal of Porphyrins and Phthalocyanines* **2016**, *20*, 108–116.

[86] Cavaleiro, J. A. S.; Neves, M. G. P. S.; Hewlins, M. J. E.; Jackson, A. H. *Journal of the Chemical Society, Perkin Transactions 1* **1990**, 1937.

[87] Matsuura, T.; Inoue, K.; Ranade, A. C.; Saito, I. *Photochemistry and Photobiology* **1980**, *31*, 23–26.

[88] Naaman, R.; Waldeck, D. H. *Annual Review of Physical Chemistry* **2015**, *66*, 263–281.

[89] Dubi, Y. *Chemical Science* **2022**, *13*, 10878–10883.

[90] Holleman, A. F.; und Nils Wiberg, E.; Fischer, G. *Inorganic Chemistry*; Walter de Gruyter, 2007.

[91] Clayden, J.; Greeves, N.; Warren, S.; Geeves, N. *Organic Chemistry*; Oxford University Press, 2012.

[92] Urban, A. J.; Yamamoto, H. M. *Chemistry – A European Journal* **2023**.

[93] Adler, A. D.; Longo, F. R.; Finarelli, J. D.; Goldmacher, J.; Assour, J.; Korsakoff, L. *The Journal of Organic Chemistry* **1967**, *32*, 476–476.

[94] Adler, A. D.; Longo, F. R.; Kampas, F.; Kim, J. *Journal of Inorganic and Nuclear Chemistry* **1970**, *32*, 2443–2445.

[95] Abbe, E. *Archiv für Mikroskopische Anatomie* **1873**, *9*, 413–468.

[96] Gross, H.; Blechinger, F.; Achtner, B. *Handbook of Optical Systems*; Wiley-VCH Weinheim Germany, 2008; Vol. 4.

[97] Berova, N.; Bari, L. D.; Pescitelli, G. *Chemical Society Reviews* **2007**, *36*, 914.

[98] Kelly, S. M.; Jess, T. J.; Price, N. C. *Biochimica et Biophysica Acta (BBA) - Proteins and Proteomics* **2005**, *1751*, 119–139.

[99] Szabo, A.; Ostlund, N. S. *Modern Quantum Chemistry: Introduction to Advanced Electronic Structure Theory*; Dover Publications Inc., 1996.

[100] Cramer, C. J. *Essentials of Computational Chemistry*; John Wiley & Sons Ltd., 2002.

[101] Jensen, F. *Introduction to Computational Chemistry*; John Wiley & Sons Ltd, 2007.

[102] Neese, F. *WIREs Computational Molecular Science* **2011**, *2*, 73–78.

[103] Neese, F. *WIREs Computational Molecular Science* **2017**, *8*, e1327.

[104] Neese, F. *WIREs Computational Molecular Science* **2022**, *12*, e1606.

[105] Becke, A. D. *The Journal of Chemical Physics* **1993**, *98*, 1372–1377.

[106] Lin, Y.-S.; Li, G.-D.; Mao, S.-P.; Chai, J.-D. *Journal of Chemical Theory and Computation* **2012**, *9*, 263–272.

[107] Yanai, T.; Tew, D. P.; Handy, N. C. *Chemical Physics Letters* **2004**, *393*, 51–57.

[108] Krishnan, R.; Binkley, J. S.; Seeger, R.; Pople, J. A. *The Journal of Chemical Physics* **1980**, *72*, 650–654.

[109] Weigend, F.; Ahlrichs, R. *Physical Chemistry Chemical Physics* **2005**, *7*, 3297.

[110] Weigend, F. *Physical Chemistry Chemical Physics* **2006**, *8*, 1057.

[111] Rappoport, D.; Furche, F. *The Journal of Chemical Physics* **2010**, *133*, 134105.

[112] Jensen, F. *The Journal of Chemical Physics* **2001**, *115*, 9113–9125.

[113] Jensen, F. *The Journal of Chemical Physics* **2002**, *116*, 7372–7379.

[114] Jensen, F. *The Journal of Chemical Physics* **2002**, *117*, 9234–9240.

[115] Jensen, F. *The Journal of Chemical Physics* **2013**, *138*, 014107.

[116] Clark, T.; Chandrasekhar, J.; Spitznagel, G. W.; Schleyer, P. V. R. *Journal of Computational Chemistry* **1983**, *4*, 294–301.

[117] Grimme, S.; Ehrlich, S.; Goerigk, L. *Journal of Computational Chemistry* **2011**, *32*, 1456–1465.

[118] Grimme, S.; Neese, F. *The Journal of Chemical Physics* **2007**, *127*, 154116.

[119] Neese, F. *Journal of Computational Chemistry* **2003**, *24*, 1740–1747.

[120] Izsák, R.; Neese, F. *The Journal of Chemical Physics* **2011**, *135*, 144105.

[121] Stoychev, G. L.; Auer, A. A.; Neese, F. *Journal of Chemical Theory and Computation* **2017**, *13*, 554–562.

[122] Dunning, T. H. *The Journal of Chemical Physics* **1989**, *90*, 1007–1023.

[123] Kendall, R. A.; Dunning, T. H.; Harrison, R. J. *The Journal of Chemical Physics* **1992**, *96*, 6796–6806.

[124] Balabanov, N. B.; Peterson, K. A. *The Journal of Chemical Physics* **2005**, *123*, 064107.

[125] Balabanov, N. B.; Peterson, K. A. *The Journal of Chemical Physics* **2006**, *125*, 074110.

[126] Dolg, M.; Wedig, U.; Stoll, H.; Preuss, H. *The Journal of Chemical Physics* **1987**, *86*, 866–872.

[127] Barone, V.; Cossi, M. *The Journal of Physical Chemistry A* **1998**, *102*, 1995–2001.

[128] Garcia-Ratés, M.; Neese, F. *Journal of Computational Chemistry* **2019**, *41*, 922–939.

[129] Giannozzi, P.; et al. *Journal of Physics: Condensed Matter* **2009**, *21*, 395502.

[130] Giannozzi, P.; et al. *Journal of Physics: Condensed Matter* **2017**, *29*, 465901.

[131] Giannozzi, P.; Baseggio, O.; Bonfà, P.; Brunato, D.; Car, R.; Carnimeo, I.; Cavazzoni, C.; de Gironcoli, S.; Delugas, P.; Ruffino, F. F.; Ferretti, A.; Marzari, N.; Timrov, I.; Urru, A.; Baroni, S. *The Journal of Chemical Physics* **2020**, *152*, 154105.

[132] Perdew, J. P.; Ernzerhof, M.; Burke, K. *The Journal of Chemical Physics* **1996**, *105*, 9982–9985.

[133] Methfessel, M.; Paxton, A. T. *Physical Review B* **1989**, *40*, 3616–3621.

[134] Monkhorst, H. J.; Pack, J. D. *Physical Review B* **1976**, *13*, 5188–5192.

[135] Tersoff, J.; Hamann, D. R. *Physical Review B* **1985**, *31*, 805–813.

[136] Hanwell, M. D.; Curtis, D. E.; Lonie, D. C.; Vandermeersch, T.; Zurek, E.; Hutchison, G. R. *Journal of Cheminformatics* **2012**, *4*, 17.

[137] Humphrey, W.; Dalke, A.; Schulten, K. *Journal of Molecular Graphics* **1996**, *14*, 33–38.

[138] Momma, K.; Izumi, F. *Journal of Applied Crystallography* **2011**, *44*, 1272–1276.

[139] de-la Roza, A. O.; Blanco, M.; Pendás, A. M.; Luaña, V. *Computer Physics Communications* **2009**, *180*, 157–166.

[140] de-la Roza, A. O.; Johnson, E. R.; Luaña, V. *Computer Physics Communications* **2014**, *185*, 1007–1018.

[141] Sheldrick, G. M. *Acta Crystallographica Section C Structural Chemistry* **2015**, *71*, 3–8.

[142] Sheldrick, G. M. *Acta Crystallographica Section A Foundations and Advances* **2015**, *71*, 3–8.

[143] Dolomanov, O. V.; Bourhis, L. J.; Gildea, R. J.; Howard, J. A. K.; Puschmann, H. *Journal of Applied Crystallography* **2009**, *42*, 339–341.

[144] Falk, H.; Neufingerl, F. *Monatshefte für Chemie* **1979**, *110*, 1243–1255.

[145] Falk, H.; Neufingerl, F. *Monatshefte für Chemie - Chemical Monthly* **1979**, *110*, 987–1001.

[146] Aussenegg, F. R.; Lippitsch, M. E.; Riegler, M. *Laser Chemistry* **1986**, *6*, 269–289.

[147] Falk, H. *The Chemistry of Linear Oligopyrroles and Bile Pigments*, 1st ed.; Monatshefte für Chemie Chemical Monthly Supplementa №1; Springer Vienna, 1989.

[148] Wodrich, M. D.; Corminboeuf, C.; von Ragué Schleyer, P. *Organic Letters* **2006**, *8*, 3631–3634.

[149] Schreiner, P. R.; Fokin, A. A.; Pascal, R. A.; de Meijere, A. *Organic Letters* **2006**, *8*, 3635–3638.

[150] Castro-Alvarez, A.; Carneros, H.; Sánchez, D.; Vilarrasa, J. *The Journal of Organic Chemistry* **2015**, *80*, 11977–11985.

[151] Bursch, M.; Mewes, J.-M.; Hansen, A.; Grimme, S. *Angewandte Chemie* **2022**, *134*, e202205735.

[152] Bogojeski, M.; Vogt-Maranto, L.; Tuckerman, M. E.; Müller, K.-R.; Burke, K. *Nature Communications* **2020**, *11*.

[153] Dolphin, D. *The Porphyrins. Structure and Synthesis, Part B*; Academic Press, 1978.

[154] Lord, P. A.; Noll, B. C.; Olmstead, M. M.; Balch, A. L. *Journal of the American Chemical Society* **2001**, *123*, 10554–10559; PMID: 11673987.

[155] Subramanian, J.; Fuhrhop, J.-H.; Salek, A.; Gossauer, A. *Journal of Magnetic Resonance (1969)* **1974**, *15*, 19–30.

[156] Goerigk, L.; Grimme, S. *The Journal of Physical Chemistry A* **2008**, *113*, 767–776.

[157] Ortuño, A. M.; Reiné, P.; Resa, S.; de Cienfuegos, L. Á.; Blanco, V.; Paredes, J. M.; Mota, A. J.; Mazzeo, G.; Abbate, S.; Ugalde, J. M.; Mujica, V.; Longhi, G.; Miguel, D.; Cuerva, J. M. *Organic Chemistry Frontiers* **2021**, *8*, 5071–5086.

[158] Switzer, J. A.; Kothari, H. M.; Poizot, P.; Nakanishi, S.; Bohannan, E. W. *Nature* **2003**, *425*, 490–493.

[159] Arana, C.; Keshavarz, M.; Potts, K. T.; Abruña, H. D. *Inorganica Chimica Acta* **1994**, *225*, 285–295.

[160] Fang, Y.; Senge, M. O.; Caemelbecke, E. V.; Smith, K. M.; Medforth, C. J.; Zhang, M.; Kadish, K. M. *Inorganic Chemistry* **2014**, *53*, 10772–10778.

[161] Scudiero, L.; Barlow, D. E.; Hipps, K. W. *The Journal of Physical Chemistry B* **2001**, *106*, 996–1003.

[162] Yoshimoto, S.; Inukai, J.; Tada, A.; Abe, T.; Morimoto, T.; Osuka, A.; Furuta, H.; Itaya, K. *The Journal of Physical Chemistry B* **2004**, *108*, 1948–1954.

[163] Friesen, B. A.; Bhattarai, A.; Mazur, U.; Hipps, K. W. *Journal of the American Chemical Society* **2012**, *134*, 14897–14904.

[164] Chilukuri, B.; Mazur, U.; Hipps, K. W. *Phys. Chem. Chem. Phys.* **2014**, *16*, 14096–14107.

[165] Porath, D.; Goldstein, Y.; Grayevsky, A.; Millo, O. *Surface Science* **1994**, *321*, 81–88.

[166] White, J. *Thin Solid Films* **1974**, *22*, 23–35.

[167] Pettinger, B. *Molecular Physics* **2010**, *108*, 2039–2059.

[168] Walen, H.; Liu, D.-J.; Oh, J.; Lim, H.; Evans, J. W.; Kim, Y.; Thiel, P. A. *The Journal of Chemical Physics* **2015**, *143*, 014704.

[169] Tynkova, A.; Sidorenko, S.; Voloshko, S.; Rennie, A.; Vasylyev, M. *Vacuum* **2013**, *87*, 69–74.

[170] Atkins, P. W.; de Paula, J. *Atkins' Physical Chemistry*, 5th ed.; Wiley VCH, 2013.

[171] Möllers, P. V.; *Private communication.*

[172] Sherman, N. *Physical Review* **1956**, *103*, 1601–1607.

[173] Möllers, P. V.; Msc. thesis; Westfälische Wilhelms-Universität Münster; 2017.

[174] Möllers, P. V.; Ulku, S.; Jayarathna, D.; Tassinari, F.; Nürenberg, D.; Naaman, R.; Achim, C.; Zacharias, H. *Chirality* **2021**, *33*, 93–102.

[175] Möllers, P. V.; Wei, J.; Salamon, S.; Bartsch, M.; Wende, H.; Waldeck, D. H.; Zacharias, H. *ACS Nano* **2022**, *16*, 12145–12155.

[176] Balch, A. L.; *Private communication.*

[177] Lehner, H.; Riemer, W.; Schaffner, K. *Liebigs Annalen der Chemie* **1979**, *1979*, 1798–1801.

[178] Bonnett, R.; Buckley, D. G.; Hamzetash, D. *Journal of the Chemical Society, Perkin Transactions 1* **1981**, 322.

[179] Balch, A. L.; Mazzanti, M.; Noll, B. C.; Olmstead, M. M. *Journal of the American Chemical Society* **1993**, *115*, 12206–12207.

[180] Senge, M. O.; Bischoff, I.; Nelson, N. Y.; Smith, K. M. *Journal of Porphyrins and Phthalocyanines* **1999**, *03*, 99–116.

[181] Lindsey, J. S.; Hsu, H. C.; Schreiman, I. C. *Tetrahedron Letters* **1986**, *27*, 4969–4970.

[182] Lindsey, J. S.; Schreiman, I. C.; Hsu, H. C.; Kearney, P. C.; Marguerettaz, A. M. *The Journal of Organic Chemistry* **1987**, *52*, 827–836.

[183] Laha, J. K.; Dhanalekshmi, S.; Taniguchi, M.; Ambroise, A.; Lindsey, J. S. *Organic Process Research & Development* **2003**, *7*, 799–812.

[184] Lindsey, J. S. *Accounts of Chemical Research* **2009**, *43*, 300–311.

[185] Tram, K.; Yan, H.; Jenkins, H. A.; Vassiliev, S.; Bruce, D. *Dyes and Pigments* **2009**, *82*, 392–395.

[186] Falk, H.; Flödl, H.; Wagner, U. G. *Monatshefte für Chemie - Chemical Monthly* **1988**, *119*, 739–749.

[187] Falk, H.; Flödl, H. *Monatshefte für Chemie - Chemical Monthly* **1986**, *117*, 57–67.

[188] Wagner, U. G.; Kratky, C.; Falk, H.; Flödl, H. *Monatshefte für Chemie - Chemical Monthly* **1987**, *118*, 1185–1194.

[189] Longo, F. R.; Finarelli, M. G.; Kim, J. B. *Journal of Heterocyclic Chemistry* **1969**, *6*, 927–931.

[190] Ojadi, E. C. A.; Linschitz, H.; Gouterman, M.; Walter, R. I.; Lindsey, J. S.; Wagner, R. W.; Droupadi, P. R.; Wang, W. *The Journal of Physical Chemistry* **1993**, *97*, 13192–13197.

[191] Buchler, J. W.; Puppe, L.; Rohbock, K.; Schneehage, H. H. *Chemische Berichte* **1973**, *106*, 2710–2732.

[192] Buchler, J. W.; Folz, M.; Habets, H.; van Kaam, J.; Rohbock, K. *Chemische Berichte* **1976**, *109*, 1477–1485.

[193] Dolphin, D. *The Porphyrins. Physical Chemistry, Part C*; Academic Press, 1978.

[194] Al-Hazimi, H. M. G.; Jackson, A. H.; Johnson, A. W.; Winter, M. *Journal of the Chemical Society, Perkin Transactions 1* **1977**, 98.

Note: For publications that were originally composed in German, English translations can be provided by the author of this thesis upon request.

Appendix A

Curriculum Vitae

Born 1994-11-24 in Baton Rouge, LA, USA as Adrian Joe Hauser.
Current address: Tenmadori 1-6 Apt. 205, Okazaki City, Aichi prefecture, 444-0038 Japan

DISSERTATION 2020-12 –
Institute for Molecular Science (Okazaki, Japan) Chirality-Induced Spin Selectivity (CISS) in helical tetrapyrroles

M.SC. THESIS 2020-02
Center for Soft Nanoscience (Münster, Germany) "Wavelength-dependent kinetics of organophosphonate-SAM formation on H-terminated Si(111)". Supervisors: H. Zacharias and B. J. Ravoo

M.SC. STUDIES IN CHEMISTRY 2018–2020
Westfälische Wilhelms-Universität (Münster, Germany) Focus: Nanotechnology, physical and surface chemistry

B.SC. THESIS 2017-10
Westfälische Wilhelms-Universität (Münster, Germany) "Angle-resolved IPE

measurements of (3×2) silicon nanoribbons on the Ag(110) surface". Supervisors: H. Zacharias and M. Schönhoff

B.Sc. Studies in Chemistry 2013–2018
Westfälische Wilhelms-Universität (Münster, Germany) Focus: Nanotechnology, surface physics

Abitur 07-2013
Städt. Gymnasium Nepomucenum (Coesfeld, Germany)

Appendix B

List of Publications

Research Articles

- **2023-05**: A. Urban, H. M. Yamamoto "Strong and Tunable Near-Infrared Circular Dichroism in Helical Tetrapyrrole Complexes" Chem. Eur. J. **2023**, e202300940. DOI: 10.1002/chem.202300940.

Conference Posters

- **2023-07**: A. Urban, T. Minato, K. Nakamoto, T. Ueda, H. M. Yamamoto "Quantitative Spin Polarization of Tetrapyrrole Monolayers with Magneto-Conductive AFM" Gordon Research Conference "Chiral Spin Filtering and its Manifestations From Molecules to Devices". Manchester, NH, United States. Accepted.

- **2023-03**: T. Reiker, P. Phanse, N. F. Kleimeier, Z. Liu, A. J. Urban, D. Zhang, H. Zacharias "Time Resolved Photoelectron Spectroscopy of Thiophen based Conjugated Donor Acceptor Polymers for Organic Photovoltaic" Spring Transactions of the German Physical Society, Condensed Matter Section. Dresden, Germany.

- **2022-12**: A. Urban, H. M. Yamamoto "Metalloporphyrins open up towards enantioseparable and fully sp^2-hybridized helical complexes"

775^{th} Wilhelm and Else Heraeus Seminar of the German Physical Society. Bad Honnef, Germany.

Appendix C

Supplementary Figures and Data

C.1 List of Chemicals, Vendors and Purities

Table C.1: List of chemicals used in this work, along with purities and suppliers.

Chemical	Supplier	Purity
Acetic acid	Wako	>99.7 %
Acetone	Kanto	>99.5 %
Ascorbic acid	Wako	>99.6 %
Benzaldehyde	Sigma Aldrich	>99 %
Chloroform	Kanto	>99.0 %
Citric acid	Commercial	Household grade
Copper(II) acetate tetrahydrate	Wako	n/A
Dichloromethane	Kanto	>99.0 %
Dimethylformamide	Wako	99.5 %
Hydrochloric acid	Kanto	37 %
Iron(II) chloride	Wako	99.9 %
Magnesium perchlorate	Sigma Aldrich	ACS Reagent
Magnesium sulfate, anhydrous	Sigma Aldrich	≥99.5 %
Methyl *tert*-butyl ether	Kanto	99.0 %
Nickel(II) acetate tetrahydrate	Wako	n/A
Octaethylporphyrin	TCI	>95 %
Propionic acid	Wako	n/A
Pyridine	Wako	>99.0 %
Pyrrole	Sigma Aldrich	98 %
Silica, neutral, 60N	Kanto	n/A
Tetrabutylammonium perchlorate	TCI	≥98 %
Toluene	Kanto	>99.5 %

C.2 EI-MS Spectra

C.2.1 Ni(TPBT)

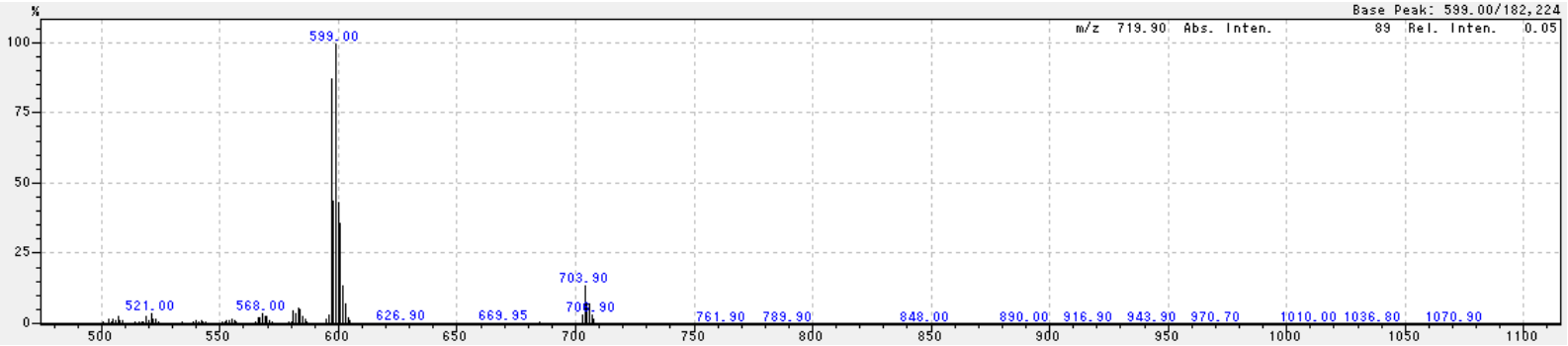

Figure C.1: EI-MS spectrum of Ni(TPBT).

C.2.2 Cu(TPBT)

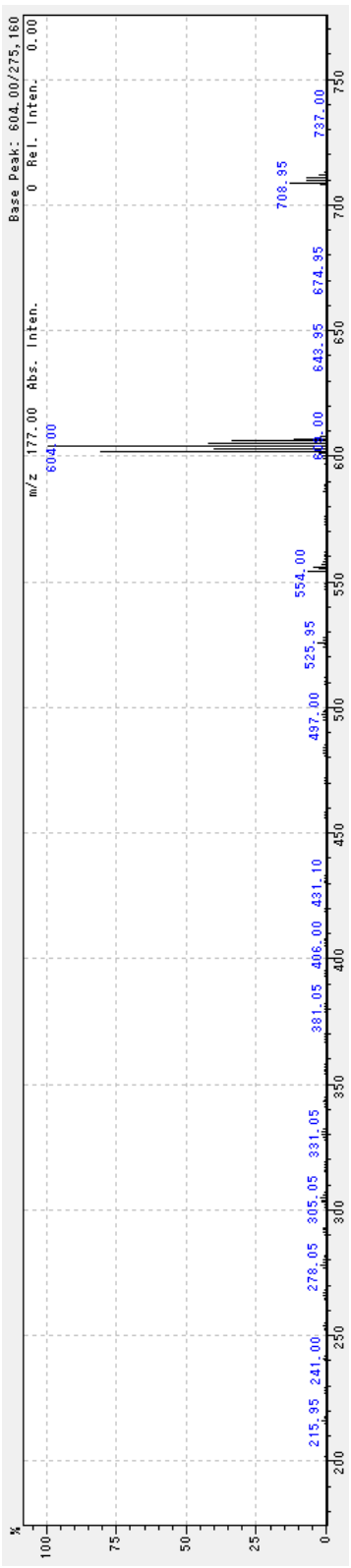

Figure C.2: EI-MS spectrum of Cu(TPBT).

C.2.3 H_3TPBV

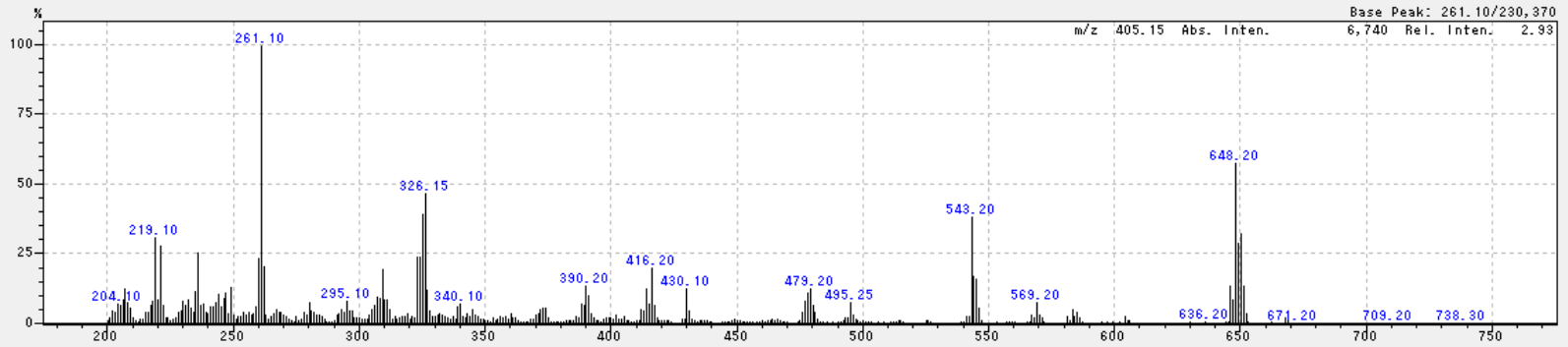

Figure C.3: EI-MS spectrum of H_3TPBV.

C.2.4 Ni(OEFB)

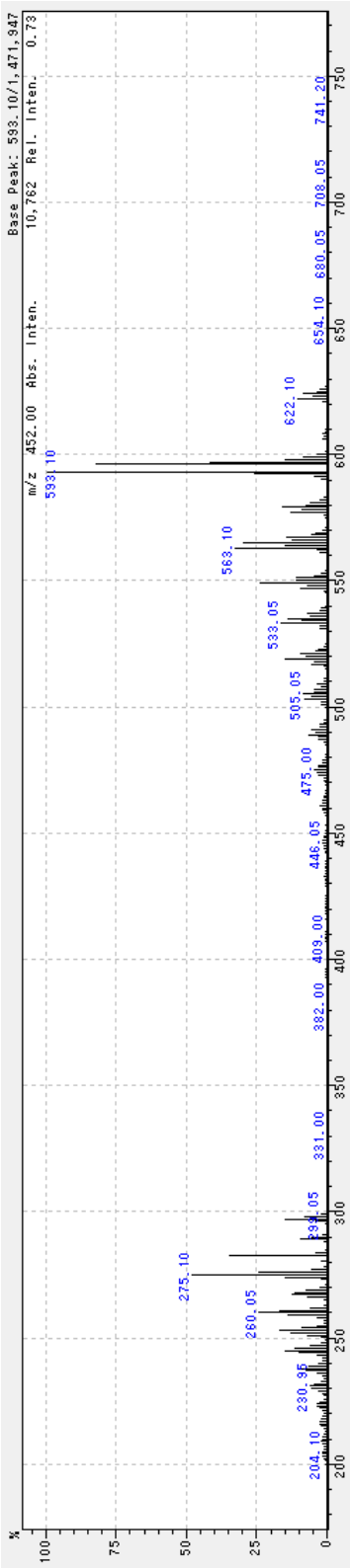

Figure C.4: EI-MS spectrum of Ni(OEFB).

C.2.5 Ni(OEFB) hydrate

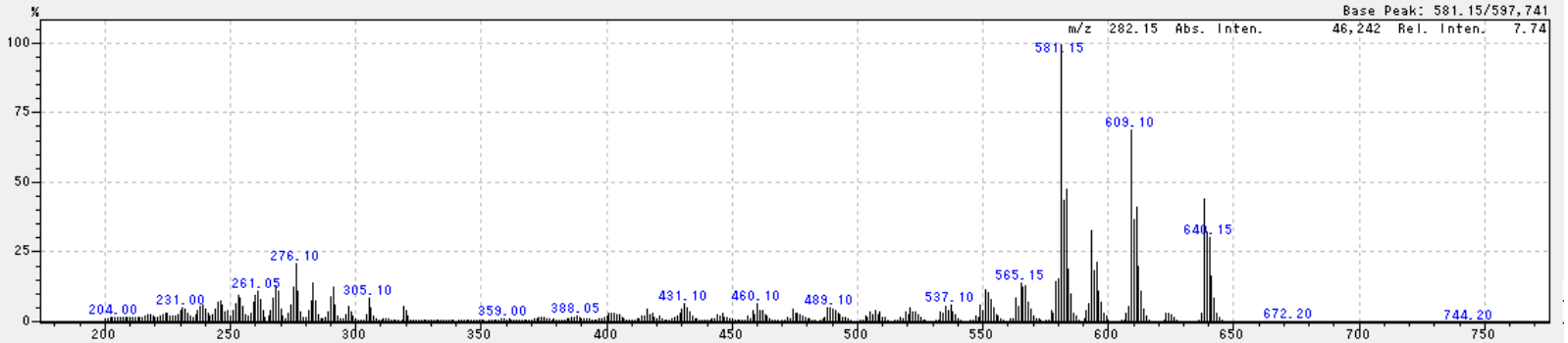

Figure C.5: EI-MS spectrum of the covalent hydrate of Ni(OEFB).

C.2.6 Mg(TPP) · 2 py

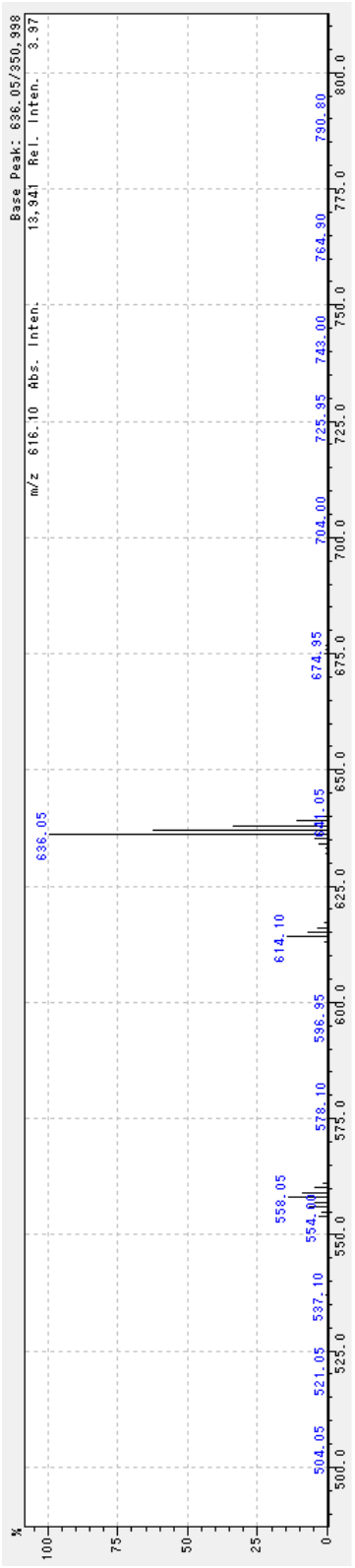

Figure C.6: EI-MS spectrum of Mg(TPP) · 2 py.

C.2.7 Mg(OEP) · 2 py

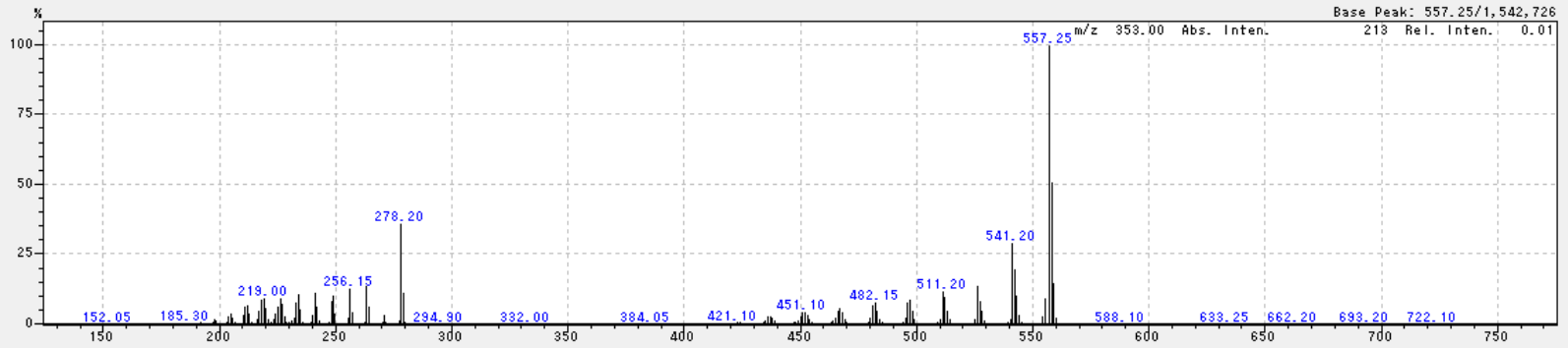

Figure C.7: EI-MS spectrum of Mg(OEP) · 2 py.

C.3 IR Spectrum of Ni(TPBT)

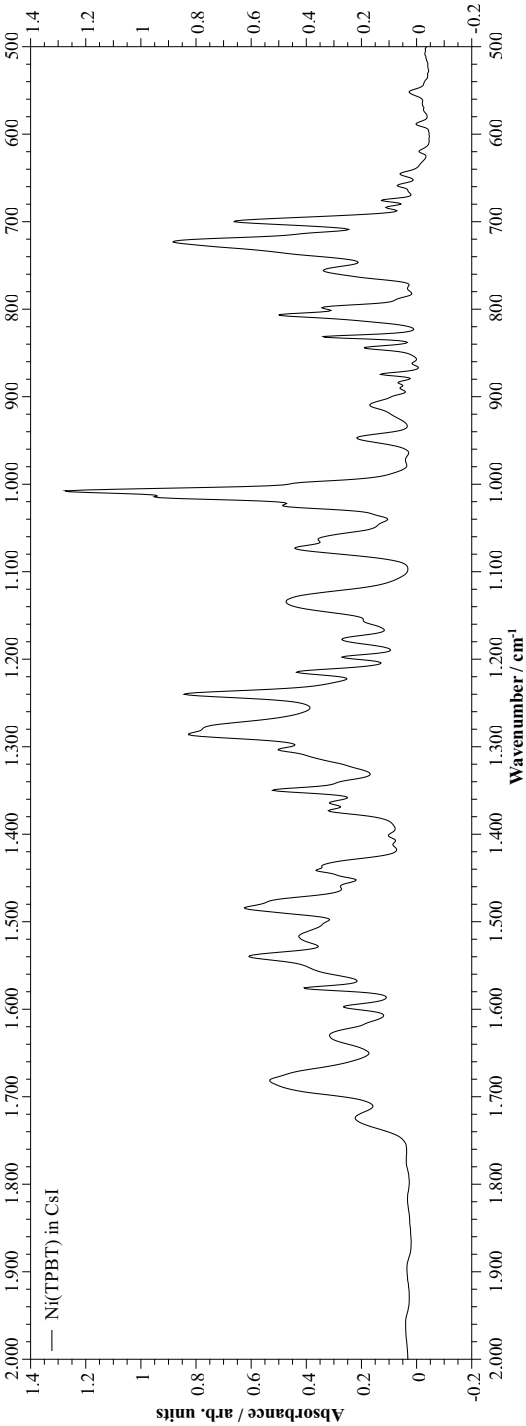

Figure C.8: IR spectrum of Ni(TPBT) as a CsI pellet.

C.4 ESR Peak Fitting of Cu(TPBT)

Table C.2: Fit parameters of the peaks in Figure 4.6 for a Levenberg-Marquardt algorithm using a tolerance of 0.0001. Fitted as $y = y_0 + (2A/\pi) \cdot w/[4 \cdot (x - x_c)^2 + w^2]$.

Fit paramater	Metal	Ligand
Range / Gs	$3301 - 3499$	$3550 - 3649$
A / [Gs · a.u.]	$1.1531 \cdot 10^9 \pm 2.9109 \cdot 10^6$	$3.6181 \cdot 10^8 \pm 9.7891 \cdot 10^5$
w / Gs	$2.3035 \cdot 10^2 \pm 6.9982 \cdot 10^{-1}$	$2.4572 \cdot 10^2 \pm 6.7162 \cdot 10^{-1}$
x_c / Gs	$3.3598 \cdot 10^3 \pm 1.7802 \cdot 10^{-1}$	$3.5703 \cdot 10^3 \pm 1.5334 \cdot 10^1$
R^2	0.99855	0.99961

C.5 NMR Spectra of Ni(TPBT)

C.5.1 ^{1}H NMR

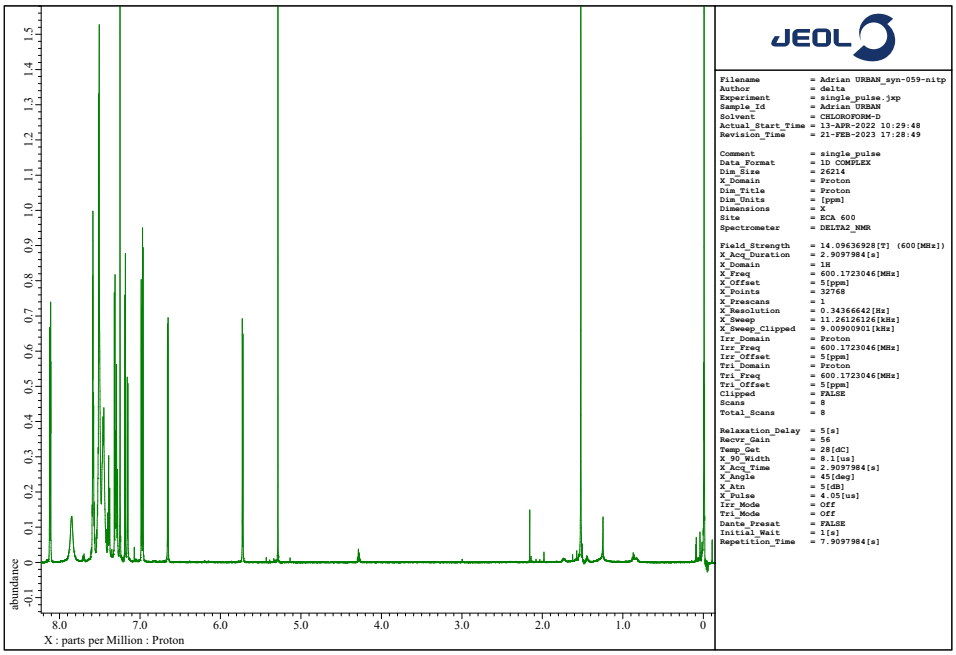

Figure C.9: Full ^{1}H-NMR spectrum of Ni(TPBT) in $CDCl_3$ at room temperature.

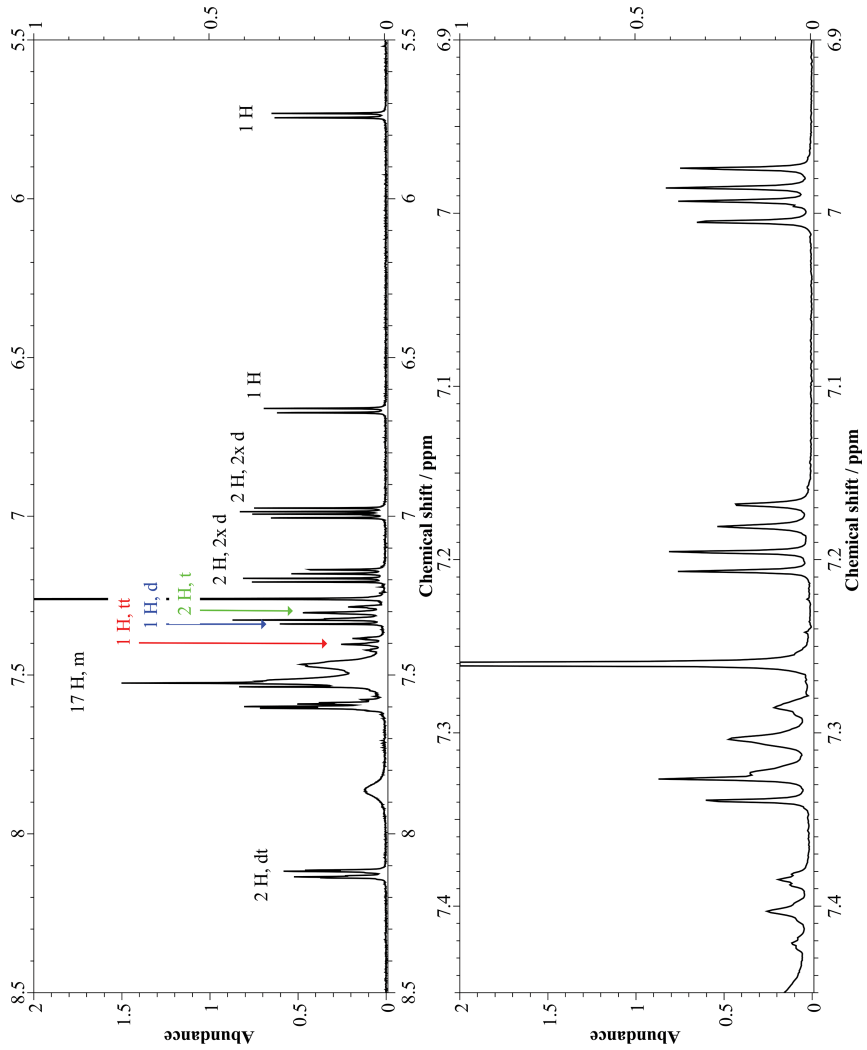

Figure C.10: ^{1}H-NMR in Figure C.9. Zoomed into the regions between 5.5 and 8.5 ppm.

C.5.2 ^{13}C

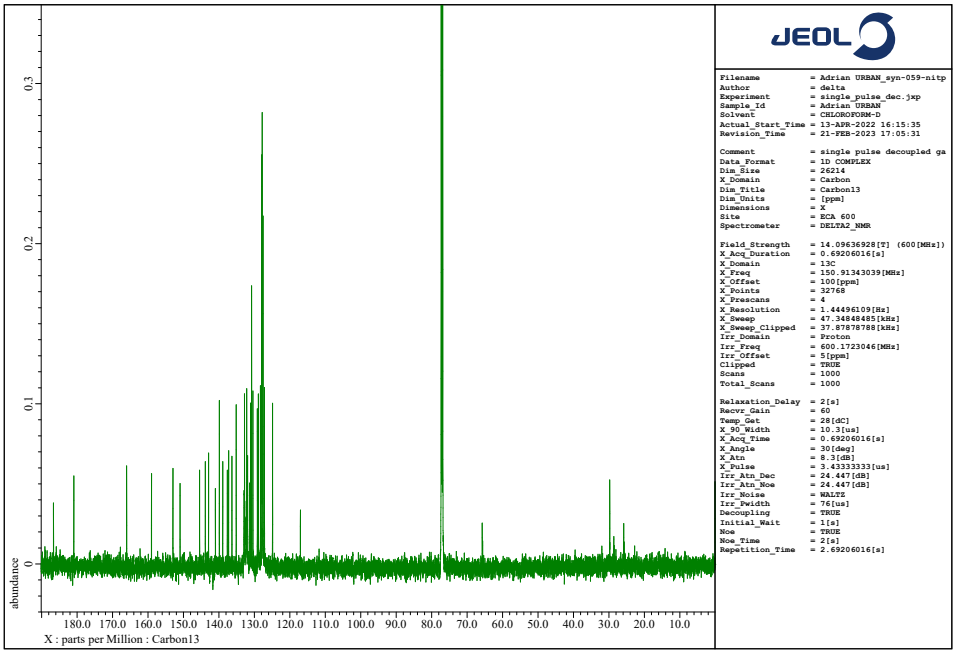

Figure C.11: ^{13}C NMR spectrum of Ni(TPBT) in $CDCl_3$ at room temperature.

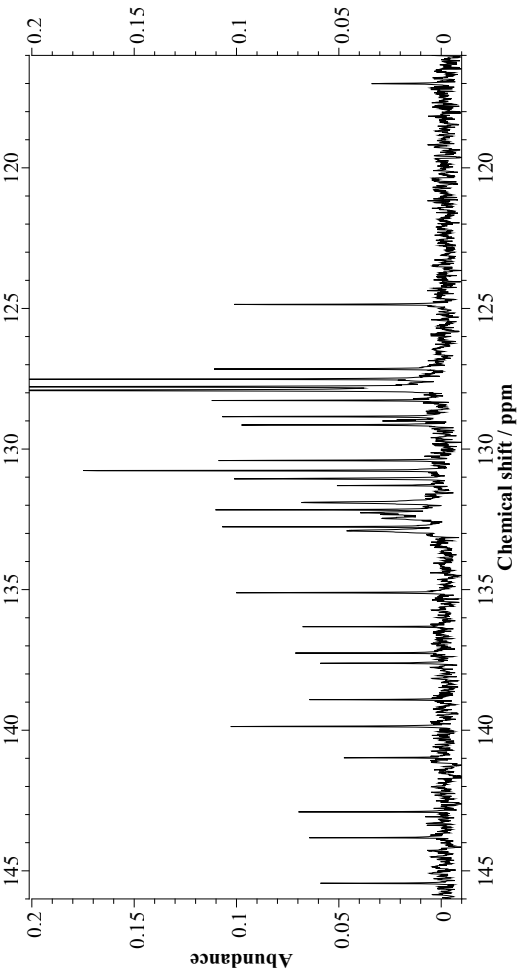

Figure C.12: ^{13}C-NMR in Figure C.11. Zoomed into the regions between 146 and 116 ppm.

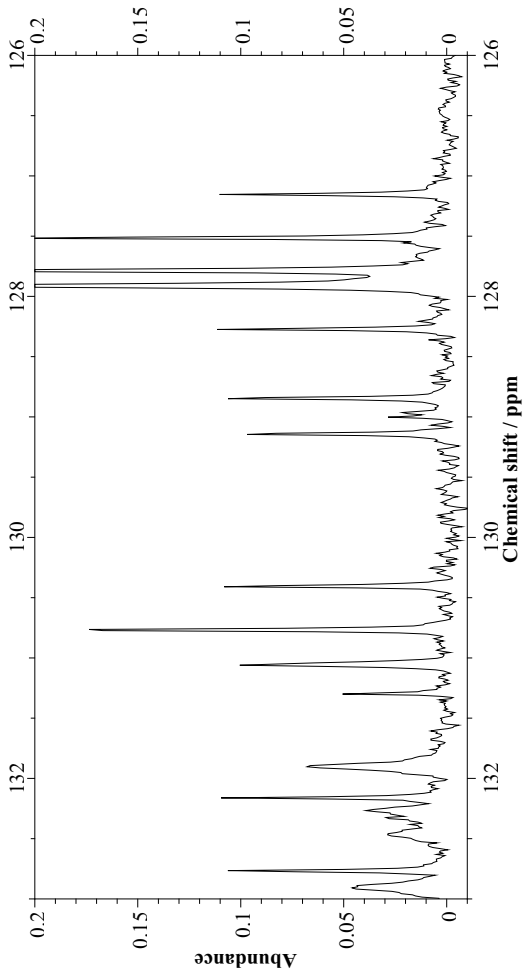

Figure C.13: ^{13}C-NMR in Figure C.11. Zoomed into the regions between 126 and 134 ppm.

C.5.3 ^{1}H,^{1}H-NOESY

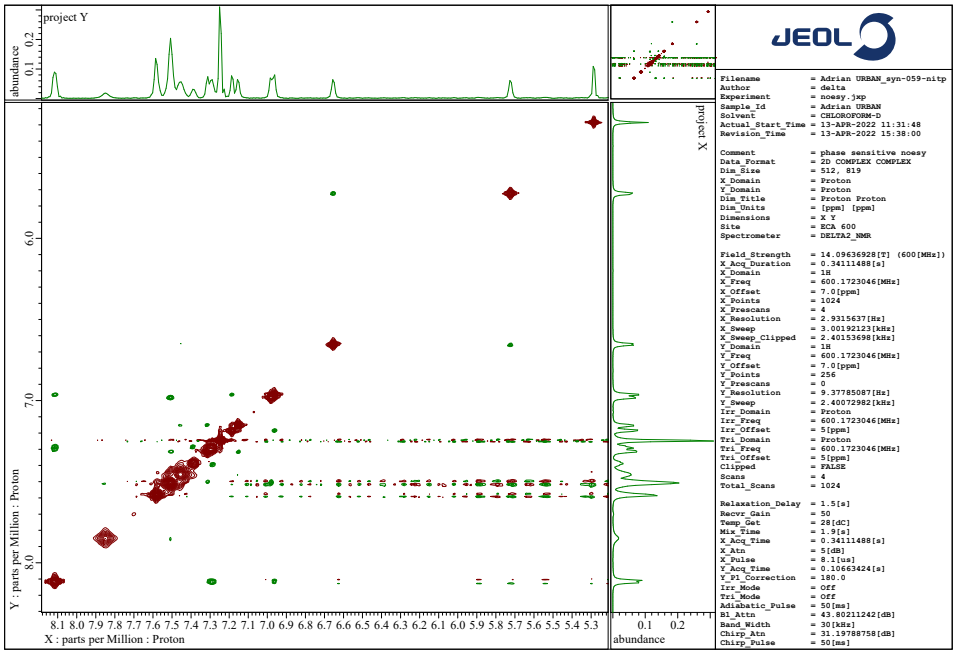

Figure C.14: ^{1}H,^{1}H-NOESY spectrum of Ni(TPBT) in $CDCl_3$ at room temperature.

C.5.4 HMQC

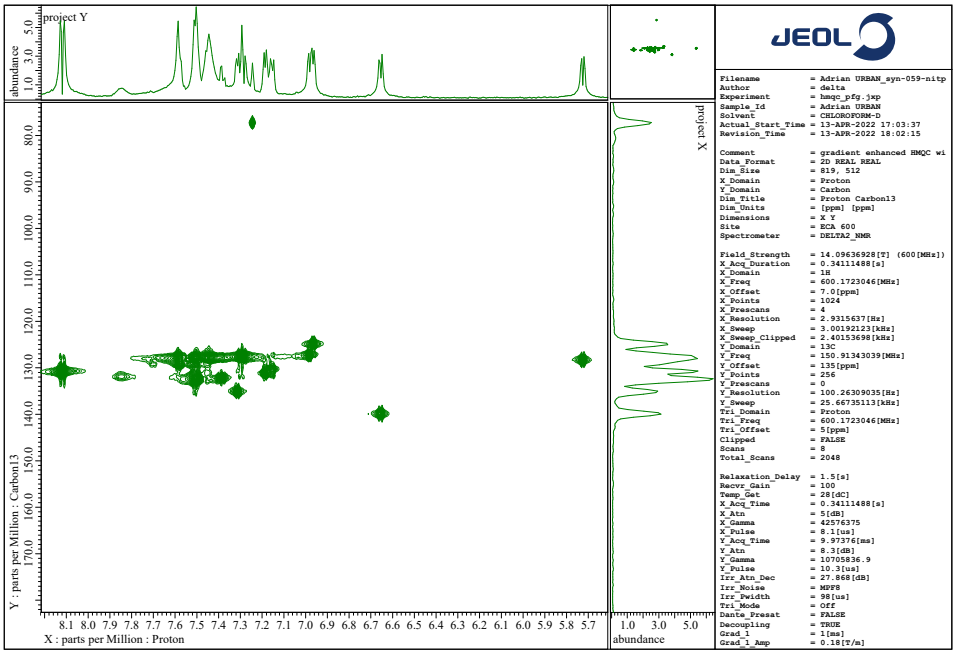

Figure C.15: HMQC NMR spectrum of Ni(TPBT) in $CDCl_3$ at room temperature.

C.5.5 Proton Assignments

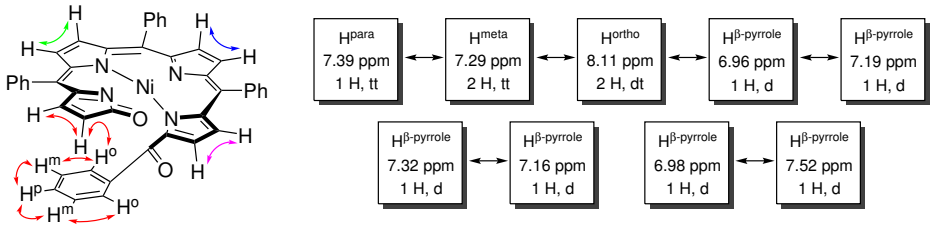

Figure C.16: Proton assignments in Ni(TPBT), based on the previously depicted NMR data.

C.6 NMR Spectra of *EZZZ*-H_3TPBV

C.6.1 ^{1}H NMR

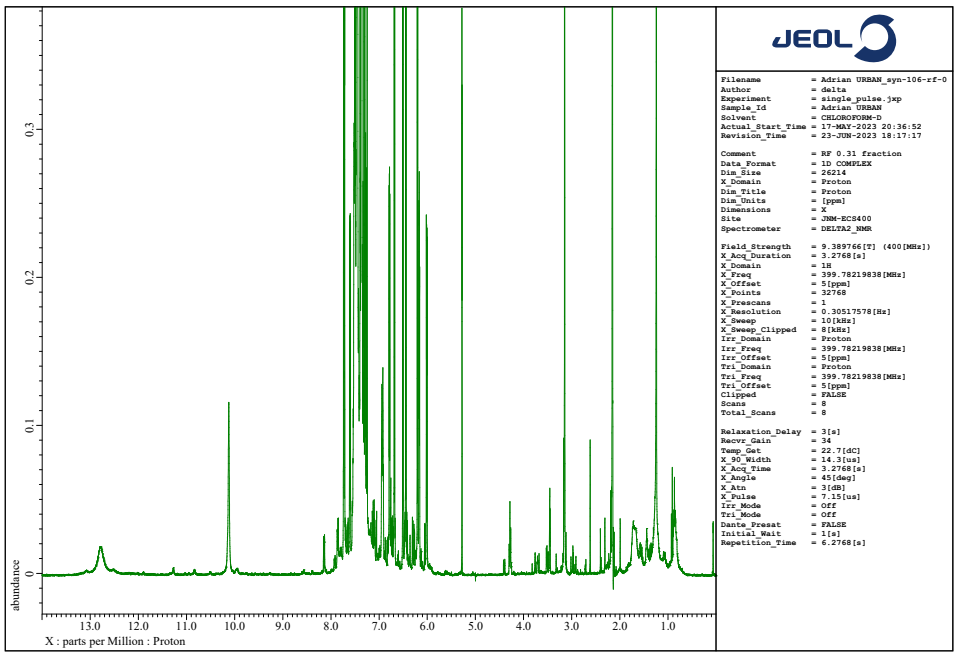

Figure C.17: Full ^{1}H-NMR spectrum of *EZZZ*-H_3TPBV in TMS-free $CDCl_3$.

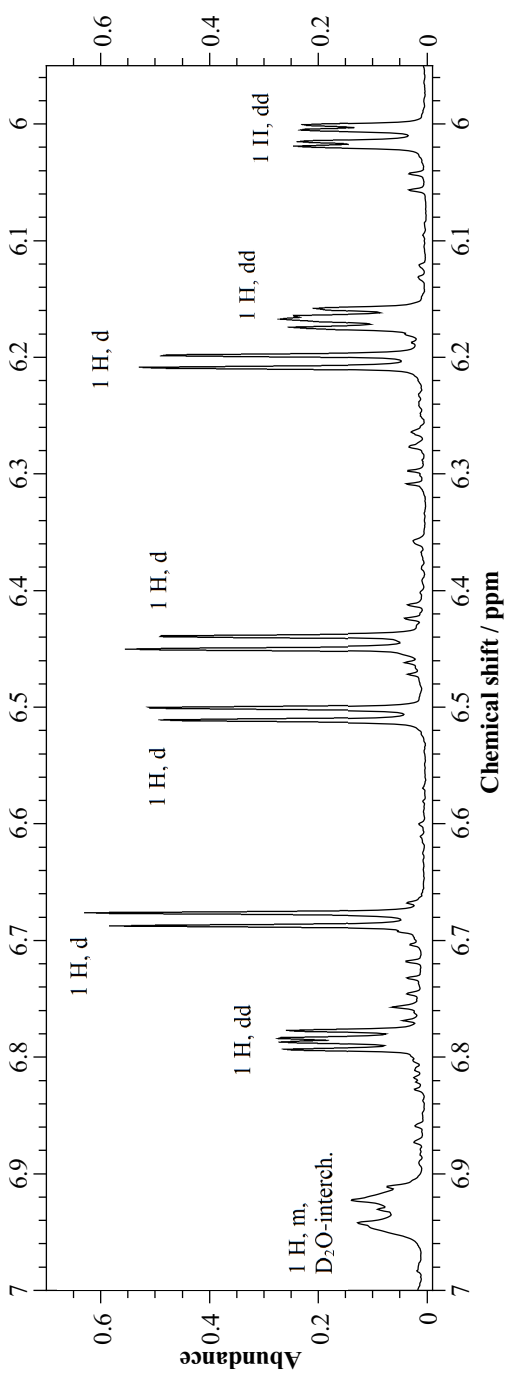

Figure C.18: ^{1}H-NMR spectrum of *EZZZ*-H_3TPBV in TMS-free $CDCl_3$ between 5.5 and 7.0 ppm.

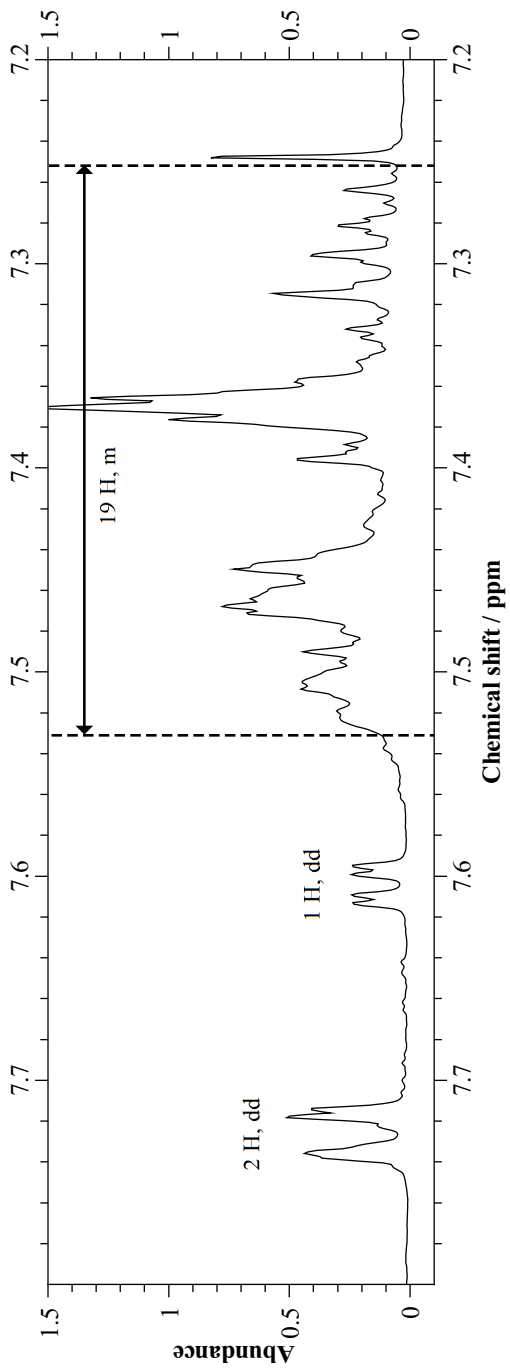

Figure C.19: ^{1}H-NMR spectrum of *EZZZ*-H_3TPBV in TMS-free $CDCl_3$ between 7.2 and 7.8 ppm.

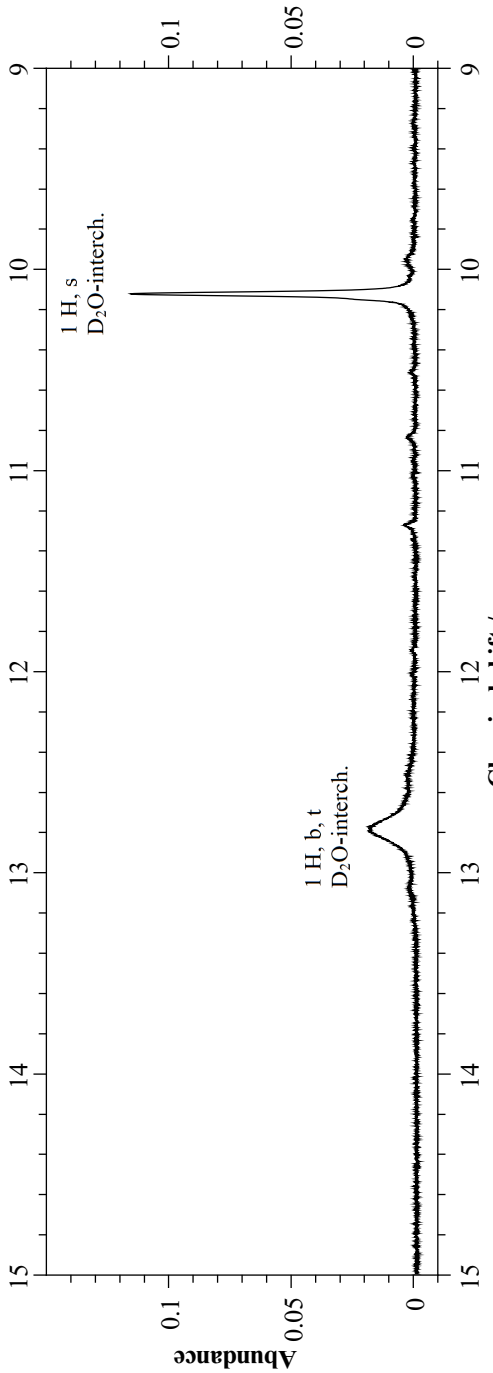

Figure C.20: ^{1}H-NMR spectrum of *EZZZ*-H_3TPBV in TMS-free $CDCl_3$ between 9.0 and 15.0 ppm.

C.6.2 ^{13}C NMR

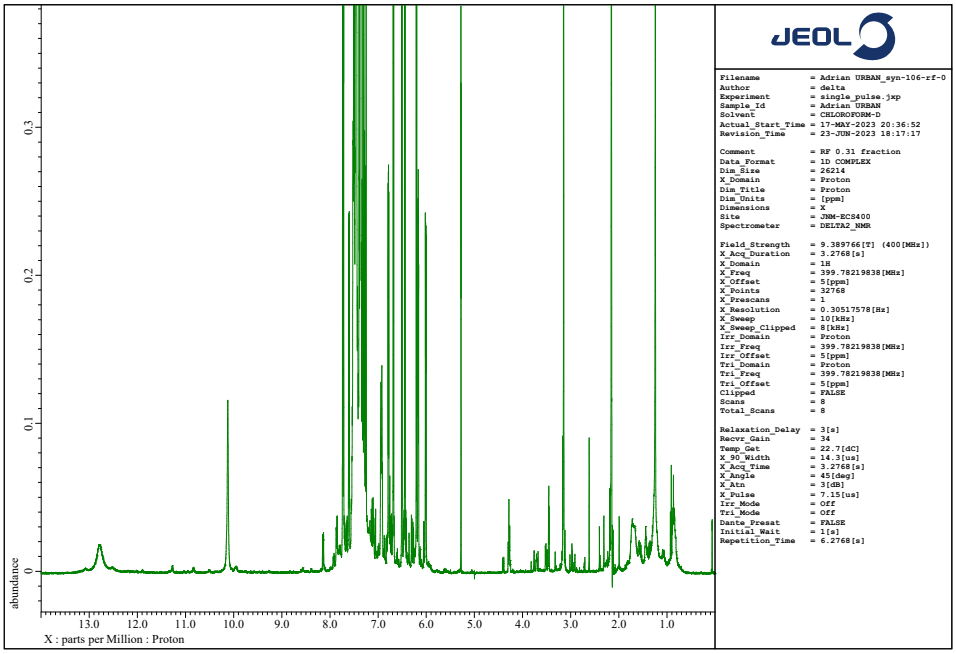

Figure C.21: Full ^{13}C-NMR spectrum of *EZZZ*-H_3TPBV in TMS-free $CDCl_3$.

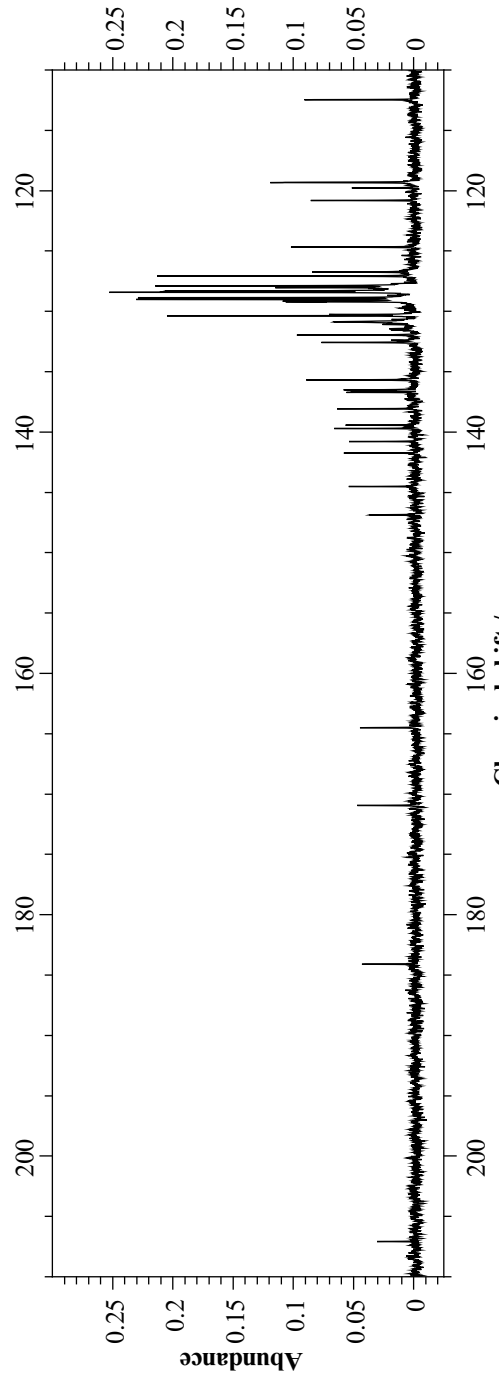

Figure C.22: ^{13}C-NMR spectrum of *EZZZ*-H_3TPBV in TMS-free $CDCl_3$ between 110 and 210 ppm.

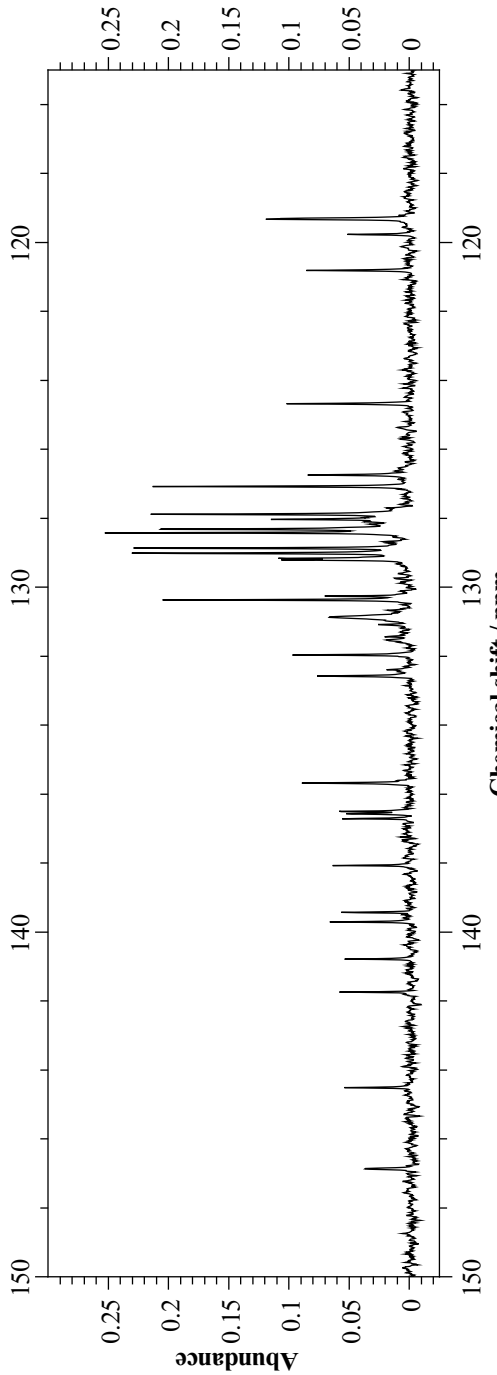

Figure C.23: ^{13}C-NMR spectrum of *EZZZ*-H_3TPBV in TMS-free $CDCl_3$ between 110 and 150 ppm.

C.6.3 ^{1}H,^{1}H-COSY

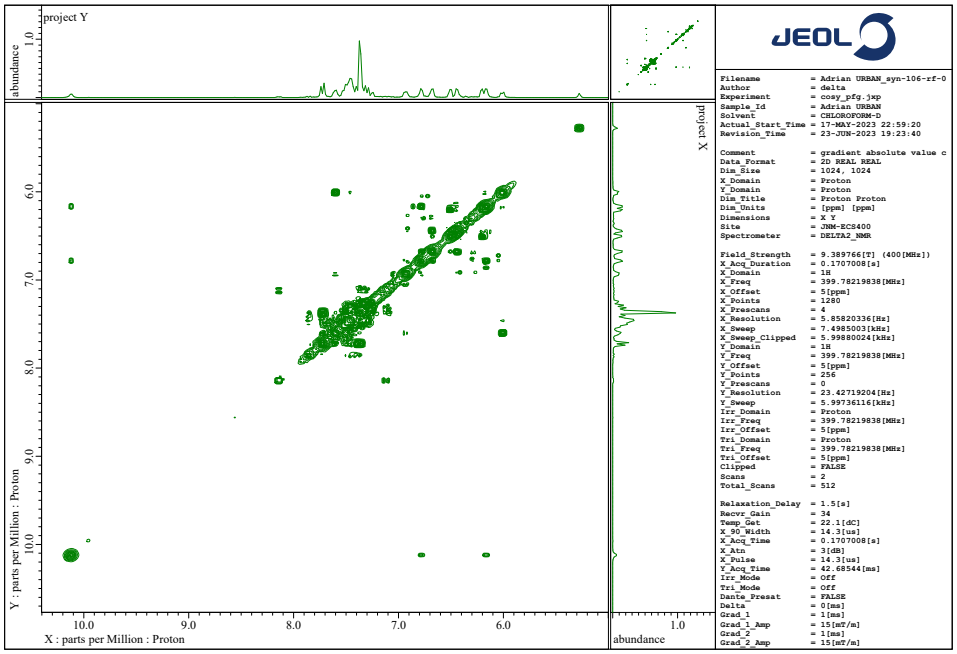

Figure C.24: ^{1}H,^{1}H-COSY spectrum of *EZZZ*-H_3TPBV in TMS-free $CDCl_3$ at room temperature.

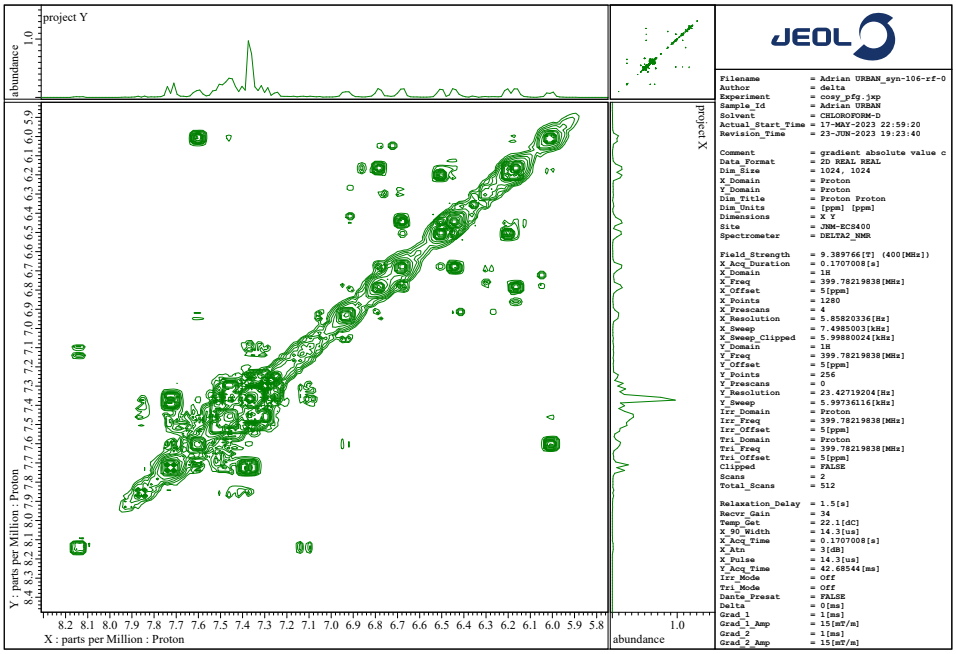

Figure C.25: The previous COSY spectrum, zoomed in.

C.6.4 HMQC

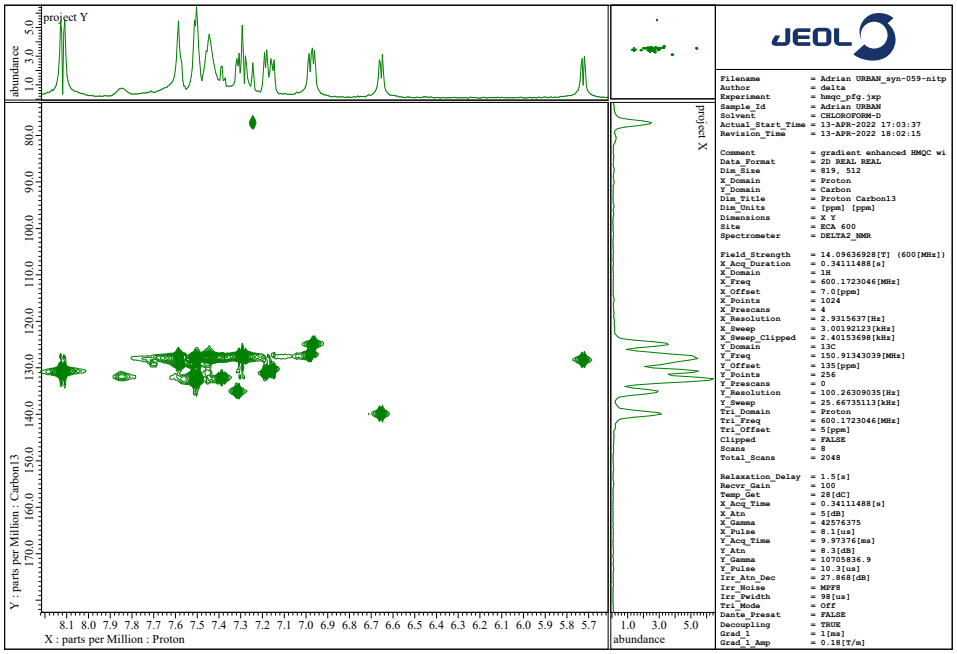

Figure C.26: HMQC NMR spectrum of *EZZZ*-H_3TPBV in TMS-free $CDCl_3$ at room temperature.

C.7 UV/vis Spectrum of H_3TPBV

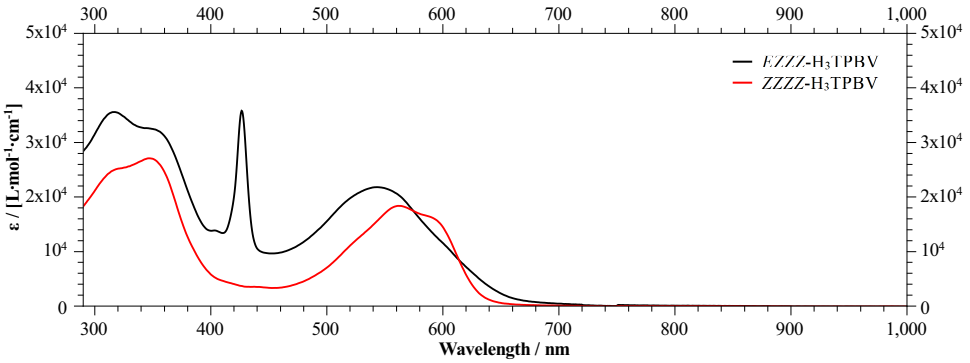

Figure C.27: UV/vis spectra of *EZZZ*- and *ZZZZ*-H_3TPBV as 10^{-5} mol/l solutions in $CHCl_3$.

C.8 Potential Energy Surface Scans

C.8.1 Ni(TPBT)

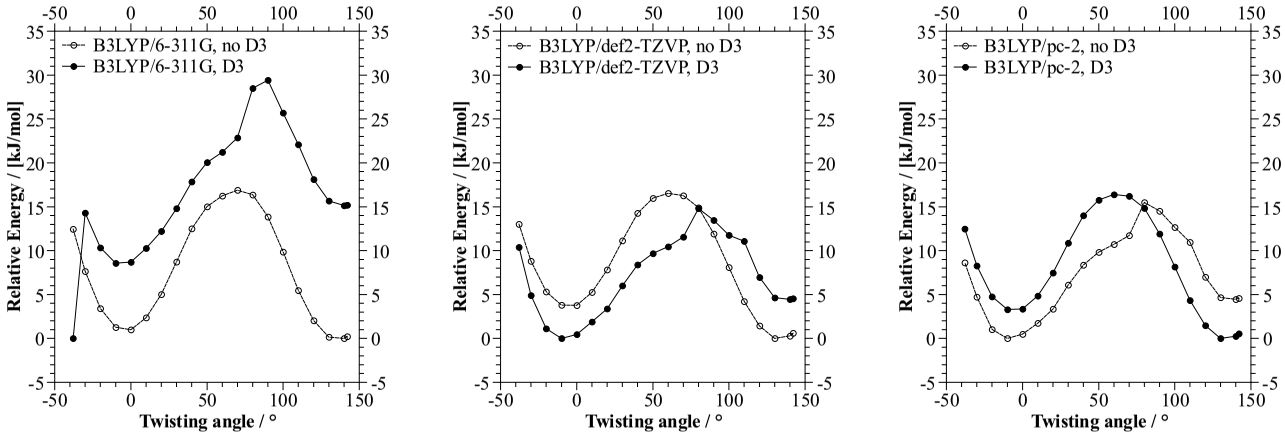

Figure C.28: PES scans of Ni(TPBT) using the B3LYP functional with and without D3 dispersion correction. Left: 6-311G basis. Center: def2-TZVP basis. Right pc-2 basis. Augmentations are mentioned in the "Computational Setup" section on page 29.

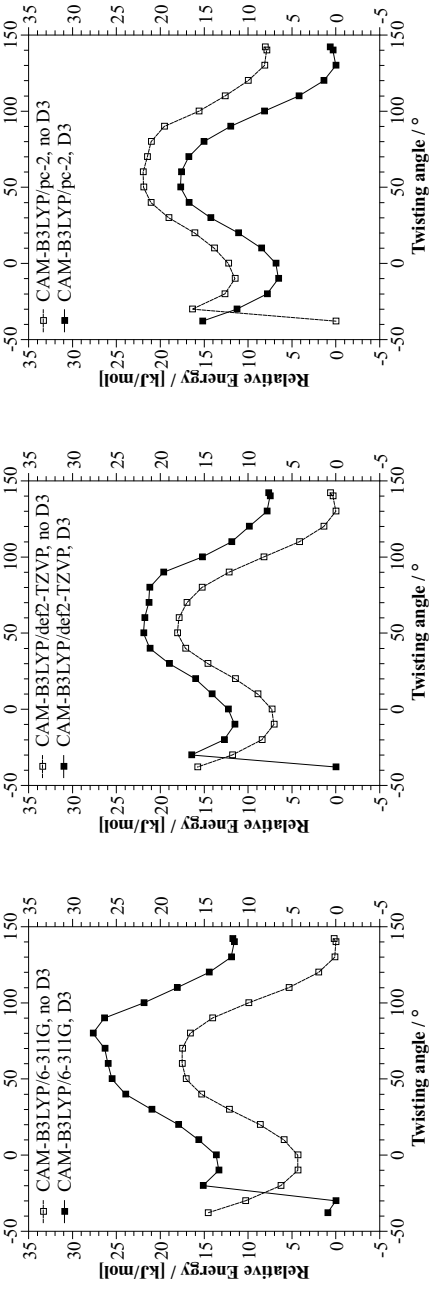

Figure C.29: PES scans of Ni(TPBT) using the CAM-B3LYP functional with and without D3 dispersion correction. Left: 6-311G basis. Center: def2-TZVP basis. Right pc-2 basis. Augmentations are mentioned in the "Computational Setup" section on page 29.

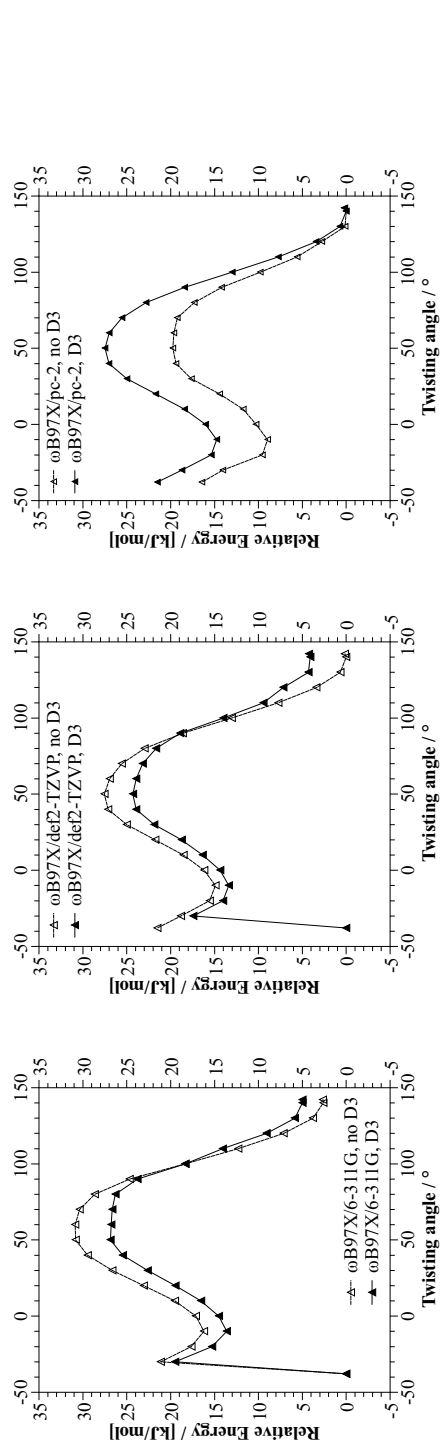

Figure C.30: PES scans of Ni(TPBT) using the ωB97X functional with and without D3 dispersion correction. Left: 6-311G basis. Center: def2-TZVP basis. Right pc-2 basis. Augmentations are mentioned in the "Computational Setup" section on page 29.

C.8.2 21,23*H*-TPBT

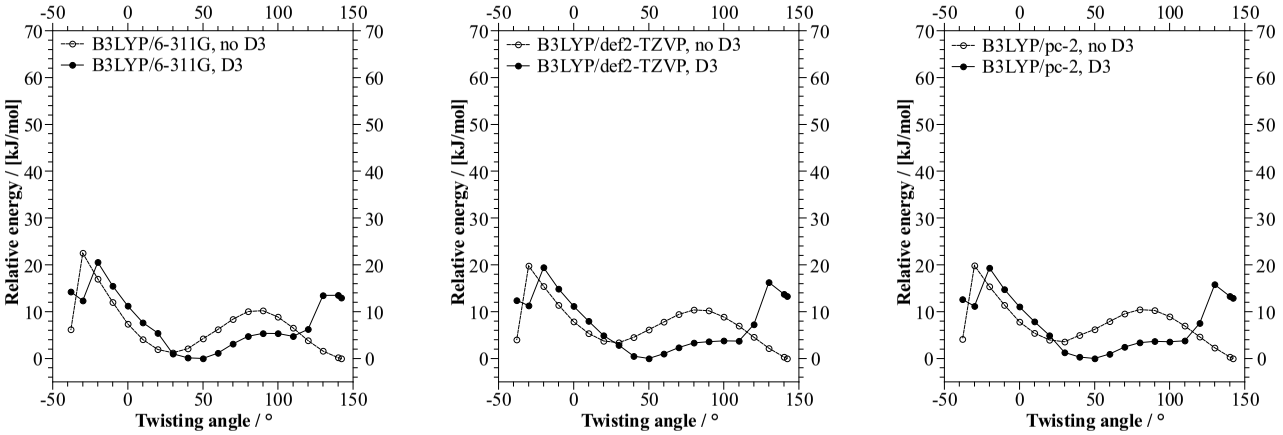

Figure C.31: PES scans of 21,23*H*-H_2TPBT using the B3LYP functional with and without D3 dispersion correction. Left: 6-311G basis. Center: def2-TZVP basis. Right pc-2 basis. Augmentations are mentioned in the "Computational Setup" section on page 29.

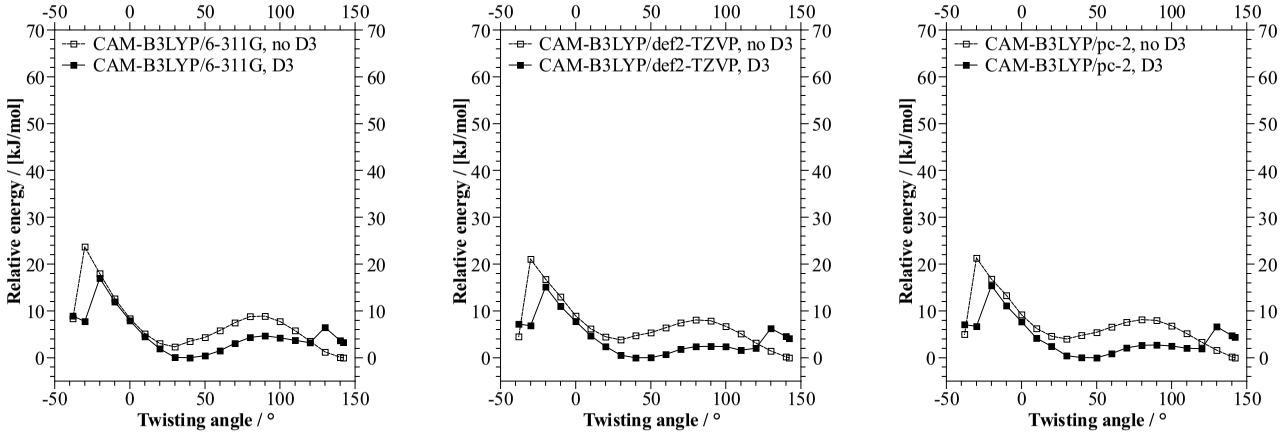

Figure C.32: PES scans of 21,23*H*-H_2TPBT using the CAM-B3LYP functional with and without D3 dispersion correction. Left: 6-311G basis. Center: def2-TZVP basis. Right pc-2 basis. Augmentations are mentioned in the "Computational Setup" section on page 29.

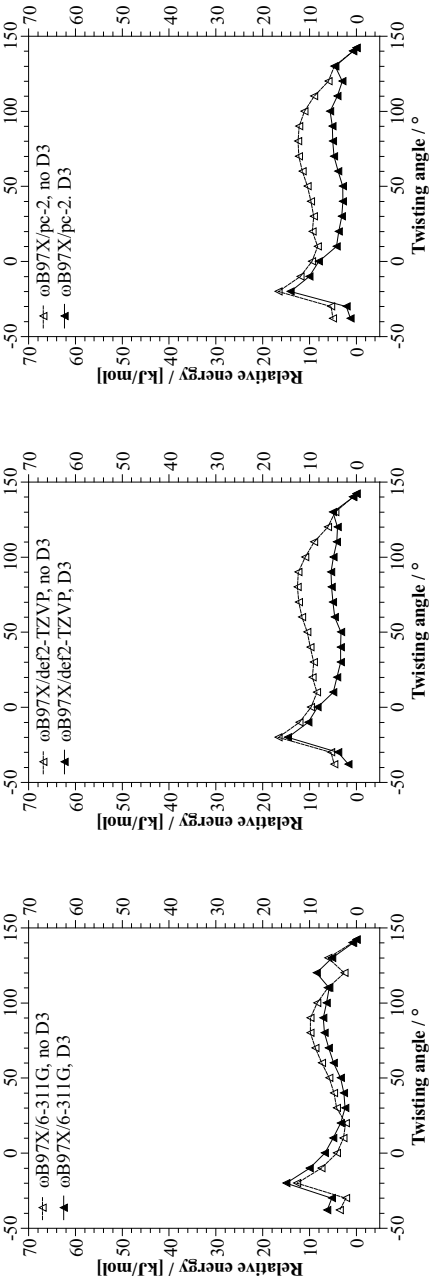

Figure C.33: PES scans of 21,23*H*-H_2TPBT using the ωB97X functional with and without D3 dispersion correction. Left: 6-311G basis. Center: def2-TZVP basis. Right pc-2 basis. Augmentations are mentioned in the "Computational Setup" section on page 29.

C.8.3 22,24*H*-TPBT

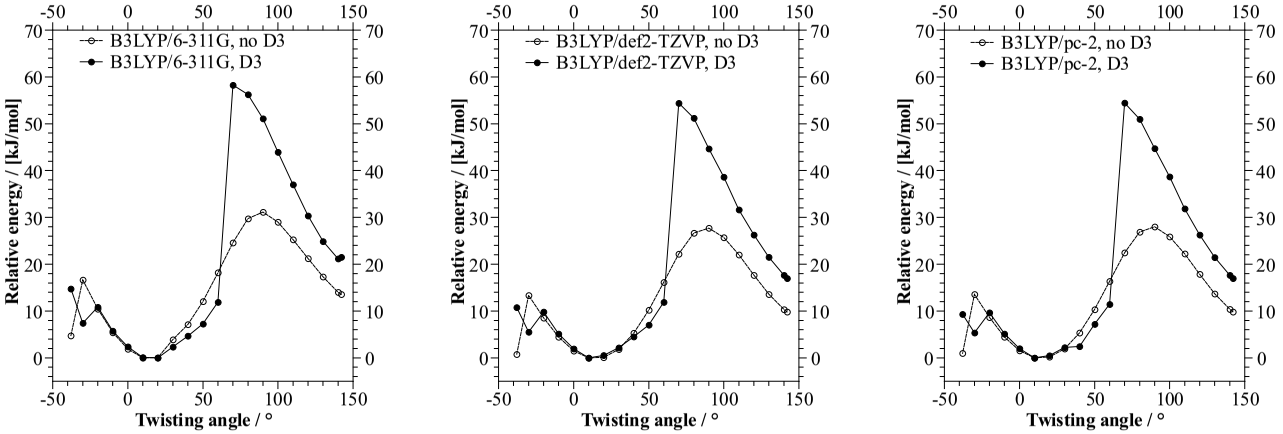

Figure C.34: PES scans of 22,24*H*-H_2TPBT using the B3LYP functional with and without D3 dispersion correction. Left: 6-311G basis. Center: def2-TZVP basis. Right pc-2 basis. Augmentations are mentioned in the "Computational Setup" section on page 29.

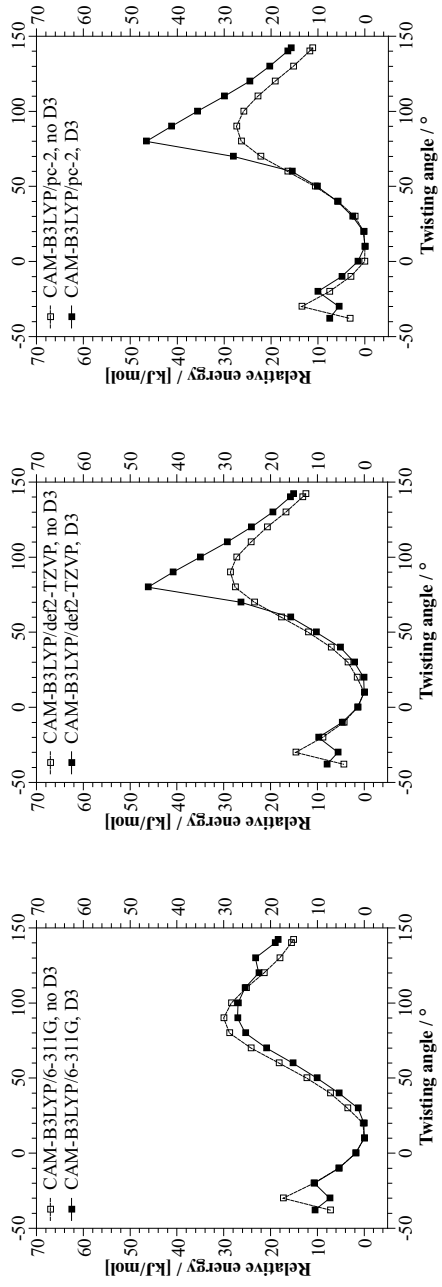

Figure C.35: PES scans of 22,24*H*-H_2TPBT using the CAM-B3LYP functional with and without D3 dispersion correction. Left: 6-311G basis. Center: def2-TZVP basis. Right pc-2 basis. Augmentations are mentioned in the "Computational Setup" section on page 29.

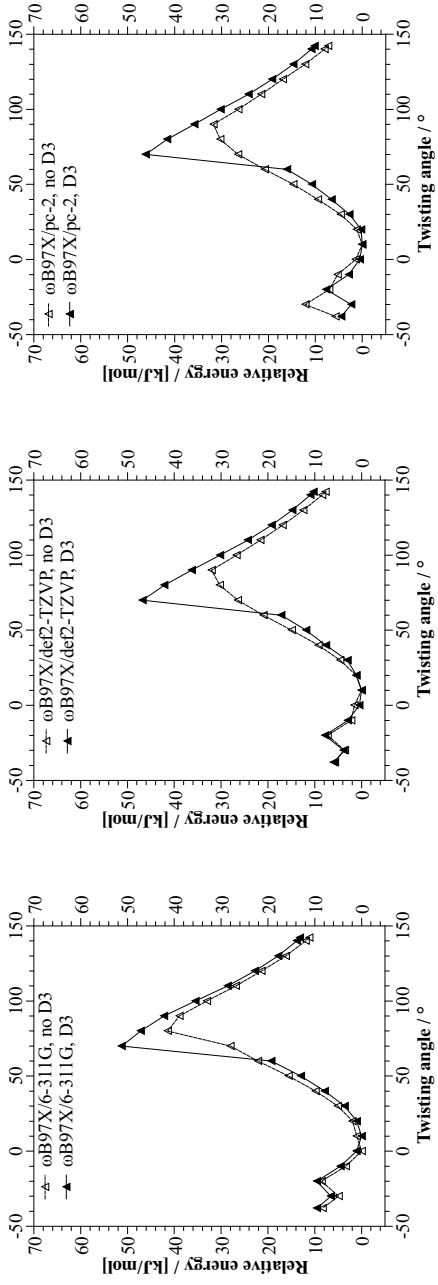

Figure C.36: PES scans of 22,24*H*-H_2TPBT using the ωB97X functional with and without D3 dispersion correction. Left: 6-311G basis. Center: def2-TZVP basis. Right pc-2 basis. Augmentations are mentioned in the "Computational Setup" section on page 29.

C.9 Frontier Orbitals

C.9.1 Ni(TPBT)

LUMO+0

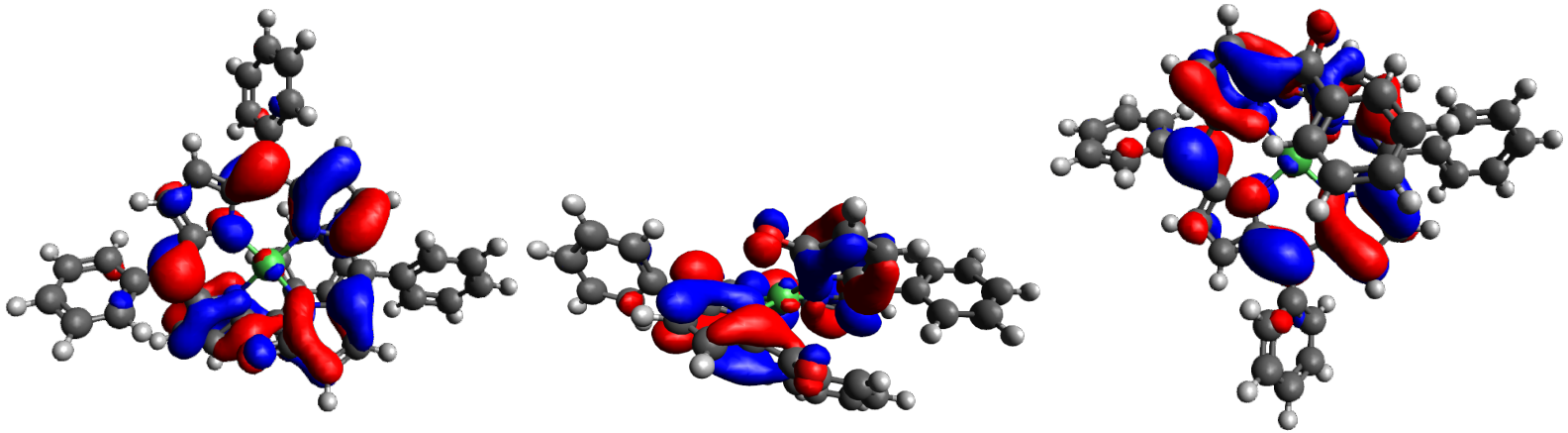

Figure C.37: Frontier orbitals of Ni(TPBT), obtained via calculation with the ωB97X-D3 functional and the def2-TZVP basis set. Augmentations are mentioned on page 29. Shown is LUMO+0 (MO 182) at -0.06639 Eh (-1.80676 eV)

HOMO-0

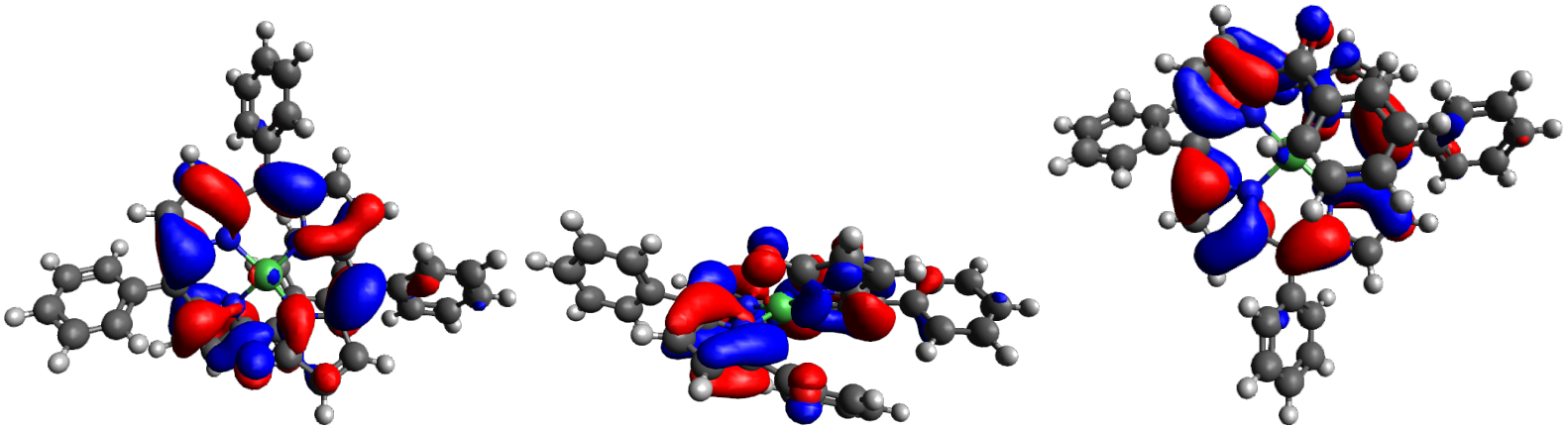

Figure C.38: Frontier orbitals of Ni(TPBT), obtained via calculation with the ωB97X-D3 functional and the def2-TZVP basis set. Augmentations are mentioned on page 29. Shown is HOMO-0 (MO 181) at -0.25632 Eh (-6.97560 eV)

HOMO-2

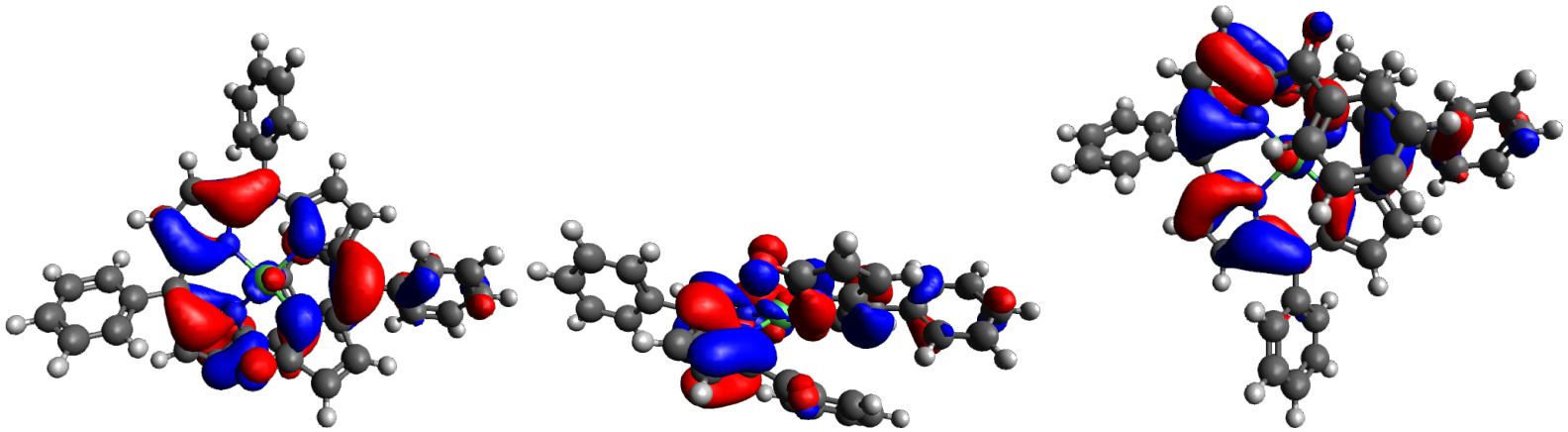

Figure C.39: Frontier orbitals of Ni(TPBT), obtained via calculation with the ωB97X-D3 functional and the def2-TZVP basis set. Augmentations are mentioned on page 29. Shown is HOMO-2 (MO 180) at -0.28914 Eh (-7.86877 eV)

HOMO-3

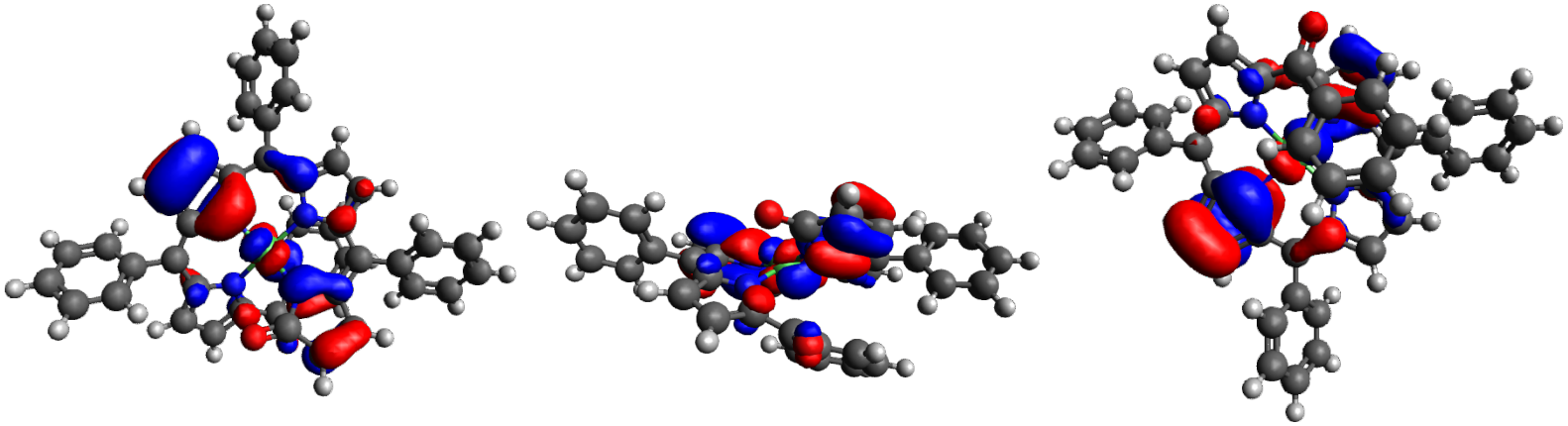

Figure C.40: Frontier orbitals of Ni(TPBT), obtained via calculation with the ωB97X-D3 functional and the def2-TZVP basis set. Augmentations are mentioned on page 29. Shown is HOMO-3 (MO 179) at -0.31601 Eh (-8.6000 eV)

HOMO-4

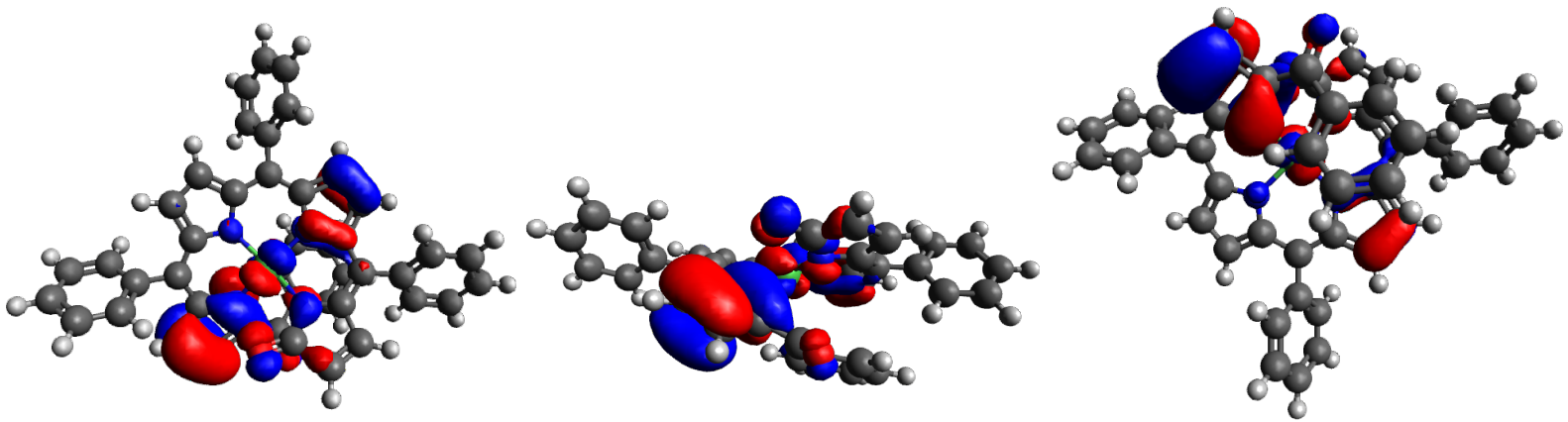

Figure C.41: Frontier orbitals of Ni(TPBT), obtained via calculation with the ωB97X-D3 functional and the def2-TZVP basis set. Augmentations are mentioned on page 29. Shown is HOMO-4 (MO 178) at -0.31858 Eh (-8.6700 eV)

C.9.2 Truncated Ni(TPBT)

LUMO+1

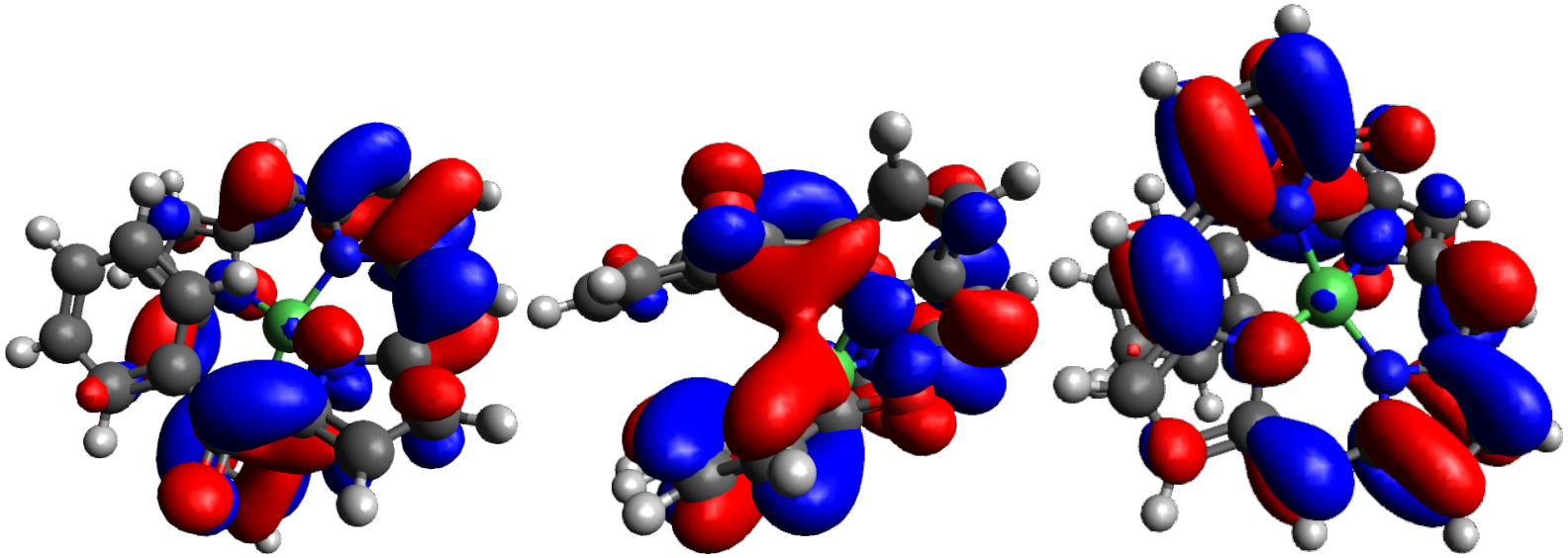

Figure C.42: Frontier orbitals of truncated Ni(TPBT), obtained via calculation with the B2PLYP functional and the def2-TZVP basis set. Augmenta-tions are mentioned on page 29. Shown is LUMO+1 (MO 118) at -0.04152 Eh (-1.2199 eV)

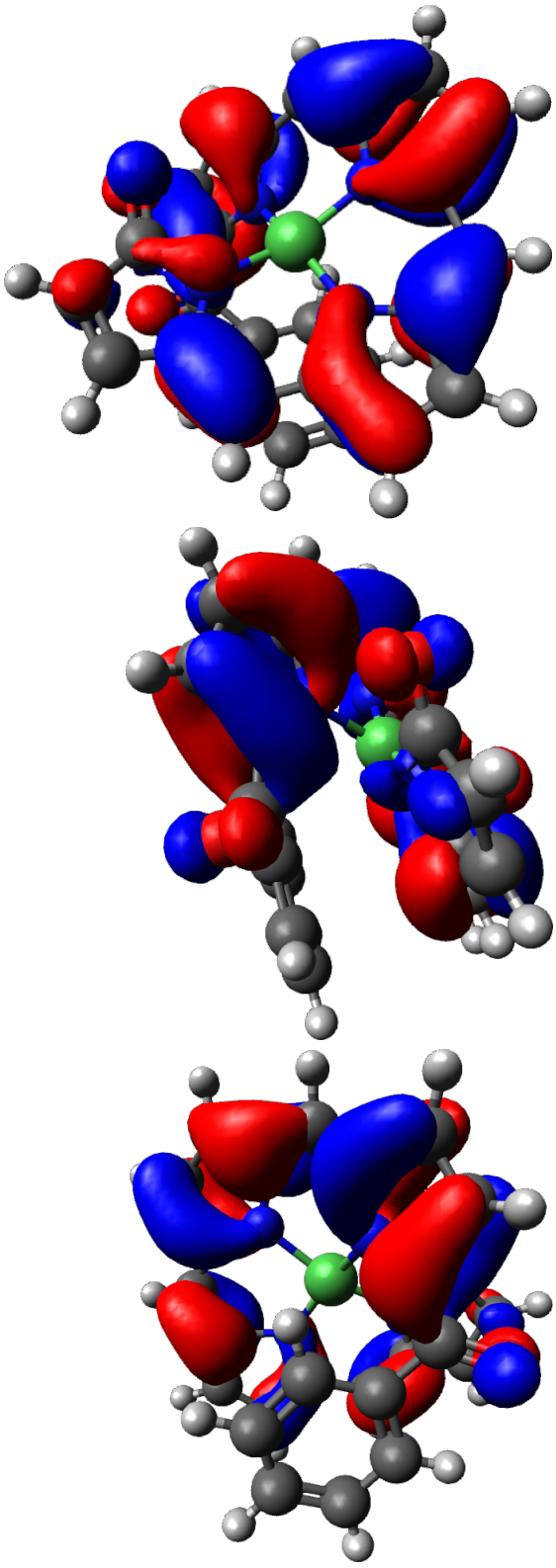

LUMO+0

Figure C.43: Frontier orbitals of truncated Ni(TPBT), obtained via calculation with the B2PLYP functional and the def2-TZVP basis set. Augmenta-tions are mentioned on page 29. Shown is LUMO+0 (MO 117) at -0.08872 Eh (-2.4142 eV)

HOMO-0

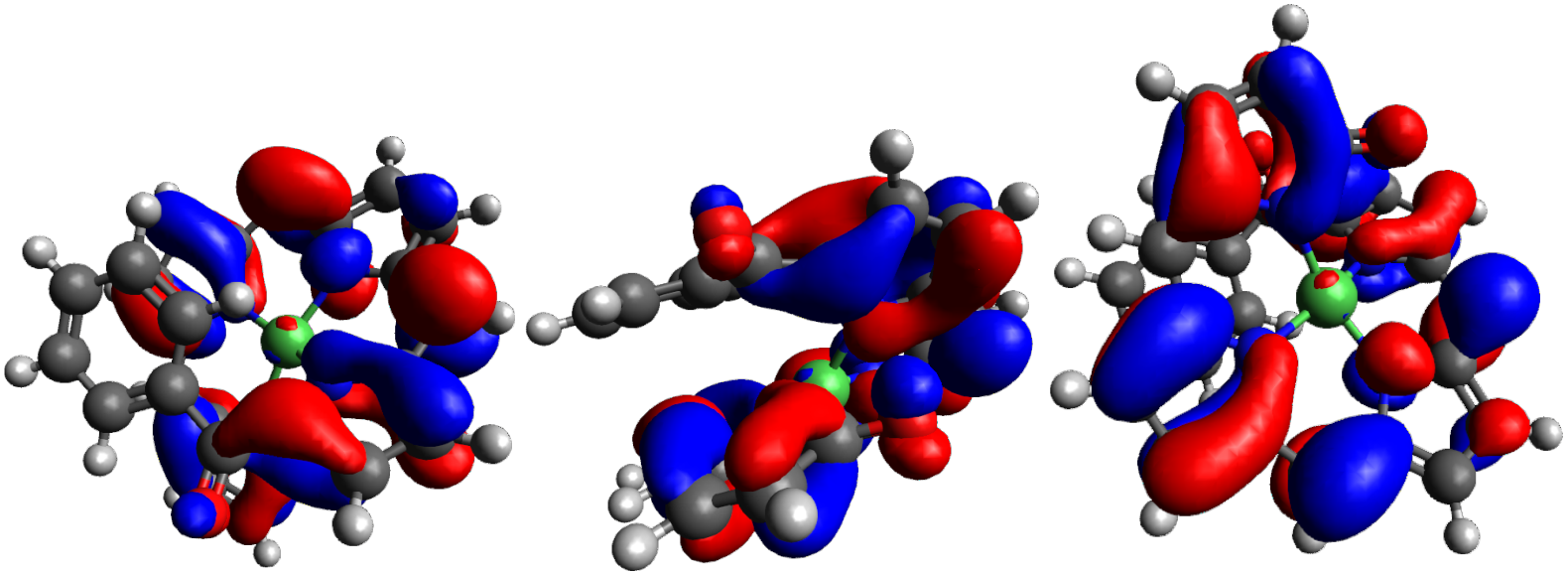

Figure C.44: Frontier orbitals of truncated Ni(TPBT), obtained via calculation with the B2PLYP functional and the def2-TZVP basis set. Augmenta-tions are mentioned on page 29. Shown is HOMO-0 (MO 116) at -0.22253 Eh (-6.0553 eV)

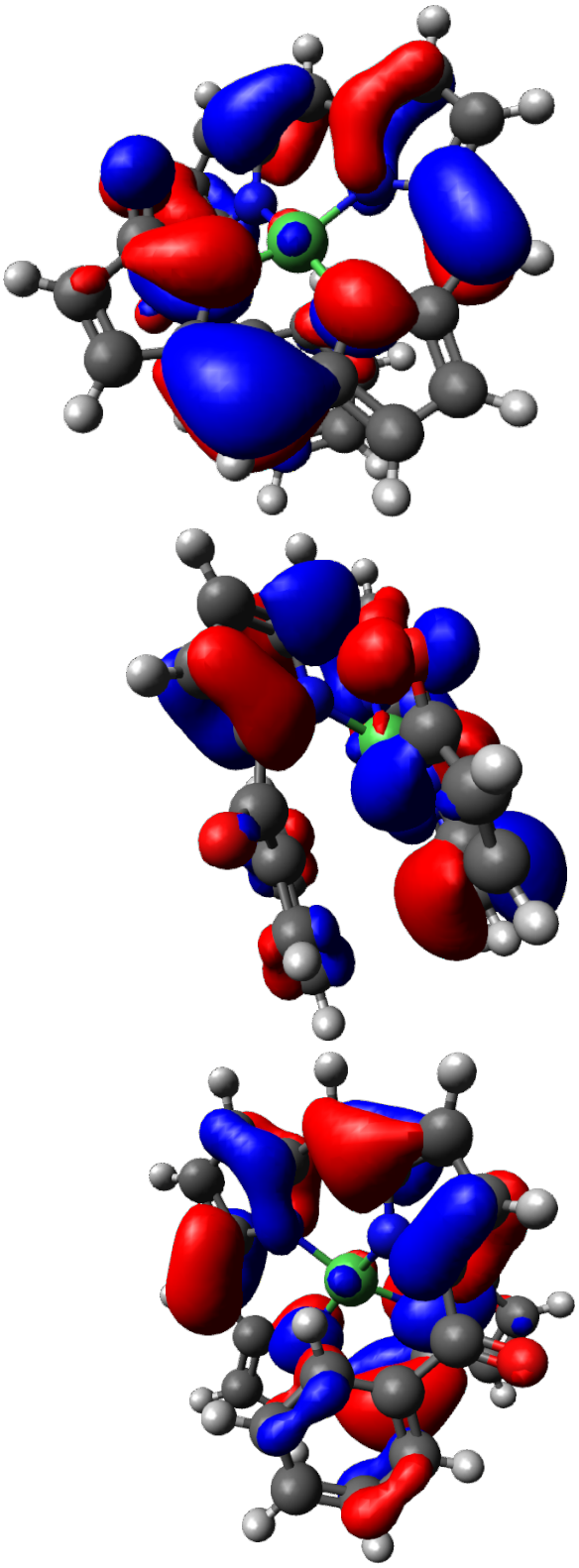

HOMO-1

Figure C.45: Frontier orbitals of truncated Ni(TPBT), obtained via calculation with the B2PLYP functional and the def2-TZVP basis set. Augmenta-tions are mentioned on page 29. Shown is HOMO-1 (MO 115) at -0.26242 Eh (-7.1408 eV)

HOMO-2

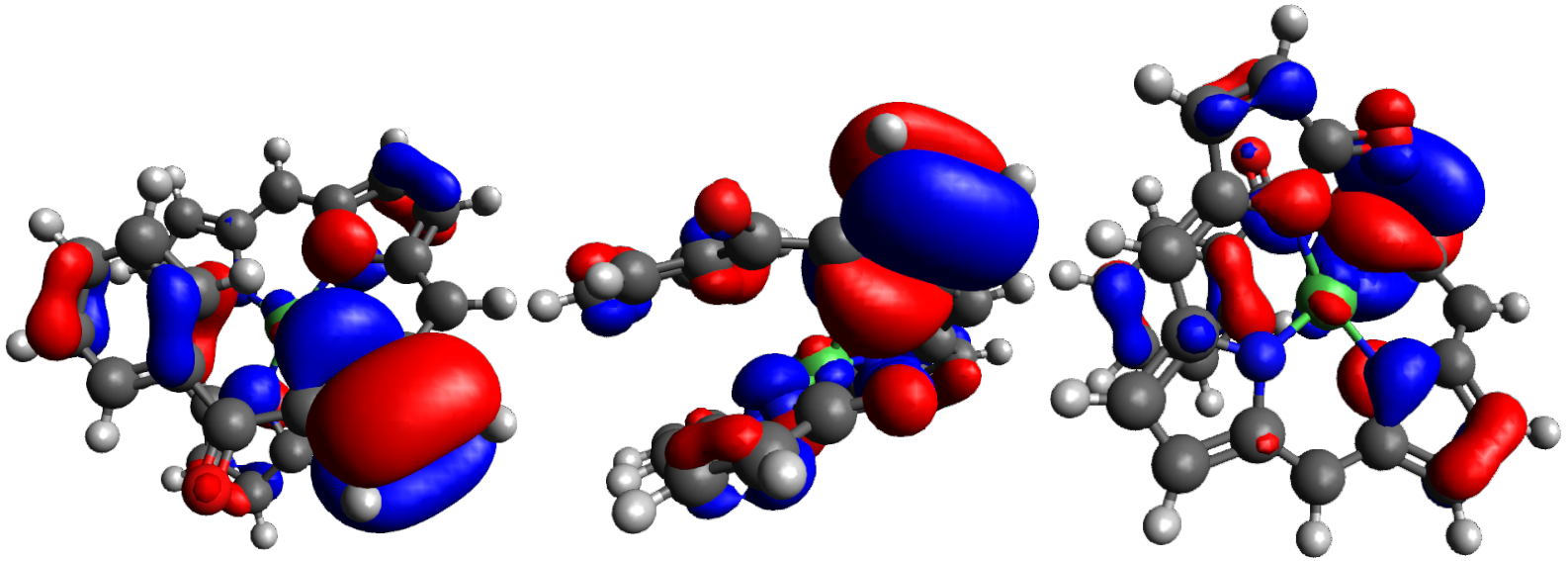

Figure C.46: Frontier orbitals of truncated Ni(TPBT), obtained via calculation with the B2PLYP functional and the def2-TZVP basis set. Augmenta-tions are mentioned on page 29. Shown is HOMO-2 (MO 114) at -0.28936 Eh (-7.8738 eV)

HOMO-3

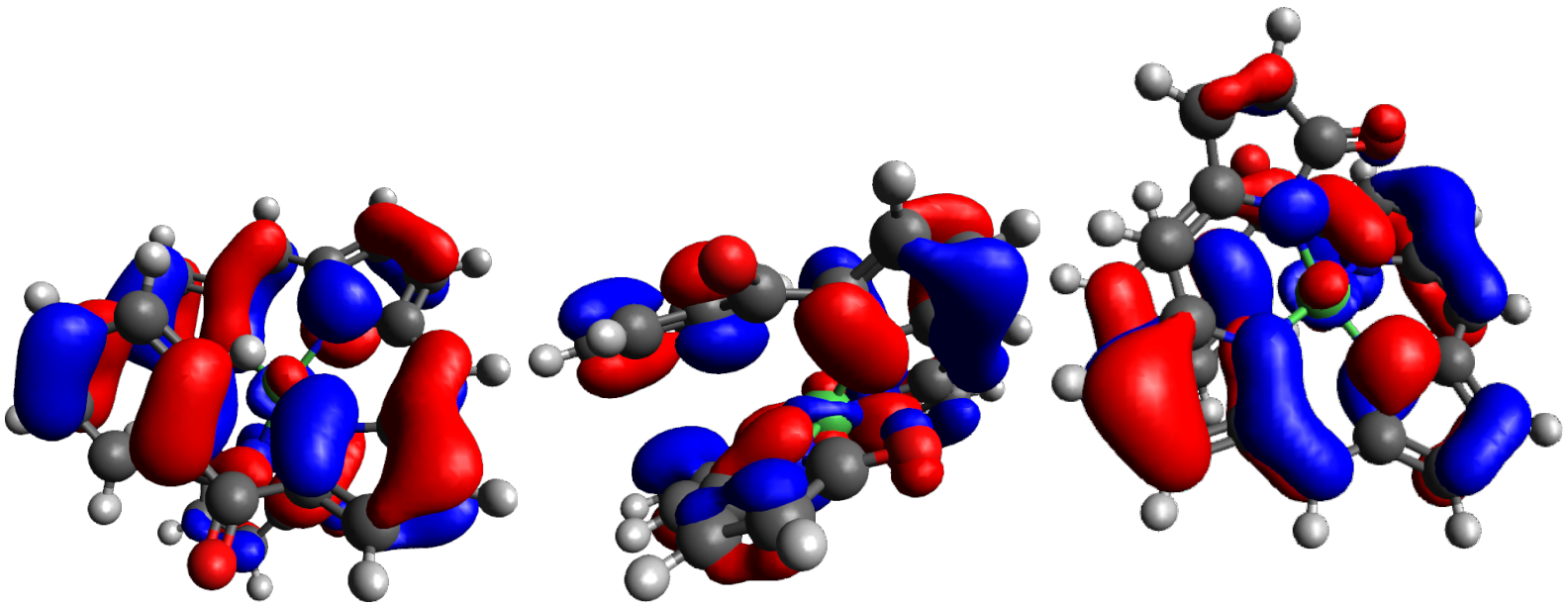

Figure C.47: Frontier orbitals of truncated Ni(TPBT), obtained via calculation with the B2PLYP functional and the def2-TZVP basis set. Augmenta-tions are mentioned on page 29. Shown is HOMO-3 (MO 113) at -0.29495 Eh (-8.0259 eV)

HOMO-4

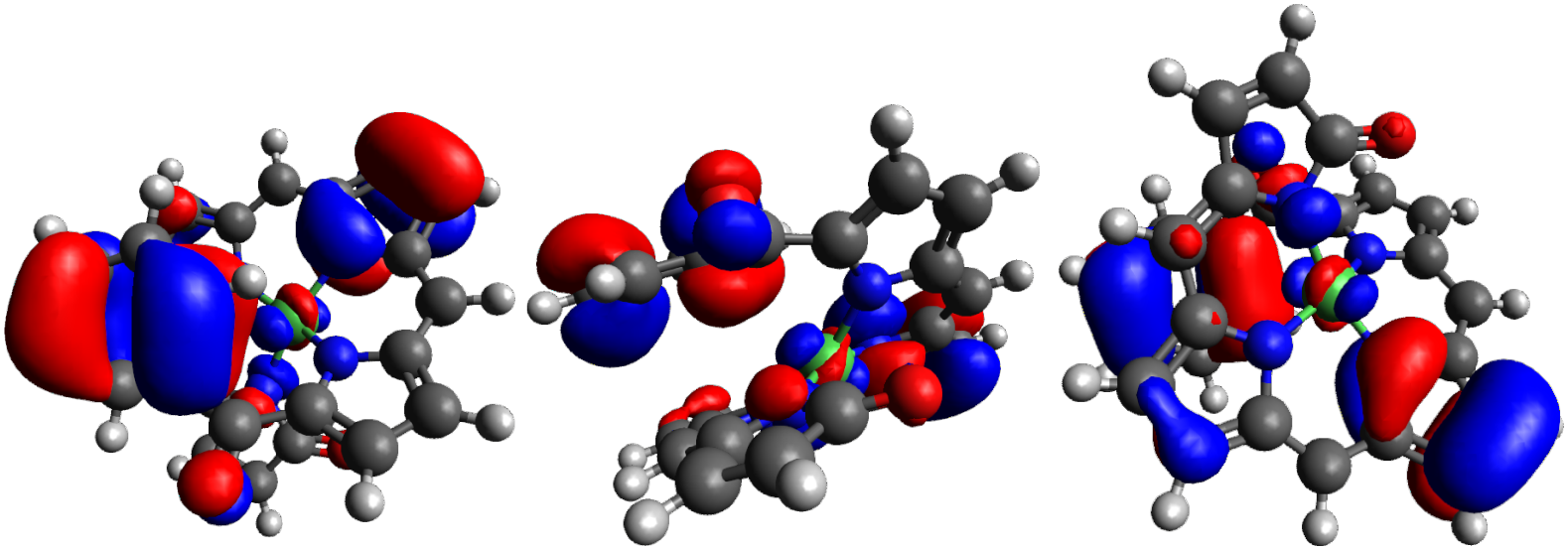

Figure C.48: Frontier orbitals of truncated Ni(TPBT), obtained via calculation with the B2PLYP functional and the def2-TZVP basis set. Augmenta-tions are mentioned on page 29. Shown is HOMO-4 (MO 112) at -0.29910 Eh (-8.1390 eV)

C.10 Predicted Excited States of Truncated Ni(TPBT)

First ten states. Only contributions larger than 0.01 (1 %) are listed.

```
STATE 1: E= 0.067225 au 1.829 eV 14754.2 cm**-1 <S**2> = 0.000000
104a -> 126a : 0.049233 (c= -0.22188622)
115a -> 118a : 0.026020 (c= -0.16130778)
116a -> 117a : 0.843866 (c= -0.91862164)

STATE 2: E= 0.094531 au 2.572 eV 20747.1 cm**-1 <S**2> = 0.000000
88a -> 126a : 0.027731 (c= -0.16652479)
97a -> 126a : 0.015014 (c= -0.12253083)
104a -> 125a : 0.043795 (c= 0.20927252)
104a -> 126a : 0.434917 (c= -0.65948228)
104a -> 127a : 0.063471 (c= 0.25193550)
104a -> 128a : 0.013866 (c= -0.11775264)
104a -> 141a : 0.011546 (c= -0.10745144)
105a -> 126a : 0.037417 (c= 0.19343378)
110a -> 126a : 0.033360 (c= 0.18264820)
112a -> 126a : 0.017596 (c= 0.13264898)
113a -> 126a : 0.011428 (c= -0.10690214)
116a -> 117a : 0.088804 (c= 0.29799982)

STATE 3: E= 0.094907 au 2.583 eV 20829.6 cm**-1 <S**2> = 0.000000
74a -> 126a : 0.010598 (c= -0.10294578)
83a -> 126a : 0.021074 (c= 0.14516831)
94a -> 126a : 0.036479 (c= 0.19099431)
97a -> 125a : 0.010573 (c= -0.10282669)
97a -> 126a : 0.100896 (c= 0.31764052)
97a -> 127a : 0.014818 (c= -0.12172859)
98a -> 126a : 0.094699 (c= -0.30773238)
98a -> 127a : 0.013732 (c= 0.11718259)
99a -> 126a : 0.032051 (c= -0.17902767)
100a -> 126a : 0.019393 (c= -0.13925880)
```

```
103a -> 125a : 0.010262 (c= -0.10130336)
103a -> 126a : 0.103756 (c= 0.32211104)
103a -> 127a : 0.015066 (c= -0.12274239)
108a -> 126a : 0.018496 (c= -0.13600012)
112a -> 126a : 0.035560 (c= 0.18857397)
113a -> 126a : 0.093886 (c= 0.30640851)
113a -> 127a : 0.013110 (c= -0.11449899)
115a -> 126a : 0.027149 (c= -0.16476981)

STATE 4: E= 0.100570 au 2.737 eV 22072.5 cm**-1 <S**2> = 0.000000
89a -> 126a : 0.015558 (c= 0.12473035)
95a -> 126a : 0.099008 (c= 0.31465578)
95a -> 127a : 0.014586 (c= -0.12077146)
97a -> 126a : 0.085235 (c= -0.29195002)
97a -> 127a : 0.012046 (c= 0.10975485)
98a -> 126a : 0.061838 (c= -0.24867221)
101a -> 126a : 0.013427 (c= -0.11587534)
102a -> 125a : 0.021160 (c= -0.14546342)
102a -> 126a : 0.213846 (c= 0.46243527)
102a -> 127a : 0.031500 (c= -0.17748317)
110a -> 126a : 0.043119 (c= 0.20765051)
112a -> 126a : 0.045398 (c= -0.21306842)
114a -> 126a : 0.036812 (c= 0.19186435)

STATE 5: E= 0.115588 au 3.145 eV 25368.6 cm**-1 <S**2> = 0.000000
80a -> 126a : 0.023803 (c= 0.15428132)
83a -> 126a : 0.056129 (c= -0.23691535)
85a -> 125a : 0.015064 (c= -0.12273625)
85a -> 126a : 0.154520 (c= 0.39309003)
85a -> 127a : 0.023119 (c= -0.15204937)
89a -> 126a : 0.028965 (c= 0.17019177)
91a -> 126a : 0.013217 (c= -0.11496545)
93a -> 125a : 0.012965 (c= 0.11386368)
93a -> 126a : 0.131660 (c= -0.36284932)
93a -> 127a : 0.019487 (c= 0.13959631)
```

```
94a -> 126a : 0.082355 (c= -0.28697599)
94a -> 127a : 0.012185 (c= 0.11038422)
97a -> 126a : 0.015088 (c= 0.12283211)
99a -> 126a : 0.035404 (c= -0.18815864)
103a -> 126a : 0.045690 (c= 0.21375232)

STATE 6: E= 0.081053 au 2.206 eV 17789.0 cm**-1 <S**2> = 0.000000
113a -> 117a : 0.014712 (c= 0.12129270)
115a -> 117a : 0.677904 (c= -0.82334905)
116a -> 118a : 0.269555 (c= 0.51918673)

STATE 7: E= 0.097543 au 2.654 eV 21408.3 cm**-1 <S**2> = 0.000000
112a -> 117a : 0.023180 (c= 0.15225031)
113a -> 117a : 0.071376 (c= -0.26716328)
114a -> 117a : 0.156379 (c= -0.39544781)
114a -> 118a : 0.014902 (c= 0.12207404)
115a -> 117a : 0.139622 (c= 0.37366046)
116a -> 118a : 0.519082 (c= 0.72047324)

STATE 8: E= 0.098603 au 2.683 eV 21640.9 cm**-1 <S**2> = 0.000000
113a -> 117a : 0.010918 (c= -0.10448911)
114a -> 117a : 0.700456 (c= -0.83693261)
115a -> 117a : 0.062143 (c= -0.24928442)
116a -> 118a : 0.121423 (c= -0.34845871)

STATE 9: E= 0.104029 au 2.831 eV 22831.8 cm**-1 <S**2> = 0.000000
108a -> 117a : 0.013012 (c= -0.11406900)
110a -> 117a : 0.258597 (c= 0.50852437)
111a -> 117a : 0.022409 (c= -0.14969744)
112a -> 117a : 0.053759 (c= 0.23185895)
113a -> 117a : 0.517669 (c= 0.71949223)
114a -> 117a : 0.035542 (c= -0.18852520)
115a -> 117a : 0.027892 (c= 0.16700962)

STATE 10: E= 0.100586 au 2.737 eV 22076.0 cm**-1 <S**2> = 0.000000
```

```
110a -> 117a : 0.419281 (c= 0.64751905)
110a -> 118a : 0.018843 (c= 0.13726817)
111a -> 117a : 0.083741 (c= -0.28937982)
112a -> 117a : 0.225426 (c= -0.47479006)
113a -> 117a : 0.143375 (c= -0.37864828)
115a -> 118a : 0.010345 (c= 0.10171004)
```

C.11 Predicted ECD Transitions of Truncated Ni(TPBT)

CD SPECTRUM

State	Energy (cm-1)	Wavelength (nm)	R (1e40*cgs)	MX (au)	MY (au)	MZ (au)
1	14754.2	677.8	-639.32118	1.13853	-0.55852	0.46786
2	20747.1	482.0	-99.13309	-0.37254	0.12360	-0.16229
3	20829.6	480.1	40.57273	0.00490	0.60463	0.01083
4	22072.5	453.1	8.92707	-0.13565	-0.03240	0.49111
5	25368.6	394.2	-0.25711	0.73770	-0.60851	0.21740
6	17789.0	562.1	10.52646	-0.09899	-0.00469	-0.03497
7	21408.3	467.1	462.23591	0.27703	0.16705	0.39479
8	21640.9	462.1	71.42189	-0.09098	-0.20455	-0.13910
9	22831.8	438.0	103.34547	-0.19883	0.16665	0.13059
10	22076.0	453.0	12.03560	0.11351	-0.13353	-0.03270
11	24828.5	402.8	213.66735	-0.23802	0.28767	0.12764
12	26051.7	383.9	14.28760	0.00885	-0.07622	-0.16897
13	25495.9	392.2	7.74395	0.00197	0.13124	0.01863
14	26865.9	372.2	-105.43770	-0.11024	-0.09194	-0.18081
15	26669.8	375.0	80.89435	-0.00273	0.08892	-0.14935
16	27824.0	359.4	-67.22386	-0.05574	0.09655	-0.11483
17	29409.2	340.0	213.30961	-0.49337	0.30624	0.20258
18	29458.4	339.5	-28.36814	0.00927	0.08954	0.04602
19	29279.9	341.5	-64.97221	0.31629	-0.14745	0.12401
20	31085.1	321.7	-192.64728	-0.04175	-0.19732	-0.20870
21	30065.3	332.6	36.17927	-0.01797	-0.05125	0.19591
22	32521.5	307.5	-43.10503	-0.21161	0.05242	0.02644
23	35611.7	280.8	-36.12744	0.22208	-0.08789	-0.03043
24	32475.3	307.9	16.48369	0.20941	0.01871	0.05482
25	28706.8	348.3	-16.92511	-0.10071	0.17343	0.18347
26	28401.5	352.1	-59.33448	0.15746	-0.01252	-0.06178

CD SPECTRUM

State	Energy (cm-1)	Wavelength (nm)	R (1e40*cgs)	MX (au)	MY (au)	MZ (au)
27	30281.1	330.2	-27.54400	-0.08443	0.05009	0.17523
28	20214.1	494.7	-1.90657	-0.01857	0.12072	0.13678
29	33535.1	298.2	5.07107	0.05963	-0.05698	-0.04300
30	41164.3	242.9	0.10632	-0.07872	0.02286	-0.07427
31	31591.4	316.5	6.15963	0.04847	-0.04608	0.04357
32	41732.3	239.6	-1.32136	-0.03275	0.04094	0.03210
33	31656.9	315.9	-27.28718	0.01035	0.02365	0.15654
34	37343.3	267.8	-25.97378	0.05822	0.03406	-0.12122
35	42574.3	234.9	0.04292	0.02562	-0.02616	-0.01286
36	35896.2	278.6	1.40435	-0.05900	-0.01217	0.02358
37	33900.1	295.0	-15.95063	0.36710	0.06346	0.29426
38	35518.6	281.5	-35.54184	0.15505	0.16966	0.11117
39	32570.6	307.0	-1.60497	0.11890	0.02652	0.39592
40	37427.3	267.2	35.79695	0.01782	-0.34800	-0.12260
41	37768.7	264.8	-9.80129	0.12851	-0.07054	0.04314
42	37243.6	268.5	22.72058	0.18944	0.17362	0.11433
43	39448.6	253.5	-8.15441	-0.36157	0.11836	0.11332
44	35206.5	284.0	-1.62241	0.00669	-0.00886	-0.01194
45	37119.9	269.4	24.18237	0.19004	-0.09590	-0.04480
46	42156.5	237.2	-8.66261	-0.15824	0.06403	-0.03443
47	39364.1	254.0	25.51469	0.21413	-0.21370	0.13795
48	40376.2	247.7	-27.19811	0.19535	0.07306	-0.14579
49	38159.3	262.1	-0.90004	-0.06947	-0.04297	-0.19012
50	37558.1	266.3	4.21534	-0.09368	-0.03190	-0.13562
51	46673.4	214.3	-16.61243	-0.12549	-0.13065	0.21423
52	36715.7	272.4	-26.92990	-0.17528	0.09982	-0.17335
53	44996.9	222.2	-41.22987	0.08709	0.07719	0.41587
54	44776.3	223.3	-9.86999	-0.09583	-0.04225	-0.08682
55	30750.6	325.2	13.58407	-0.02146	0.11874	0.15106

CD SPECTRUM

State	Energy (cm-1)	Wavelength (nm)	R (1e40*cgs)	MX (au)	MY (au)	MZ (au)
56	34509.3	289.8	6.78273	0.01662	-0.00662	0.10350
57	40155.2	249.0	2.97136	-0.19552	-0.23936	0.04240
58	47343.2	211.2	0.65690	0.07939	-0.06139	0.02473
59	39884.6	250.7	5.89291	0.04786	-0.02887	-0.00635
60	46202.8	216.4	3.49735	-0.19759	0.06160	0.03581
61	44157.8	226.5	-4.90765	0.24814	0.01575	-0.03597
62	39905.6	250.6	-23.14513	0.22571	0.17273	-0.06745
63	40762.8	245.3	25.02118	-0.01299	0.43725	-0.15003
64	42399.0	235.9	20.48737	-0.00987	-0.28401	-0.05493
65	41190.2	242.8	-4.36349	-0.13126	-0.06079	0.15205
66	45236.0	221.1	-69.06258	-0.21780	0.10092	0.43799
67	42951.6	232.8	-29.76400	-0.22045	0.16834	0.04393
68	42053.9	237.8	-40.16583	0.11742	-0.12919	0.00708
69	45018.0	222.1	-13.12158	0.02976	0.15773	-0.02769
70	41145.9	243.0	15.27271	0.00196	-0.12982	-0.27131
71	46211.0	216.4	10.66688	0.04786	0.03054	-0.09366
72	42977.0	232.7	26.61519	0.48376	0.00437	-0.07079
73	42227.2	236.8	20.26791	-0.20412	-0.26534	0.00210
74	46634.7	214.4	-6.06235	0.10034	0.14405	0.17416
75	46368.4	215.7	-3.55298	0.08458	-0.02088	-0.00915
76	50757.8	197.0	118.66001	0.03061	0.25320	0.34060
77	48820.4	204.8	42.08066	-0.03201	-0.11181	-0.19171
78	43072.2	232.2	-64.91432	0.25758	0.26244	0.10507
79	46944.9	213.0	27.58761	0.48578	0.16939	0.28508
80	49260.1	203.0	-4.75312	-0.24870	-0.21767	0.24200
81	41590.0	240.4	-18.31394	-0.09335	-0.11866	-0.25644
82	47773.0	209.3	-4.03675	-0.12840	-0.04200	0.09803
83	48733.6	205.2	-17.59019	-0.07486	-0.13355	-0.11319
84	50113.7	199.5	5.01792	0.00030	-0.03957	-0.17260

CD SPECTRUM

State	Energy (cm-1)	Wavelength (nm)	R (1e40*cgs)	MX (au)	MY (au)	MZ (au)
85	51481.1	194.2	18.24003	-0.01377	-0.11964	0.01218
86	47203.9	211.8	28.22684	-0.12948	0.02223	0.13312
87	48734.8	205.2	13.81550	-0.11608	0.00477	0.08916
88	51594.3	193.8	36.52614	0.10240	0.00035	-0.16022
89	45590.0	219.3	29.89586	0.18561	0.08623	-0.11498
90	54261.2	184.3	-10.40473	0.08135	-0.05152	-0.09490
91	50311.3	198.8	4.95116	0.04770	-0.17182	0.02136
92	53750.7	186.0	26.79791	0.04800	-0.24153	0.14653
93	50826.3	196.7	-9.42247	0.02808	-0.14170	-0.08016
94	51034.7	195.9	-3.97665	0.11895	0.11303	0.11136
95	48700.4	205.3	-27.12058	0.10661	0.02419	0.19779
96	48884.0	204.6	14.11441	0.06158	-0.00618	-0.04671
97	51951.7	192.5	3.76526	-0.12083	0.27564	-0.05536
98	44163.8	226.4	-28.33090	0.18514	0.15720	0.04946
99	46739.4	214.0	35.51344	-0.05791	-0.20677	0.08030
100	51846.2	192.9	-30.74396	0.11081	-0.11659	-0.09450

C.12 Predicted Excited States of Truncated Ni(OEFB)

First ten states. Only contributions larger than 0.01 (1 %) are listed.

```
STATE  1:  E=   0.072488 au      1.973 eV    15909.3 cm**-1
74a -> 101a  :     0.013371 (c=  0.11563322)
75a -> 101a  :     0.014656 (c=  0.12106081)
81a -> 101a  :     0.026335 (c= -0.16228023)
81a -> 105a  :     0.013442 (c= -0.11593802)
85a ->  99a  :     0.039267 (c=  0.19815945)
85a -> 101a  :     0.413896 (c=  0.64334772)
85a -> 102a  :     0.026495 (c= -0.16277298)
85a -> 105a  :     0.209179 (c=  0.45736140)
85a -> 113a  :     0.027186 (c= -0.16488299)
92a -> 101a  :     0.016357 (c=  0.12789489)

STATE  2:  E=   0.070381 au      1.915 eV    15446.9 cm**-1
70a -> 101a  :     0.029276 (c=  0.17110283)
70a -> 105a  :     0.015195 (c=  0.12326934)
81a ->  99a  :     0.018959 (c= -0.13769153)
81a -> 101a  :     0.206489 (c= -0.45441103)
81a -> 102a  :     0.013158 (c=  0.11470865)
81a -> 105a  :     0.105781 (c= -0.32524044)
81a -> 113a  :     0.014783 (c=  0.12158441)
84a -> 101a  :     0.010856 (c=  0.10419270)
85a -> 101a  :     0.027129 (c= -0.16470975)
85a -> 105a  :     0.013636 (c= -0.11677436)
86a ->  99a  :     0.011707 (c=  0.10819791)
86a -> 101a  :     0.124526 (c=  0.35288245)
86a -> 105a  :     0.063291 (c=  0.25157693)
93a -> 101a  :     0.060905 (c= -0.24679003)
93a -> 105a  :     0.029596 (c= -0.17203608)
95a -> 101a  :     0.012983 (c=  0.11394246)
```

```
STATE  3:  E=   0.074896 au      2.038 eV    16437.7 cm**-1
76a -> 101a  :     0.011606 (c=  0.10773325)
77a -> 101a  :     0.010595 (c=  0.10293202)
79a -> 101a  :     0.082216 (c=  0.28673379)
79a -> 105a  :     0.042097 (c=  0.20517533)
80a ->  99a  :     0.014151 (c=  0.11895927)
80a -> 101a  :     0.152651 (c=  0.39070557)
80a -> 105a  :     0.078076 (c=  0.27942025)
80a -> 113a  :     0.010620 (c= -0.10305503)
84a ->  99a  :     0.013573 (c=  0.11650178)
84a -> 101a  :     0.142228 (c=  0.37713192)
84a -> 105a  :     0.072275 (c=  0.26883984)
86a -> 101a  :     0.016981 (c= -0.13031254)
92a -> 101a  :     0.031039 (c=  0.17617786)
92a -> 105a  :     0.014974 (c=  0.12236640)
93a -> 101a  :     0.010305 (c= -0.10151551)
94a -> 101a  :     0.018655 (c=  0.13658394)

STATE  4:  E=   0.093721 au      2.550 eV    20569.5 cm**-1
62a -> 101a  :     0.017068 (c= -0.13064312)
64a -> 101a  :     0.014601 (c= -0.12083566)
66a -> 101a  :     0.050669 (c= -0.22509666)
66a -> 105a  :     0.026355 (c= -0.16234366)
67a -> 101a  :     0.048879 (c= -0.22108672)
67a -> 105a  :     0.025406 (c= -0.15939373)
68a ->  99a  :     0.011599 (c= -0.10769650)
68a -> 101a  :     0.127416 (c= -0.35695330)
68a -> 105a  :     0.066149 (c= -0.25719462)
69a -> 101a  :     0.060742 (c=  0.24645989)
69a -> 105a  :     0.031534 (c=  0.17757705)
74a -> 101a  :     0.011614 (c=  0.10776876)
78a -> 101a  :     0.104244 (c=  0.32286862)
78a -> 105a  :     0.053480 (c=  0.23125684)
81a -> 101a  :     0.024387 (c=  0.15616195)
81a -> 105a  :     0.012456 (c=  0.11160815)
```

```
STATE  5:  E=   0.067549 au      1.838 eV    14825.3 cm**-1
95a ->  98a  :     0.030461 (c= -0.17452962)
96a ->  97a  :     0.929982 (c=  0.96435561)

STATE  6:  E=   0.086171 au      2.345 eV    18912.3 cm**-1
93a ->  97a  :     0.011492 (c= -0.10720017)
95a ->  97a  :     0.581743 (c=  0.76272090)
96a ->  98a  :     0.374577 (c=  0.61202665)

STATE  7:  E=   0.098269 au      2.674 eV    21567.6 cm**-1
91a ->  97a  :     0.023340 (c= -0.15277498)
94a ->  97a  :     0.665011 (c= -0.81548226)
94a ->  98a  :     0.033102 (c=  0.18193958)
95a ->  97a  :     0.066804 (c=  0.25846404)
96a ->  98a  :     0.146643 (c= -0.38294042)

STATE  8:  E=   0.107341 au      2.921 eV    23558.7 cm**-1
90a ->  97a  :     0.017312 (c=  0.13157661)
91a ->  97a  :     0.035645 (c=  0.18879835)
92a ->  97a  :     0.307241 (c=  0.55429310)
93a ->  97a  :     0.388987 (c=  0.62368856)
94a ->  97a  :     0.093082 (c= -0.30509373)
96a ->  98a  :     0.082604 (c=  0.28740903)

STATE  9:  E=   0.113252 au      3.082 eV    24855.8 cm**-1
88a ->  98a  :     0.014731 (c= -0.12137235)
90a ->  97a  :     0.021336 (c= -0.14607006)
91a ->  97a  :     0.072988 (c= -0.27016382)
92a ->  97a  :     0.186104 (c=  0.43139813)
92a ->  98a  :     0.025356 (c=  0.15923411)
93a ->  97a  :     0.035311 (c=  0.18791292)
94a ->  97a  :     0.138298 (c=  0.37188462)
95a ->  97a  :     0.151109 (c=  0.38872781)
95a ->  99a  :     0.010270 (c=  0.10134124)
```

```
96a ->  98a  :     0.241732 (c= -0.49166226)

STATE 10:  E=   0.105295 au      2.865 eV    23109.6 cm**-1
89a ->  97a  :     0.045901 (c=  0.21424570)
89a ->  98a  :     0.024054 (c=  0.15509437)
89a ->  99a  :     0.013288 (c=  0.11527209)
91a ->  97a  :     0.016246 (c=  0.12745877)
92a ->  97a  :     0.353334 (c=  0.59441862)
92a ->  98a  :     0.017036 (c=  0.13052099)
93a ->  97a  :     0.438847 (c= -0.66245499)
95a ->  97a  :     0.016429 (c= -0.12817447)
```

C.13 Predicted ECD Transitions of Truncated Ni(OEFB)

CD SPECTRUM

State	Energy	Wavelength	R	MX	MY	MZ
	(cm-1)	(nm)	(1e40*cgs)	(au)	(au)	(au)	
1	15909.3	628.6	-4.79023	-0.04209	-0.13761	-0.12423
2	15446.9	647.4	14.62939	-0.34283	-0.40949	-0.14676
3	16437.7	608.4	0.82143	-0.39261	0.34594	-0.18140
4	20569.5	486.2	3.95713	0.29622	-0.12918	-1.04351
5	14825.3	674.5	537.01947	0.45076	-0.08125	-1.41805
6	18912.3	528.8	3.45362	0.01474	0.02852	0.04320
7	21567.6	463.7	-68.06450	0.01208	0.09693	-0.14060
8	23558.7	424.5	-6.56612	-0.08030	-0.03110	0.20059
9	24855.8	402.3	-196.99047	-0.01792	0.18823	-0.04632
10	23109.6	432.7	-37.45267	0.10416	-0.09197	-0.10678
11	25308.1	395.1	121.37868	0.12124	-0.27168	0.03082
12	23891.5	418.6	-2.84908	0.13296	0.10579	0.08547
13	22722.1	440.1	-2.86734	0.03867	0.01726	-0.13904
14	25437.6	393.1	-183.47460	0.38839	-0.14827	-0.51167
15	24164.8	413.8	-140.28530	-0.20795	0.14165	0.23662
16	26845.0	372.5	-20.23584	-0.07235	0.07217	0.06110
17	29110.4	343.5	28.93270	-0.12535	-0.01806	0.31549
18	32027.0	312.2	59.74014	0.02955	-0.13142	-0.05017
19	39028.2	256.2	14.08847	-0.00898	0.01177	-0.07498
20	34145.4	292.9	141.29967	0.02365	0.03412	0.25382
21	32863.1	304.3	6.79713	0.08823	0.00665	-0.15229
22	32332.8	309.3	4.48235	-0.08100	0.05072	0.11132
23	23125.0	432.4	20.09476	-0.03304	0.11517	0.16592
24	30939.6	323.2	4.85851	0.02835	-0.17895	-0.00912
25	34769.3	287.6	-0.22323	-0.00990	0.01401	0.00135
26	35535.0	281.4	-6.93867	-0.01908	0.14011	-0.08120

CD SPECTRUM

State (cm-1)	Energy (nm)	Wavelength (1e40*cgs)	R (au)	MX (au)	MY (au)	MZ
27	40849.9	244.8	3.20385	-0.09369	0.03654	0.03975
28	29206.3	342.4	-23.31681	-0.10520	-0.08263	0.06066
29	42765.1	233.8	-0.00235	-0.01089	0.01340	0.00587
30	30957.4	323.0	-2.07204	-0.04931	-0.05997	0.04738
31	28992.9	344.9	24.78063	0.08374	0.01932	-0.01471
32	32562.9	307.1	-30.74595	-0.12392	-0.01070	-0.19034
33	29276.9	341.6	19.09683	-0.11289	-0.06536	0.12087
34	37779.5	264.7	-13.92480	0.15496	-0.03695	-0.11549
35	40326.5	248.0	46.67732	-0.17271	0.10595	0.36185
36	38527.3	259.6	2.09672	-0.08213	-0.06038	-0.37173
37	34908.4	286.5	17.32300	-0.14623	-0.03159	0.09177
38	46283.4	216.1	-18.67918	0.01878	-0.17935	0.06141
39	38417.6	260.3	-7.63715	-0.01275	-0.04134	0.05228
40	34820.5	287.2	-10.02432	0.14981	-0.15413	0.16847
41	34751.7	287.8	10.03587	-0.13557	-0.03728	0.24540
42	33177.2	301.4	-19.36951	0.05814	-0.20636	-0.08724
43	44544.3	224.5	-1.43446	0.11358	-0.04091	-0.15384
44	41803.2	239.2	-2.93935	-0.08784	-0.12647	0.23165
45	48824.9	204.8	24.12721	0.26098	-0.01568	0.08794
46	40217.4	248.6	-44.53463	0.12878	-0.11470	0.03671
47	43037.0	232.4	6.95024	-0.08045	0.00588	0.25441
48	37960.1	263.4	-8.99388	0.02350	-0.03353	-0.00944
49	39389.9	253.9	46.17386	0.08407	-0.09700	-0.40526
50	50289.5	198.8	-4.11709	0.06119	0.02925	-0.03679
51	45312.9	220.7	57.35310	0.04700	-0.08273	-0.38325
52	48969.5	204.2	-3.04353	0.31612	0.03074	0.19611
53	44141.5	226.5	-19.05659	0.16417	0.12379	-0.10201
54	35223.4	283.9	11.45722	-0.08648	-0.00292	-0.01215
55	36812.2	271.6	-8.08447	0.02379	0.12858	-0.02895

CD SPECTRUM

State (cm-1)	Energy (nm)	Wavelength (1e40*cgs)	R (au)	MX (au)	MY (au)	MZ
56	50780.3	196.9	-38.68385	-0.20944	0.35020	0.05799
57	47247.0	211.7	-18.40075	-0.00504	-0.26884	0.01800
58	38478.1	259.9	-5.85641	0.05424	-0.00148	0.06291
59	36910.4	270.9	16.14359	-0.00715	-0.20973	0.04831
60	38433.6	260.2	-2.94539	-0.00945	0.00082	-0.07393
61	41053.6	243.6	4.37504	-0.00281	-0.02090	0.07704
62	38233.8	261.5	-14.57308	-0.00273	-0.07680	-0.09983
63	51133.9	195.6	25.19969	-0.22656	-0.30668	-0.08209
64	41748.3	239.5	1.43434	0.18372	-0.10486	-0.08978
65	52504.2	190.5	-6.62661	-0.01237	0.10813	-0.11892
66	44083.5	226.8	-2.03139	0.04227	-0.03825	0.05823
67	46909.0	213.2	17.63127	0.03861	0.11221	-0.03434
68	47980.3	208.4	-26.72824	0.02539	0.11869	-0.03312
69	43294.6	231.0	-0.77418	0.06427	-0.04529	-0.04833
70	49108.7	203.6	-9.67707	0.19333	-0.09228	-0.12770
71	51526.4	194.1	-1.76746	-0.06384	0.11605	-0.14667
72	48067.0	208.0	28.13851	-0.06699	0.20730	0.08232
73	54090.7	184.9	-20.47146	-0.00237	-0.05769	-0.13008
74	53821.1	185.8	-14.38904	-0.04980	-0.00579	-0.13940
75	51205.1	195.3	20.27594	-0.00361	-0.17956	0.07556
76	43625.6	229.2	-2.24045	0.04065	-0.03602	0.01604
77	44502.1	224.7	1.21897	-0.10296	0.00492	0.19101
78	44297.5	225.7	3.03259	-0.08082	-0.01710	-0.11907
79	47779.1	209.3	5.18112	0.04091	0.09529	-0.03494
80	33921.5	294.8	0.09645	-0.04794	-0.03096	0.01557
81	48810.7	204.9	-12.68479	-0.02458	0.17605	0.27290
82	49408.8	202.4	-0.33659	-0.03014	0.01525	0.09607
83	49280.8	202.9	28.01542	0.08609	0.11561	-0.09118
84	53054.6	188.5	-17.96038	0.00354	-0.17591	-0.12335

CD SPECTRUM

State	Energy (cm-1)	Wavelength (nm)	R (1e40*cgs)	MX (au)	MY (au)	MZ (au)
85	51262.1	195.1	-39.95255	0.13030	-0.26106	0.01558
86	53446.9	187.1	-12.98436	0.01890	-0.14129	0.05303
87	51624.3	193.7	-12.24627	0.11114	-0.08237	0.03579
88	51258.6	195.1	0.04739	-0.13392	0.08224	0.03600
89	53410.6	187.2	28.29559	-0.14155	0.14087	0.04016
90	54623.1	183.1	13.86898	-0.09435	-0.02664	-0.32193
91	41336.3	241.9	-5.91490	-0.07038	0.04720	-0.13117
92	53542.2	186.8	28.75925	-0.01450	-0.24587	-0.10975
93	51235.5	195.2	8.66226	0.16969	-0.09017	0.20928
94	52715.5	189.7	-7.00091	0.09226	0.01733	-0.04931
95	55905.9	178.9	-4.79616	-0.09721	0.01477	-0.02530
96	53345.0	187.5	3.86134	-0.01374	-0.07059	-0.03679
97	51540.0	194.0	-3.59722	0.09722	0.15669	0.11296
98	53056.9	188.5	13.76157	-0.15562	0.02032	-0.06891
99	51758.8	193.2	0.60370	-0.13627	0.00265	0.14167
100	54506.3	183.5	6.47612	-0.10006	0.19796	0.02159

C.14 Shell Scripts for mc-AFM Evaluation

Note: Sections beginning with a right arrow (===>) are part of the previous line in the script. In the below code, lines have been broken up for ease of reading. These scripts may be run on other operating systems using tools such as `git bash`*,* `cygwin`*, or* `mingw32`*.*

C.14.1 Statistics on $I(V)$ Curves

```
#!/bin/sh

# This script creates averaged I(V) curves and returns some helpful
===> statistics
# like the confidence interval, mean error, variance etc.
# To run this, make sure your input files have the following
===> structure
#  HEADER HEADER
# BIAS   VOLTAGE
# You can do this in Bruker NanoScope Analysis by selecting all files
===> you want to
# export, then right-clicking "Export" > "ASCII ..."
# Check the following boxes only: "TUNA Current", "Display", "Ramp",
===> and
# either "Extend" or "Retract". The script will run on all *.txt
===> files in the
# current directory. Make sure no other text files reside there!

echo "mc-AFM spin polarization script"
echo "Adrian Urban/Yamamoto Group/IMS Okazaki"
echo "Provided under GNU GPL license"

# Read user input for downstream spin-polarization analysis
echo ""
echo "Choose the quadrant on the stage. You may choose:"
echo "Quadrant on the stage  BL => back  left quadrant"
echo "                       FL => front  \"     \"   "
```

```
echo "                        BR => back  right  \"   "
echo "                        FL => front  \"     \"     "
printf "Your choice? "
read quadrant
if [[ $quadrant != @(BL|BR|FL|FR) ]]
then
echo "Not a valid choice. Exiting."
exit 1
fi
printf "Angle of the magnet (090 or 270): "
read angle
if [[ $angle != @(090|270) ]]
then
echo "Not a valid choice. Exiting."
exit 1
fi

# Convert Bruker's DOS text format to UNIX
printf "\nConverting files from DOS to UNIX format... "
dos2unix *.txt > /dev/null 2>&1
echo "Done."

# Merge all individual I(V) curves into one file, then
===>determine statistical
# parameters and append these as new columns
printf "Merging individual curves and doing statistics... "
paste *.txt | awk '
function abs(v) {v += 0; return v < 0 ? -v : v}
FNR==1{
printf "Sample Bias / V"
for(i=2; i<=NF; i+=2){
printf ",Current / nA"
}
print ",Average Current / nA,log[abs(I)] / log(nA),Mean
===>Deviation / nA,Variance / nA**2,Standard Deviation / nA,
```

```
===>Standard Error / nA,Upper 95 % Confidence Band / nA,Lower
===>95 % Confidence Band / nA"
}
FNR>=2{
sum=0
fields=0
average=0
params=0
printf $1
for(i=2; i<=NF; i+=2){
printf ","$i*10**9
sum+=$i
fields++
}
average = sum/fields*10**9
if($1==0)
printf average > "offset.var"
printf ","average
printf ","log(abs(average))
meandev=0
for(i=2; i<=NF; i+=2){
meandev=meandev+abs($i*10**9-average)
variance=variance+($i*10**9-average)**2
}
meandev/=fields
variance/=fields
printf ","meandev
printf ","variance
stdev=sqrt(variance)
printf ","stdev
sterr=stdev/sqrt(fields)
printf ","sterr
z_upper=1.960
conf_upper=z_upper*sterr
printf ","conf_upper
```

```
z_lower=-1.960
conf_lower=z_lower*sterr
print ","conf_lower
}
' > $quadrant-$angle-merged.csv
echo "Done."
# Remove the offset
printf "Removing offset ($(cat offset.var) V) in the averaged
===>I(V) curves... "
awk -F',' -v offset="$(cat offset.var)" '
function abs(v) {v += 0; return v < 0 ? -v : v}
FNR==1{
print "Sample Bias / V,Average Corrected Current / nA,
===>log[abs(I)] / log(nA),Mean Deviation / nA,Variance / nA**2,
===>Standard Deviation / nA,Standard Error / nA,Upper 95 %
===> Confidence Band / nA,Lower 95 % Confidence Band / nA"
}
FNR>=2{
printf $1","$(NF-7)-offset","log(abs($(NF-7)-offset))
for(i=NF-5; i<=NF; i++){
printf ","$i
}
print ""
}
' $quadrant-$angle-merged.csv > $quadrant-$angle-corrected.csv
rm offset.var $quadrant-$angle-merged.csv
awk -F',' '{print $1","$2}' $quadrant-$angle-corrected.csv >
===> $quadrant-$angle.csv
echo "Done."
```

C.14.2 Determining the Spin Polarization

```
#!/bin/sh

# This script generates spin-polarization curves from
===> provided I(V) curves
# Here, the definition of SP is defined according to
#  Clever et al. Isr. J. Chem. Vol. 62 No. 11-12,
#  e202200045 (2022). DOI: 10.1002/ijch.202200045
# The provided input files need to have the following naming scheme
#  (BL|BR|FR|FL)-(090|270).csv
# where the first half contains the quadrant on the mc-AFM stage (back,
# front, left, right) and the second half contains the orientation of
# the magnet. This naming scheme is already provided by
===> "mc-afm-stats.sh".
# So far, this script does NOT compensate I(V)-offsets from the
# AFM's sensitivity settings. This needs to be done manually!

echo "mc-AFM spin polarization script"
echo "Adrian Urban/Yamamoto Group/IMS Okazaki"
echo "Provided under GNU GPL"

echo "\nFiles selected for evaluation: $1 and $2"
file1=$1
file2=$2

# CONVERT FROM DOS TO UNIX IF IT DID NOT ALREADY HAPPEN
printf "Converting to UNIX format... "
dos2unix $1 $2 > /dev/null 2>&1
echo "Done."

# ALIGNMENT FOR FIRST FILE
printf "\nGetting current/magnetic field alignment for I(V) curves
===> in $1... "
awk '
```

```
FNR==1{
if (FILENAME ~ /(BL-090|FR-090|BR-270|FR-270)/)
fieldDirection="into-sample"
else if (FILENAME ~ /(BL-270|FR-270|BR-090|FL-090)/)
fieldDirection="out-of-sample"
print "Sample Bias / V,Average Current / nA,Alignment"
}
FNR>=2{
printf $1","$2
if( ($1<0 && fieldDirection=="out-of-sample") || ($1>0
===> && fieldDirection=="into-sample") ){
alignment="parallel"
}
else if( ($1<0 && fieldDirection=="into-sample") || ($1>0 &&
===> fieldDirection=="out-of-sample") ){
alignment="antiparallel"
}
else if( ($1=0 && fieldDirection=="into-sample") || ($1=0 &&
===> fieldDirection=="out-of-sample") ){
alignment="n/A"
}
print alignment
}' $1 > ${file1%%.*}-alignment.csv
echo "Done."

# ALIGNMENT FOR SECOND FILE
printf "Getting current/magnetic field alignment for I(V) curves
===> in $2... "
awk '
FNR==1{
if (FILENAME ~ /(BL-090|FR-090|BR-270|FL-270)/)
fieldDirection="into-sample"
else if (FILENAME ~ /(BL-270|FR-270|BR-090|FL-090)/)
fieldDirection="out-of-sample"
print "Sample Bias / V,Average Current / nA,Alignment"
```

```
}
FNR>=2{
printf $1","$2
if( ($1<0 && fieldDirection=="out-of-sample") || ($1>0 &&
===> fieldDirection=="into-sample") ){
alignment="parallel"
}
else if( ($1<0 && fieldDirection=="into-sample") || ($1>0 &&
===> fieldDirection=="out-of-sample") ){
alignment="antiparallel"
}
else if( ($1=0 && fieldDirection=="into-sample") || ($1=0 &&
===> fieldDirection=="out-of-sample") ){
alignment="n/A"
}
print alignment
}' $2 > ${file2%%.*}-alignment.csv
echo "Done."

# MERGE BOTH FILES AND DO THE POLARIZATION
printf "\nCalculating spin polarization... "
paste -d "," ${file1%%.*}-alignment.csv ${file2%%.*}-alignment.csv
===> | awk -F',' '
FNR==1{
print "Sample Bias / V,Spin Polarization / %"
}
FNR>=2{
printf $1","
if($3=="parallel" && $6=="antiparallel")
print ($2-$5)*100/($2+$5)
else if($3=="antiparallel" && $6=="parallel")
print ($5-$2)*100/($2+$5)
else if($3=$6 || $3=="n/A" || $6=="n/A")
print 0
}' > spin-polarization.csv
```

```
echo "Done."
```